Formation of bright solitary matter-waves

MARCHANT, ANNA,LOUISE

Formation of bright solitary matter-waves

Anna Louise Marchant

Abstract

This thesis presents the development of an experimental apparatus to produce Bose-Einstein condensates (BECs) with tunable interparticle interactions. The ability to precisely control the strength of these interactions, and even to switch them from repulsive to attractive, allows one to probe novel regimes of condensate physics, from the collapse of attractively interacting BECs and the formation of solitary matter-waves to the observation of beyond mean-field effects in strongly repulsive condensates.

The construction and characterisation of both a single and crossed beam optical dipole trap is presented. In the single beam case we develop a technique allowing the guided transport of atoms along the beam and up to a room-temperature surface; a technique which can be used to evaporatively cool the trapped atomic cloud. We produce Bose-Einstein condensates of ^{87}Rb in the $F = 1, m_F = -1$ state in this trap, comparing the effect of beam waist on the evaporation trajectory. In the crossed beam trap Bose-Einstein condensation of ^{87}Rb is realised in three distinct trapping configurations, along with a 1D optical lattice formed by changing the polarisation of the beams.

A method of direct cooling of ^{85}Rb atoms in the crossed trap is developed using a magnetic Feshbach resonance to precisely tune both the elastic and inelastic scattering properties of the atoms. The resonance used for this work occurs at 155 G in collisions between atoms in the $F = 2, m_F = -2$ state of ^{85}Rb. Bose-Einstein condensates of up to 4×10^4 ^{85}Rb atoms are formed in this trap and we demonstrate the presence of tunable interatomic interactions, exploring the collapse phenomenon associated with attractive condensates.

By loading the ^{85}Rb condensate into a quasi-1D waveguide we show that stable attractive condensates can be created, taking the form of bright solitary matter-waves. We observe a solitary wave of $\sim$2,000 atoms which propagates, without dispersion, along the waveguide over a distance of $\sim$1.1 mm. The particle-like nature of the solitary wave is demonstrated by classical reflection of the wavepacket from a repulsive Gaussian barrier.

Formation of bright solitary matter-waves

Anna Louise Marchant

A thesis submitted in partial fulfilment
of the requirements for the degree of
Doctor of Philosophy

Department of Physics
Durham University

December 2012

Contents

List of Figures

Declaration

I confirm that no part of the material offered has previously been submitted by myself for a degree in this or any other University. Where material has been generated through joint work, the work of others has been indicated.

Anna Louise Marchant
Durham, December 2012

Acknowledgements

There are a great many people who have contributed to my time as a PhD student, both in and out of the lab, and I thank them all whole heartedly.

First and foremost I would like to thank my supervisor, Simon Cornish. The first time I met Simon, he lied to me. As a poor, naive undergraduate I believed him when he told me we would be measuring gravity and completing the Standard Model. It took many months and a trip to Vienna for the truth to out. I still haven't completely forgiven him.

Setting that aside, Simon has many fantastic qualities which make him such a great scientist; his attention to detail, his ability to see ways around a problem and most importantly, his love and enthusiasm for his work. However, perhaps most astounding is his ability to annex space in the department which is truly second to none. Simon has taught me a great many things about the intricacies of experimental physics and I am forever indebted to him for his patience, understanding and commitment to ensuring his students succeed. Although this thesis marks the end of my time as one of Simon's students, I am certain that our friendship will last a lifetime.

Life in the lab would have been infinitely less entertaining without the fantastic Sylvi Händel. Many a late night (powered by Haribo, the dulcet tones of (terrible) 90s boy bands and a manic desire make the ELS laser do anything useful) often led to much hilarity and even the occasional bit of physics. Her work setting up the laser cooling system in the early days of the project provided an invaluable foundation for the experiment and has undoubtedly saved the rest of us hours of time.

Thanks go to Tim Wiles for his incredible capacity to make even the most bizarre computer related requests a reality. His ability to turn crazy hand waving into fully functioning Matlab code is truly admirable and frankly, nothing short of witchcraft. Most importantly though, I must thank Tim for all his help following the great flood of 2012. (Although I still maintain that the whole incident was part of an elaborate plan on my part to fix the cooling water supply.) My thanks also go to Steve Hopkins. Steve's knowledge of all things electrical and plumbing related, coupled with the vast contents of his

workshop at home, has been truly invaluable over the years.

The rest of 'The Cornish Division' have my gratitude for making my time in the group what it was. The original Team Mixture, Danny McCarron and Dan 'iron man' Jenkin helped solve numerous problems in the lab back when there were only the four of us - the girls vs. the boys! Hung Wen Cho provided not only endless help with servo circuitry, but also gave me someone to visit in the lab next door during the long nights of data taking. Manfred Yu has proved to be a wonderful addition to Team Soliton, maintaining an alarmingly sunny disposition, even in the face of the most monotonous tasks! Kirsteen Butler must be thanked for her pace-making in the swimming pool whilst Michael Köppinger can always be relied upon to provide a solid German perspective on things if you should happen to find him in the corridors...

Many years ago I attempted to leave Durham, however, my attempt was thwarted by Simon Gardiner. My thanks go to him for convincing me that AtMol would be a great place to work, for introducing me to Simon Cornish and for always taking an interest in my progress over the years. I would also like to thank Ifan Hughes for his willingness to discuss physics problems, his enthusiasm for teaching and for countless entertaining chats in the office. I am also grateful to Charles Adams for his valuable insight at the start of the project.

The AtMol group in Durham has been a wonderfully supportive, encouraging and friendly place to work and has made the last four years thoroughly enjoyable. My thanks go to all its member, both past and present, for loans of equipment, explanations of things I had no idea about and general comedic moments over the years. In particular my thanks go to Jon Pritchard for all the moral support at the start of my PhD and to Adam West for his endless patience with me and my dalliances with Matlab.

No experimental project would be possible without the skill and expertise of the mechanical workshop technicians. I would like to thank Phil Armstrong, Steve Lishman and Malcolm Robertshaw in particular for help with drawings, knowing what I wanted far better than I knew myself and for rushing through jobs when we were short of time. Thanks also go to Norman Thompson for all his organising, coordinating and generally just making the department work.

My PhD time in Durham would have been infinitely more stressful had it not been for some fantastic housemates. The wonderful Alice Danielson is perhaps the happiest, most fun loving person I have ever had the pleasure of knowing. My thanks go to her and Aaron for keeping me entertained even after the house disbanded. What can I say about Tom Billam? It has been a privilege to live and work with such a fantastic friend. (And when he finally

gets the Nobel Prize, this stands as proof that I knew him right back at the beginning!)

Away from Durham, I would like to thank my parents for their endless love and support in everything that I do and their constant encouragement throughout my PhD. Most importantly though, I thank them for always making me believe that I could do anything I wanted to. Without them I could never have achieved all that I have up until now. Lastly, I thank Chris for always being there over the last four years, in spite of the distance between us. Without you, this would have been a million times harder.

To Mum and Dad,
for getting me to where I am.

Chapter 1

Introduction

First observed in the shallow water of the Union canal [1], solitons appear in a diverse range of systems from nonlinear optics and ultracold quantum gases to plasma and particle physics [2]. Arising as solutions to nonlinear wave equations, these wavepackets are unique in that they maintain their shape for all time, are very well localized and emerge from collisions with other solitons having retained both their shape and size. The self-trapped and hence non-dispersive nature of solitons makes them excellent candidates for the study of short-range atom-surface potentials [3], for use in interferometry schemes [4] and for enhancing the understanding of quantum systems. The 3D analogue to the soliton, the bright solitary matter-wave, has previously been observed in Bose-Einstein condensates (BECs) of alkali metal atoms [5, 6, 7]. Early work raised many divisive questions about the formation of such wavepackets [8, 9, 10] but without any further experimental data available to verify theoretical claims many open question still remain.

1.1 Solitons and solitary matter-waves

The term 'soliton' is used to describe any solution of a nonlinear equation or system which *(i) represents a wave of permanent form; (ii) is localised, decaying or becoming constant at infinity; and (iii) may interact strongly with other solitons so that after the interaction it retains its form, almost as if the principle of superposition were valid* [11].

Importantly, true solitons only arise as the solution to *1D* nonlinear equations. In reality quantum gas experiments can never reach this regime, instead only ever obtaining quasi-1D confinement. As such we must instead consider the 3D counterpart of the soliton, the solitary wave, although it is often the case that the terms *soliton* and *solitary wave* are used interchangeably to describe the wavepackets created in experiments.

Solitons can take several forms, being described as bright, dark (or grey) or gap. Here we briefly discuss these categories and relate them to the specific case of solitons or solitary waves in Bose-Einstein condensates.

Bright solitons

Bright solitons occur in the presence of an attractive, or focussing, nonlinearity. These are self-contained wavepackets which propagate without dispersion. Studied most extensively in the field of nonlinear optics [12], bright solitons have also been realised in Bose-Einstein condensates of both lithium [5, 6] and rubidium [7].

The collapse instability of attractive Bose-Einstein condensates [13] means bright solitons must be created by precise tuning of the atomic interactions. A repulsive condensate is first created then, typically by means of a magnetic Feshbach resonance [14], the atomic interactions are switched from positive to negative. Stable solitons can then be formed provided the condensate number does not exceed some critical value N_c.

Dark solitons

Dark solitons take the form of a density dip with a phase jump across the density minimum. As this type of soliton effectively creates a 'notch' in the density profile they are not self-contained objects like bright soliton but instead occur on top of a stable or continuous background. Dark solitons arise in systems which exhibit a defocussing nonlinearity and hence have been studied in many contexts, e.g. optical fibres [15], mechanical systems [16], thin magnetic films [17]. For a review of both the theory and experimental investigations of dark solitons see Ref. [18].

Dark solitons have also been realised in Bose-Einstein condensates with repulsive interactions. Here, the soliton is created via phase engineering of the condensate. This can be done in a number of ways: phase-imprinting [19, 20], density-engineering [21, 22], quantum-state engineering [23, 24] (which is a combination of phase imprinting and density engineering) or the matter-wave interference method [25, 26]. Alternatively, dark solitons can be created by dragging an obstacle sufficiently fast through a condensate [27].

The phase imprinting technique used to create dark solitons is also important in the context of bright solitons as it allows one to investigate the role of relative phase in binary soliton collisions (as discussed in section 2.5.2). Phase imprinting allows the manipulation of the condensate phase but leaves the density unaltered. Experimentally this is done by illuminating part of the condensate with a short pulse of off-resonant light. In this process the wavefunction of the condensate acquires a phase factor $e^{-i\phi}$ [23] where the phase ϕ can be spatially varying and is proportional to the product of the local AC Stark shift and the pulse length.

Gap solitons

The use of attractive condensates to form bright solitons has the unfortunate limitations that the atom number achievable in the condensate is restricted and that only species with suitable tunable interactions can be used.

However, gap bright soliton-like structures can be created for both repulsive and attractive [28] condensates formed in optical lattices. Here the presence of the periodic potential leads to a modification of the linear dispersion relation which can in turn, influence the effective mass.

Gap solitons have been realised in condensates with repulsive interactions [29] where it is possible to create an object with negative effective mass ($m^* = \hbar^2[d^2E/dp^2]^{-1}$), effectively rendering the interaction term of the GPE attractive and thus permitting the formation of bright solitons.

1.2 Previous work

In this section we give a very brief overview of work previously carried out in other groups on the production of ^{85}Rb Bose-Einstein condensates and the formation of bright matter-wave solitons. Further details of these experiments, and others, are included in the subsequent chapters.

1.2.1 Production of ^{85}Rb Bose-Einstein condensates

Despite the broad Feshbach resonance present in the $F = 2, m_F = -2$ state of ^{85}Rb making it highly suited to experiments requiring tunable BECs, previous work using this particular isotope of rubidium to produce a condensate has been somewhat limited. At the time of writing only 3 other machines capable of producing a ^{85}Rb Bose-Einstein condensate have been built, two of which were by the same group at JILA, Colorado [30] and the third at Australia National University, Canberra [31].

The first realisation of ^{85}Rb Bose-Einstein condensation was carried out by the Wieman group at JILA in 2000. Here atoms were cooled directly in a Ioffe-Pritchard magnetic trap [32], exploiting the variation of the elastic and inelastic scattering rates close to the 155 G Feshbach resonance to maximise the efficiency of the evaporation. To reduce detrimental three-body loss rates, trap frequencies were kept low ($\nu_{\text{radial}} = 17.5$ Hz, $\nu_{\text{axial}} = 6.8$ Hz) with the result that evaporation proceeded slowly, taking 120 s to cool atoms from 45 μK to 2 μK. This method produced condensates of $\sim 10^4$ atoms at 162.3 G with smaller condensates also formed within the surrounding 3 G window.

In an attempt to improve on this condensate number the next generation of the experiment tackled the problems associated with cooling ^{85}Rb by employing a second species to act as a refrigerant, sympathetically cooling the atoms [33]. The refrigerant chosen was the more commonly used ^{87}Rb isotope. An additional change to the apparatus was to transfer atoms into an optical dipole trap allowing independent control over the magnetic bias field and the trap frequencies. Using this system condensates of around 8×10^4 atoms could be formed.

At the Australian National University the Close group realised ^{85}Rb BEC

in 2010, also using sympathetic cooling with ^{87}Rb. A large volume optical dipole trap in combination with a pair of Feshbach coils allowed BECs of 4×10^4 to be attained.

1.2.2 Experiments with ^{85}Rb Bose-Einstein condensates

The first experiments carried out with the JILA condensate explored the effect on the condensate dynamics of tuning the interactions from repulsive to attractive. As predicted by theory, beyond some critical value of the scattering length a collapse was initiated causing massive atom loss from the condensate [34, 35]. As we shall see in chapter 7 the remnant of this collapse was later found to contain bright solitary matter-waves [7].

Again exploiting the 155 G resonance, the condensate was also used to investigate quantum superpositions of atoms and diatomic molecules created using a time varying magnetic field to tune the interparticle interactions [36]. In doing so, the binding energy of molecular states could be measured [37] leading to a more accurate characterisation of the Feshbach resonance. In the next generation experiment dual species condensates of ^{85}Rb and ^{87}Rb [33] were created using the method of sympathetic cooling, thus allowing the miscibility of the condensates to be probed.

Work in the ANU group also focussed on the collapse dynamics, attempting to develop a better understanding of the system. Models of the collapse using the Gross-Pitaevski equation (GPE) with the inclusion of a three body loss term were found to be in good agreement with new experimental data, predicting the collapse time for the process and setting new bounds on the three body loss coefficient, K_3 [38]. In addition, studies of inelastic loss in all five Zeeman sublevels of the $F = 2$ manifold were carried out [39].

1.2.3 Observation of bright solitary matter-waves

The formation of bright matter-wave solitons was first observed in Bose-Einstein condensates of lithium. In two inherently similar experiments, very different results were obtained. Experiments carried out at ENS (Paris) re-

sulted in a single soliton, seen to propagate 1.1 mm along an optical waveguide with a weakly expulsive potential [40]. In contrast to this, results from Rice University (Texas) showed trains of multiple solitons being formed, also propagating in a waveguide and interacting repulsively with each other [5].

Four years after these initial observations it was found that the same experiment at JILA first used to demonstrate tunable interactions in a Bose-Einstein condensate was also capable of producing multiple solitons. The collapse of the attractive condensate studied previously produced a stable remnant which, in a similar fashion to the Rice experiment, took the form of multiple bright matter-wave solitons [7].

1.3 Motivation: Open questions

Previous observations of bright matter-wave solitons sparked a great deal of theoretical interest in the dynamics of these wavepackets. Although a huge body of work already existed, the interactions *between* the trapped solitons raised many fascinating questions. Simulations of the system using the GPE formalism could explain the observed behaviour, however only with the inclusion of a relative phase between neighbouring solitons [41, 9]. If this was indeed the correct description, the origin of this phase would be an obvious conundrum to be considered. However, alternative work postulated that the addition of quantum fluctuations could be sufficient to explain the observed repulsive interaction between colliding soliton pairs [10]. The development of many-body theories has also added an extra dimension to the debate, suggesting the emergence of 'fragmentons' [42], distinctly different objects to the solitons predicted by mean-field theories.

With the theoretical community divided over the true description of both soliton formation and collisional dynamics there is an obvious desire to generate more experimental data in order to test theoretical models. This provides one of the key motivations for the work discussed in this thesis. By creating a reproducible, tunable ^{85}Rb BEC from which to form bright solitary matter-waves, collisional dynamics can be investigated in a controlled fashion. Using phase imprinting techniques to manipulate collisions, it should

then be possible to extract information which could lead to a more complete understanding of soliton-soliton interactions.

In future work the self-trapped and stable nature of solitons could see the wavepackets used as probes of short-range forces such as that between an atom and a surface. In this context, solitons make ideal candidates for the observation of quantum effects such as quantum reflection from a surface [3].

1.4 Context of this thesis

This thesis describes the development of an optical trap suitable for the production of Bose-Einstein condensates of ^{85}Rb. The characterisation of the trap using ^{87}Rb is presented, along with the optimisation of the ^{85}Rb condensation routine. The loading of a quasi-1D optical waveguide is discussed, along with the method of bright solitary matter-wave formation.

Throughout this work we focus solely on the optical trapping stages of the experiment. The preliminary stages of the experimental routine (namely the MOT, magnetic trap loading, magnetic transport and RF evaporation in a quadrupole trap) and their optimisation are discussed in the thesis of Sylvi Händel (SH) [43] and, to avoid repetition, are not presented again here.

The building of the laser cooling system was carried out by SH, along with the construction of the magnetic coils and transport apparatus. The assembly of the MOT optical setup and the optical dipole traps was carried out by ALM and SH. The optimisation of the apparatus, to the point of ^{87}Rb condensation, was performed by ALM and SH. (Note, details of the experimental control system also developed during this time can be found in the thesis of Timothy Wiles (TW).) Further characterisation of the crossed dipole trap was completed by ALM and TW. The subsequent cooling of ^{85}Rb and the formation of bright solitary matter-waves was carried out by ALM.

1.5 Thesis outline

The work presented in this thesis aims to give a chronological review of the steps taken to successfully achieve Bose-Einstein condensation of ^{85}Rb along with the formation of bright solitary matter-waves from the condensate.

- Following the overview of previous experimental work on ^{85}Rb Bose-Einstein condensates and bright solitary-matter-waves presented in this chapter we begin by considering some of the theoretical background relevant to the results discussed in this thesis. These are presented in chapter 2.

- In chapter 3 we introduce the experimental apparatus used throughout this work. In addition to the technical details of the experimental sequence, some basic theory of the optical trap is included.

- Chapter 4 contains details of a single beam optical dipole trap suitable for producing Bose-Einstein condensates of ^{87}Rb. We demonstrate that atoms in this trap can be controllably transported along the beam. By guiding atoms up to a room temperature test surface positioned within our glass science cell we show that this process can be used as a method of evaporative cooling.

- In chapter 5 we present the implementation and characterisation of a crossed dipole trap better suited to the formation of ^{85}Rb condensates. We discuss three distinct trap configurations and the evaporation in each case. We go on to produce Bose-Einstein condensates of ^{87}Rb in each of the traps before using the crossed trap geometry to produce a 1D optical lattice. We demonstrate condensation in the lattice, again using ^{87}Rb, and observe Kaptiza-Dirac scattering from a deep lattice potential.

- In chapter 6 we discuss the scattering properties of ^{85}Rb and the difficulty associated with evaporative cooling. We then go on to present our method of direct cooling in the crossed dipole trap to efficiently reach degeneracy in ^{85}Rb. We demonstrate the tunable atomic interactions of the condensate close to the 155 G Feshbach resonance and show that

the condensate undergoes collapse if the interactions are tuned to be strongly attractive.

- In chapter 7 we load the ^{85}Rb condensate into a quasi-1D waveguide. By again tuning the atomic interactions we are able to realise bright solitary matter-waves which we observe to propagate along the waveguide beam. Using a broad, repulsive Gaussian barrier we demonstrate classical reflection of the solitary wave and contrast this to the case of a repulsive condensate.

- Finally in chapter 8 we give an outlook to future work and some of the open questions to be explored using this system.

1.6 Publications

Work related to this thesis

[44] S. Händel, A. L. Marchant, T. P. Wiles, S. A. Hopkins, and S. L.Cornish, *Magnetic transport apparatus for the production of ultracold atomic gases in the vicinity of a dielectric surface*, Rev. Sci. Instrum. **83**, 013105 (2012), gives further details of the experimental apparatus presented in chapter 3.

[45] A. L. Marchant, S. Händel, T. P. Wiles, S. A. Hopkins and S. L. Cornish, *Guided transport of ultracold gases of rubidium up to a room-temperature dielectric surface*, New J. Phys. **13** 125003 (2011), provides the basis for chapter 4.

[46] A. L. Marchant, S. Händel, S. A. Hopkins, T. P. Wiles, and S. L. Cornish, *Bose-Einstein condensation of ^{85}Rb by direct evaporation in an optical dipole trap*, Phys. Rev. A **85**, 053647 (2012), forms the basis of chapter 6.

[47] A. L. Marchant, T. P. Billam, T. P. Wiles, M. M. H. Yu, S.A. Gardiner and S. L. Cornish, *Controlled formation and reflection of a bright solitary matter-wave*, Nat. Commun. **4**, 1865 (2013), contains details of the work

presented in chapter 7.

Other work

[48] A. L. Marchant, S. Händel, T. P. Wiles, S. A. Hopkins, C. S. Adams and S. L. Cornish, *Off-resonance laser frequency stabilization using the Faraday effect*, Opt. Lett. **36**, 64 (2011), describes work to develop a locking scheme suitable for use in degenerate Raman sideband cooling, potentially as an alternative route towards quantum degeneracy. This is included as an appendix.

[49] S. Händel, T. P. Wiles, A. L. Marchant, S. A. Hopkins, C. S. Adams, and S. L. Cornish *Magnetic merging of ultracold atomic gases of* ^{85}Rb *and* ^{87}Rb, Phys. Rev. A **83**, 053633 (2011), describes experiments carried out using the same apparatus used for this work to controllably merge magnetic traps thus allowing multiple loading of one or more atomic species.

[50] T. P. Billam, A. L. Marchant, S. L. Cornish, S. A. Gardiner, N.G. Parker, *Bright solitary matter waves: formation, stability and interactions*, in Progress in optical science and photonics, Vol. 1, Spontaneous symmetry breaking, self-trapping, and Josephson oscillations, Springer (2013), contains a review of the current theoretical work in the field, along with experimental results to date as covered in sections 6.7.1 and 7.1.1.

Chapter 2

Theoretical background

2.1 Introduction

In this chapter we present a brief overview of the physics governing Bose-Einstein condensates and bright solitons. We discuss the effect of interparticle interactions in a condensate and how, in reduced dimensions, attractive interactions can lead to the formation of bright solitons. We conclude by looking at some of the potential explanations for the formation of bright solitary waves in experiments and the role of relative phase in binary solitary wave collisions.

2.2 Bose-Einstein condensation

The phenomena of Bose-Einstein condensation corresponds to the macroscopic occupation of a single quantum state due to the quantum statistics governing indistinguishable bosons. This occurs at low temperatures where there is a significant overlap of the thermal deBroglie wavelength of the atoms in the gas,

$$\lambda_{\mathrm{dB}} = \sqrt{\frac{2\pi\hbar^2}{mk_{\mathrm{B}}T}}, \tag{2.1}$$

or equivalently when the phase space density (PSD),

$$\mathrm{PSD} = n_0\lambda_{\mathrm{dB}}^3, \tag{2.2}$$

exceeds 2.61. Here n_0 is the condensate density. In a trap, this leads to the idea of a critical temperature T_c, dependent on the atom number N and the trapping frequency ω. In a harmonic, isotropic trap this is given by [51]

$$k_B T_c = 0.94 N^{1/3} \hbar\omega. \tag{2.3}$$

Bose-Einstein condensation was first predicted in 1924 following the collaborative efforts of Bose and Einstein. Bose's work considered the statistics of photons [52] which Einstein then developed in the context of a gas containing a fixed number of non-interacting, massive bosons. It was shown that below some critical temperature a non-zero fraction of the bosons would fall into the lowest-energy single-particle state [53]. In reaching this conclusion an entirely new field of atomic physics was born.

Despite the advent of laser cooling in the mid 1970s, it wasn't until 1995 that this new state of matter was experimentally realised in gases of rubidium [54], sodium [55] and lithium [56]. Although laser cooling techniques could produce samples at tens of μK [57] the temperature of the trapped clouds was neither cold enough nor the density high enough for condensation to occur. Only the addition of evaporative cooling [58, 59] stages, taking the lead from work on spin polarized hydrogen, allowed access to this new temperature regime.

The low temperatures of Bose-Einstein condensates allow the exploration of quantum phenomena. Despite being dilute[1], atomic interactions play a huge role in the dynamics of the system. However, the diluteness makes the treatment of interactions theoretically tractable in terms of simple two-body physics. Indeed, the dilute gases used to produce Bose-Einstein condensates are well described by the mean-field Gross-Pitaevskii formalism. The fact that these interactions can be controlled or tuned, either by the choice of atom or by means of Feshbach resonances [14] where present, makes atomic Bose-Einstein condensates extremely attractive systems to work with.

Condensates which exhibit some sort of Feshbach structure allow the experimenter full control over the s-wave scattering properties of the atoms. The scattering length of the atoms, a_s, which characterises elastic collisions

[1]Typical condensate densities are of the order $10^{13} - 10^{15}$ cm^{-3} whereas the molecules in air at room temperature and atmospheric pressure have densities of $\sim 10^{19}$ cm^{-3} [60].

may then be tuned over many orders of magnitude and, most interestingly, even changed in sign. Control of the atomic interactions in this way, coupled with the ability to produce condensates in almost entirely arbitrary geometries makes Bose-Einstein condensates ideal systems in which to study the formation of bright solitary matter-waves.

2.3 The Gross-Pitaevskii equation

The Gross-Pitaevskii equation (GPE) is a wave equation which describes a many body wavefunction. It accurately describes gaseous Bose-Einstein condensates in the limit that [50]:

- The number of particles in the condensate is large, $N \gg 1$, i.e. the condensate is macroscopically populated.
- The temperature of the gas is lower than T_c, the critical temperature i.e. $T < T_c$. As such, the thermal fraction of atoms is small.
- Short-range two-body interactions, characterised by the s-wave scattering length a_s, dominate.
- The interactions are weak $n|a_s|^3 \ll 1$ and small fluctuations have no effect. In this limit the shape of the interatomic potential becomes unimportant and can be approximated as a contact potential of the form

$$U(\mathbf{r} - \mathbf{r}') = \frac{4\pi\hbar^2 a_s}{m}\delta(\mathbf{r} - \mathbf{r}'). \tag{2.4}$$

The success of this treatment relies upon the fact that, in the ultracold limit, collisions can be parameterised by a single quantity, the scattering length. In this ultracold limit atoms scatter like hard spheres. In low energy collisions (where only the $l = 0$ partial wave is important) the deBroglie wavelength of the atoms is much larger than the short-range molecular potential associated with the two-atom bound state. As such, the atoms do not 'see' the shape of the potential and only a phase shift of the scattered wavefunction can be observed as shown in Fig. 2.1. This phase shift can be translated into the

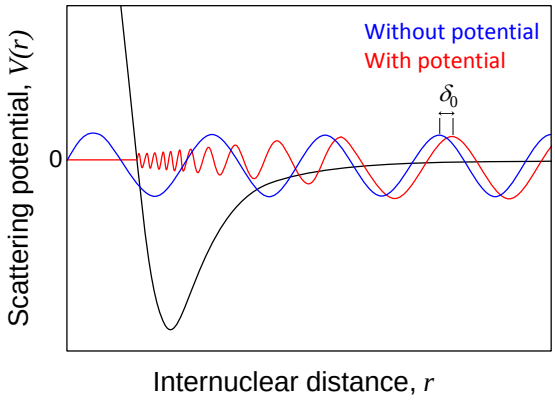

Figure 2.1: Effect of scattering from a molecular potential in the ultracold limit: At long range the scattered wave is phase shifted relative to the case of scattering from a point like object at $r = 0$. Scattering from the potential $V(r)$ is indistinguishable from that of a hard sphere.

scattering length, a_s,

$$a_s = -\lim_{k\to 0} \frac{\tan \delta_0(k)}{k} \tag{2.5}$$

which can be thought of as the radius of the hard sphere. Here δ_0 is the phase shift of the $l = 0$ partial wave and k is the wavevector [61].

2.3.1 Mean-field theory and the order parameter

If we consider N spinless bosons, characterised by spatial coordinates $\mathbf{r}$, the many-body Hamiltonian is given in second quantisation by [62]

$$\begin{aligned} \hat{H} = \int d\mathbf{r} \quad & \hat{\Psi}^\dagger(\mathbf{r}) \left[-\frac{\hbar^2}{2m}\nabla^2 + V_{\text{ext}}(\mathbf{r}) \right] \hat{\Psi}(\mathbf{r}) \\ + \quad & \frac{1}{2} \int \int d\mathbf{r} d\mathbf{r}' \hat{\Psi}^\dagger(\mathbf{r}) \hat{\Psi}^\dagger(\mathbf{r}') V(\mathbf{r} - \mathbf{r}') \hat{\Psi}(\mathbf{r}') \hat{\Psi}(\mathbf{r}). \end{aligned} \tag{2.6}$$

$\hat{\Psi}(\mathbf{r})$ and $\hat{\Psi}^\dagger(\mathbf{r})$ are bosonic field operators that annihilate and create particles at the position $\mathbf{r}$. $V(\mathbf{r} - \mathbf{r}')$ is the two-body interaction potential.

In the mean field description, one can separate out the contributions to the bosonic field operator, expressing it as a sum of single particle wave functions $\Psi_\alpha(\mathbf{r})$, multiplied by the corresponding annihilation operators a_α such that,

$$\hat{\Psi}(\mathbf{r}) = \sum_\alpha \Psi_\alpha(\mathbf{r}) a_\alpha. \tag{2.7}$$

To generalise this to the nonuniform, time-dependent case, we have

$$\hat{\Psi}(\mathbf{r},t) = \Phi(\mathbf{r},t) + \hat{\Psi}'(\mathbf{r},t), \tag{2.8}$$

where $\Phi(\mathbf{r},t)$ is a classical field or order parameter and $\hat{\Psi}'(\mathbf{r},t)$ is a small fluctuation. This 'wave function of the condensate' is a complex function and is defined as $\Phi(\mathbf{r},t) = \langle\hat{\Psi}(\mathbf{r},t)\rangle$. The order parameter can also be expressed in terms of the condensate density, $n_0(\mathbf{r},t) = |\Phi(\mathbf{r},t)|^2$.

Writing the time evolution of the field operator $\Phi(\mathbf{r},t)$ using the Heisenberg equation with the many-body Hamiltonian given in Eq. (2.6), it is possible to derive an equation for the condensate wave function,

$$\begin{aligned} i\hbar\frac{\partial}{\partial t}\hat{\Psi}(\mathbf{r},t) &= [\hat{\Psi},\hat{H}] \\ &= \left[-\frac{\hbar^2\nabla^2}{2m} + V_{\text{ext}}(\mathbf{r})\right]\hat{\Psi}(\mathbf{r},t) \\ &\quad + \left[\int d\mathbf{r}'\hat{\Psi}^\dagger(\mathbf{r}',t)\times V(\mathbf{r}-\mathbf{r}')\hat{\Psi}(\mathbf{r}',t)\right]\hat{\Psi}(\mathbf{r},t), \end{aligned} \tag{2.9}$$

where the field operator must then be replaced with the classical field Φ.

Next we consider the two-body potential $V(\mathbf{r}-\mathbf{r}')$ at very low temperature. If the interactions only occur on length scales much shorter than the typical interparticle separations we can approximate the interaction by a Dirac delta-function

$$V(\mathbf{r}-\mathbf{r}') = g\delta(\mathbf{r}-\mathbf{r}'), \tag{2.10}$$

where we introduce the effective interaction constant

$$g = 4\pi\hbar^2 a_s/m, \tag{2.11}$$

which relates the interaction to the scattering length a_s. Using this effective potential in Eq. (2.9) allows the replacement of $\hat{\Psi}$ with Φ, thus we arrive at,

$$i\hbar\frac{\partial}{\partial t}\Phi(\mathbf{r},t) = \left(-\frac{\hbar^2\nabla^2}{2m} + V_{\text{ext}}(\mathbf{r}) + g|\Phi(\mathbf{r},t)|^2\right)\Phi(\mathbf{r},t). \tag{2.12}$$

This is the Gross-Pitaevskii equation.

The contributions to Eq. (2.12) can be written in terms of their respective energies,

$$E = E_{\text{kin}} + E_{\text{ho}} + E_{\text{int}}. \tag{2.13}$$

Here, the kinetic energy, or *quantum* kinetic energy, $E_{\rm kin}$, arises as a result of the uncertainty principle (and vanishes for the case of a uniform system), the harmonic oscillator energy, $E_{\rm ho}$, is due to the trapping potential and the mean-field interaction energy, $E_{\rm int}$, is a result of the interparticle interactions.

2.3.2 The healing length

The balance between the kinetic energy and the interaction energy of the condensate can be used to describe a typical length scale, the healing length ξ. This is the distance over which the BEC wavefunction 'heals' over defects. If the BEC density grows from 0 to n over a distance ξ, the kinetic energy $\sim \hbar^2/(2m\xi^2)$ and interaction energy $\sim 4\pi\hbar^2 a_s n/m$ become equal at the healing length,

$$\xi = (8\pi n a_s)^{-1/2}. \tag{2.14}$$

We shall see in section 2.4 that this length becomes important in the context of lower dimensional systems.

2.3.3 Interparticle interactions

The strength of interparticle interactions, relative to the kinetic energy of the condensate, plays an important role in the structure and dynamics of the trapped gas. The interaction energy is given by gNn where the average density $n \sim N/a_{\rm ho}^3$ and $a_{\rm ho} = (\hbar/m\omega)^{1/2}$. This means that the interaction energy scales as $E_{\rm int} \propto N^2|a_s|/a_{\rm ho}^3$. The kinetic energy of the condensate is given by $N\hbar\omega_{\rm ho}$. Here $\omega_{\rm ho} = \hbar/(ma_{\rm ho}^2)$ thus $E_{\rm kin} \propto N a_{\rm ho}^{-2}$. This gives us the relation,

$$\frac{E_{\rm int}}{E_{\rm kin}} \propto \frac{N|a_s|}{a_{\rm ho}}, \tag{2.15}$$

allowing us to determine the importance of the interaction energy, relative to the kinetic energy. Even if $n|a_s|^3 \ll 1$ (the condition for the validity of the GPE) Eq. (2.15) can still be much greater than 1, hence a dilute gas can still be strongly interacting, exhibiting nonlinear behaviour.

A system of noninteracting bosons confined in a harmonic trap will take the form of a Gaussian with average width $a_{\rm ho,i} = (\hbar/m\omega_i)^{1/2}$ and a peak density

proportional to N. However, in the presence of interactions, the shape of the condensate is modified. This change in shape can be dramatic if the interactions energy is much greater than the kinetic energy, that is [62],

$$\frac{Na_s}{a_{\text{ho}}} \gg 1. \tag{2.16}$$

For repulsive $a_s > 0$ (attractive $a_s < 0$) interactions the peak density decreases (increases) and the condensate spreads (contracts).

In systems exhibiting some sort of Feshbach structure it is possible to tune the atomic scattering properties, i.e. the interactions, using magnetic or optical fields [14]. Further discussion of magnetic Feshbach resonances can be found in section 6.3.2.

Noninteracting solution: The ground state

The ground state of the GPE can easily be found by substituting an expression for the condensate wavefunction, $\Phi(\mathbf{r}) = \phi(\mathbf{r})\exp(-i\mu t/\hbar)$, into Eq. (2.12). ϕ is real and normalised to the number of atoms such that $\int d\mathbf{r}|\phi|^2 = N$. This gives us

$$\left(-\frac{\hbar^2}{2m}\nabla^2 + V_{\text{trap}}(\mathbf{r}) + \frac{4\pi a_s\hbar^2}{m}|\phi(\mathbf{r})|^2\right)\phi(\mathbf{r}) = \mu\phi(\mathbf{r}). \tag{2.17}$$

Here the nonlinear aspect of this nonlinear Schrödinger equation is provided by the mean field term, proportional to the particle density, $n(\mathbf{r}) = |\phi|^2(\mathbf{r})$. μ is the chemical potential. In the absence of interactions, $a_s = 0$, Eq. (2.17) reduces to a the single particle Schrödinger equation, the solution to which is a simple Gaussian function,

$$\phi(\mathbf{r}) = \sqrt{N}\left(\frac{m\omega_{\text{ho}}}{\pi\hbar}\right)^{3/4}\exp\left[-\frac{m}{2\hbar}(\omega_x^2x^2 + \omega_y^2y^2 + \omega_z^2z^2)\right], \tag{2.18}$$

where $\omega_{\text{ho}} = (\omega_x\omega_y\omega_z)^{1/3}$.

Repulsive interactions: The Thomas-Fermi approximation

Most experiments operate in the regime $Na_s/a_{\text{ho}} \gg 1$ where interactions are repulsive. As Na_s/a_{ho} increases atoms are pushed further from the trap centre as the condensate spreads creating a slow spatial variation of the

density. As a result, the kinetic energy of the condensate, which scales as $\sqrt{n}$, becomes small when compared to the interaction energy, only becoming significant again close to the boundary. One can then entirely neglect the kinetic term of the Hamiltonian. This is referred to as the Thomas-Fermi approximation. The density profile of the trapped condensate is thus given by

$$n(\mathbf{r}) = \frac{\mu - V_{\text{trap}}(\mathbf{r})}{g}, \tag{2.19}$$

for the region $\mu > V_{\text{trap}}(\mathbf{r})$ [62]. Outside this region the density is zero.

In the Thomas-Fermi limit the chemical potential takes the form

$$\mu = \frac{\hbar\omega_{\text{ho}}}{2}\left(\frac{15Na_s}{a_{\text{ho}}}\right)^{2/5}. \tag{2.20}$$

From Eq. (2.19) we can see that the density profile of the condensate reflects the form of the trapping potential. For a harmonic trap this produces an inverted parabola, vanishing at position $\mathbf{R}$, defined by $\mu = V_{\text{trap}}(\mathbf{R})$. If we take the case of a spherically symmetric trap we have $\mu = m\omega_{\text{ho}}^2 R^2/2$. Substituting in the value for the chemical potential given by Eq. (2.20) we arrive at an expression for the radius of the condensate,

$$R = a_{\text{ho}}\left(\frac{15Na_s}{a_{\text{ho}}}\right)^{1/5}. \tag{2.21}$$

Attractive interactions: Collapse instability

A trapped attractively interacting condensate tends to increase its density at the trap centre, thus minimising its interaction energy. This contraction can be balanced by the kinetic energy of the gas if the interactions are sufficiently weak or the atom number is sufficiently low. Beyond this, the kinetic energy can no longer stabilise the condensate and collapse occurs. Incidentally, in a uniform, untrapped gas the absence of this kinetic energy (or quantum pressure) means all attractive condensates are unstable, irrespective of atom number or interaction strength.

The stability of the trapped condensate can be parameterised by k, given by [13]

$$k = \frac{N_c|a_s|}{a_{\text{ho}}}. \tag{2.22}$$

The value of k can be calculated numerically and is determined by both the trapping strength and geometry. For a spherical trap, numerical integration of the GPE gives $k \approx 0.57$ [13] whereas for a waveguide, typically used to produce solitary waves, the same GPE treatment yields a value of $k \approx 0.675$ [63].

If the number of atoms in the condensate exceeds the critical value N_c, set by k, the system will undergo collapse in both 2D and 3D [64, 60]. In a true 1D geometry, collapse is prohibited. However, in quasi-1D systems the finite radial trapping means it is possible to produce stable attractive condensates provided the number of atoms remains *below* some threshold, this time set by a slightly modified version of Eq. (2.22),

$$k_{\mathrm{1D}} = \frac{N_c|a_s|}{a_{\mathrm{ho,r}}}. \tag{2.23}$$

Here $a_{\mathrm{ho,r}}$ is the radial harmonic oscillator length [65, 66, 67, 68]. This expression for the stability parameters using only the radial harmonic oscillator length means one can readily consider the case of $\omega_{\mathrm{axial}} = 0$ in calculations.

Insight into the behaviour of an attractively interacting gas can be gained from a variational approach based on Gaussian functions. The results of such an analysis are presented in section 2.3.4.

2.3.4 Variational analysis of the GPE

If we consider the case of no interparticle interactions the lowest single-particle state can be described by the wavefunction [60]

$$\phi_0 = \frac{1}{\pi^{3/4}(a_x a_y a_z)^{1/2}} e^{-x^2/2a_x^2} e^{-y^2/2a_y^2} e^{-z^2/2a_z^2}. \tag{2.24}$$

Here $a_i^2 = \hbar/m\omega_i$ are the oscillator lengths in three directions ($i = x, y, z$). However, in the presence of interactions the cloud begins to change shape and this wavefunction no longer provides an accurate description. Instead we introduce a trial wavefunction, chosen to be a Gaussian of the same form [68],

$$\psi(\mathbf{r}) = \frac{1}{\pi^{3/4}(a_x a_y a_z b_x b_y b_z)^{1/2}} e^{-x^2/2a_x^2 b_x^2} e^{-y^2/2a_y^2 b_y^2} e^{-z^2/2a_z^2 b_z^2}, \tag{2.25}$$

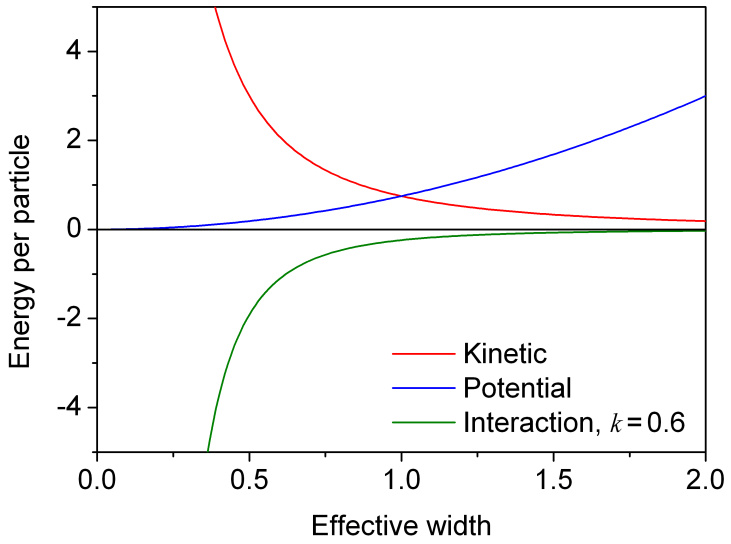

Figure 2.2: Dependence on effective width of the kinetic, potential and interaction (k=0.6) energy contributions of a harmonically trapped BEC: The energy per particle is given in units of $\hbar\omega$.

which contains the variational parameters, b_i. Such an ansatz has been considered previously for bright solitary matter-waves [69, 63, 68] and is most appropriate when the trapping strength dominates the interactions. Substituting Eq. (2.25) into the energy functional

$$E(\psi) = \int d\mathbf{r} \left[\frac{\hbar^2}{2m} |\nabla\psi(\mathbf{r})|^2 + V(\mathbf{r})|\psi(\mathbf{r})|^2 - \frac{2\pi N|a_s|\hbar^2}{m} |\psi(\mathbf{r})|^4 \right], \qquad (2.26)$$

where $V(r) = m\omega^2(x^2 + y^2 + z^2)/2$, one can show that the energy of the system is given by

$$E(b_x, b_y, b_z) = \sum_i \hbar\omega_i \left(\frac{1}{4b_i^2} + \frac{b_i^2}{4} \right) - \frac{N|a_s|}{\sqrt{2\pi} a_{\rm ho} b_x b_y b_z}. \qquad (2.27)$$

From this analysis we can see the dependence on the effective width, b, of the various energy contributions for an isotropic trap ($b = b_x = b_y = b_z$): kinetic $\sim 1/b^2$, trapping potential $\sim b^2$, interaction $\sim -1/b^3$, also illustrated in Fig. 2.2. The energy per particle, in units of $\hbar\omega$ is shown in Fig. 2.3 as a function of the effective width for various values of $k = N|a_s|/a_{\rm ho}$. We can see that for negative scattering lengths being considered here, a local energy minimum exists provided that N remains below some critical value N_c. Beyond this, the condensate collapses.

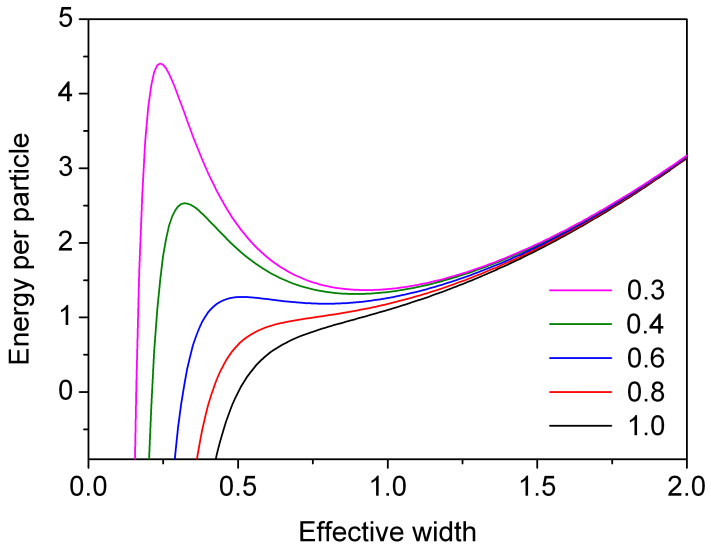

Figure 2.3: Variational expression for the energy per particle in a isotropic, harmonic trap: Energy per particle (in units of $\hbar\omega$) is given as a function of the variational parameter, the effective width b, for various values of $k = N|a_s|/a_{\mathrm{ho}}$

.

This variational analysis returns a value of $k \approx 0.671$ for a spherical trap. Here the local minimum in the energy disappears and the condensate collapses. This is in reasonable agreement with the full GPE calculation, confirming that the method can indeed provide valuable insight into the behaviour of attractive gases without the need for intensive calculations.

2.4 Quasi-1D models

Experiments focussed on soliton formation usually employ elongated, prolate traps with $\omega_x = \omega_y = \omega_r \gg \omega_z$. If the harmonic oscillator length associated with this radial direction $a_{\mathrm{ho,r}} = \sqrt{\hbar/m\omega_r} < \xi$ the confinement becomes sufficiently tight such that the higher energy radial modes are effectively 'frozen out' and the system can be considered quasi-1D. The full 3D GPE description of this cigar-shaped condensate can then be reduced to the much simpler 1D case provided ω_z/ω_r is sufficiently small.

In this 1D limit the coupling constant g, describing the interparticle interactions, is modified such that [70],

$$\tilde{g} = \frac{g}{2\pi a_r^2} = 2\hbar\omega_r a_s. \tag{2.28}$$

The trapping potential is also simplified to $V_{\text{trap}}(z) = (1/2)m\omega_z^2 z^2$.

2.5 Soliton solutions to the 1D GPE

In 1D the GPE for a BEC with scattering length a_s in a trapping potential $V(z,t)$, is given by

$$i\hbar\frac{\partial\psi}{\partial t} + \frac{\hbar^2}{2m}\frac{\partial^2\psi}{\partial z^2} - V(z,t)\psi - \tilde{g}(z,t)|\psi|^2\psi = 0, \tag{2.29}$$

where the interaction term $\tilde{g}(z,t) = 2\hbar\omega_r a_s$.

In the absence of trapping ($V(z,t) = 0$) and when the atomic interactions are attractive, $a_s < 0$ Eq. (2.29) admits bright soliton solutions of the form [70]

$$\psi(z,t) = \frac{a_r}{\sqrt{2|a_s|\kappa}}\text{sech}\left(\frac{z-vt}{\kappa}\right)\exp\left[i\frac{mv}{\hbar}z - \frac{i}{\hbar}\left(\frac{mv^2}{2} - \frac{\hbar^2\kappa^2}{2m}\right)t\right]. \tag{2.30}$$

Here $a_{\text{ho,r}} = \sqrt{\hbar/(m\omega_r)}$, v is the soliton velocity and

$$\kappa = \frac{a_r^2}{|a_s|N} \tag{2.31}$$

is the soliton width. (Here it is assumed that the soliton width in the radial direction is set by the harmonic oscillator ground state.) Eq. (2.29) is only valid when $|a_s|N/a_r \ll 1$ which implies that $a_r \ll \kappa$.

In real experiments, this quasi-1D geometry is usually accompanied by the presence of weak axial harmonic trapping, $V(z,t) = (1/2)m\omega_z^2 z^2$. This removes the integrability of the system and prevents the appearance of true solitons. However, *bright solitary wave* solutions may still be supported. Although these do not comply with the strict mathematical definition of a true soliton, they can be considered soliton like in that they are non-dispersive due to their attractive interactions, are robust to collisions with other solitary waves and their dynamics can be described using particle-likes models [71, 72].

It is still the case that one expects only to observe solitary matter-waves in quasi-1D geometries. However, the observation of bright solitary matter-waves in an almost fully 3D system [7] raises the interesting question of how 1D a system must be in order to admit these solitary wave objects.

2.5.1 Bright solitary wave formation: Modulational instability

The mechanism for the formation of bright solitary matter-waves and the creation of a relative phase $\Delta\phi$ between neighbouring wavepackets is still not completely understood. However, the process of modulational instability has been proposed as a possible mechanism to explain these phenomena. Here a constant-wave background becomes unstable to sinusoidal modulations because of the presence of a focusing nonlinearity (i.e. the mean-field interaction $a_s < 0$). Amplitude and phase modulations of the wave grow as a result of an interplay between this nonlinearity and anomalous dispersion [73, 9].

Although there is some general agreement that modulational instability may be responsible for the formation of solitary waves [74, 9], it is still unclear as to whether this can also explain the emergence of a relative phase. In Ref. [9] Carr *et al.* postulate that an initial nonuniform state undergoing modulational instability will produce wavepackets with arbitrary $\Delta\phi$, even in a mean-field treatment. Subsequent secondary collapse processes then lead to a relative phase of $\pi/2 < \Delta\phi < 3\pi/2$ between neighbouring solitons, stabilising them in later collisions. In contrast, Al Khawaja *et al.* attribute the origin of $\Delta\phi$ to phase fluctuations in the condensate. These phases are restricted to values close to $\phi = \pi$ in order to stabilise the wavepackets during collisions as we shall see in section 2.5.2.

2.5.2 Bright solitary wave collisions

It is interesting to consider the effect of collisions on the stability of bright solitary matter-waves oscillating in a trap. Previous experimental results [5, 7] provide a clear motivation for this. In the 1D limit it has been shown

that the force between two colliding solitons depends sinusoidally on their relative phase [12]. If this phase $\Delta\phi = 0$ the solitons interact 'attractively', overlapping freely, whilst for $\Delta\phi = \pi$ the interactions between solitons are 'repulsive' [75]. The collisions are elastic and the relative phase is unaltered by the collision.

In 3D, the potential overlap of two solitary waves can be sufficient to render the system unstable as the critical number for an attractive condensate N_c can be exceeded. In this case, attractive collisions, $\Delta\phi = 0$, can result in a collapse due to the localised increase in density during the collision. Collision dynamics are predicted to depend not only on this relative phase $\Delta\phi$ but also on the velocity of the collision [76]. (Simulations of collisions of two solitons in a time-modulated optical lattice even predict the potential merging of the two into a single soliton for the case of in-phase collisions [77].)

Extensive numerical simulations of the 3D GPE can be used to investigate how collisions depend on key parameters, namely the relative phase, interaction strength and timescale of the collision [41]. In Ref. [41] Parker *et al.* show that collisions of bright solitary waves exhibit rich and non-trivial behaviour, not present for 1D solitons.

The relative phase difference between solitary waves can lead to population transfer between two colliding wavepackets [41, 78], this depending strongly on the incoming velocity and therefore the collision time. Slow, high density collisions can lead to the collapse of the condensate if the collision time, $t_{\text{collision}}$, exceeds the collapse time, t_{collapse}, for the condensate (see section 6.7). The presence of a π relative phase can, however, suppress this instability. In contrast, if $t_{\text{collision}} < t_{\text{collapse}}$ the collision is elastic and independent of $\Delta\phi$.

Just as the stability parameter k determines the stability of an isolated attractively interacting condensate, it is a crucial factor in the stability of collisions of bright solitary matter-waves formed from the condensate. Collisions remain stable for low values of k but become increasingly unstable as $k \to k_c$. Again, a π relative phase can stabilise collisions of this nature as the solitary waves are prevented from overlapping.

2.6 Summary

In this chapter we have briefly reviewed some of the underlying physics of Bose-Einstein condensation and bright solitary matter-waves. We have discussed how, in 3D, an attractive condensate is unstable to collapse however, in the presence of trapping, the kinetic energy of the wavepacket can result in a meta-stable, non-collapsing state. If the trapping geometry is made sufficiently quasi-1D, these attractive condensates can form bright solitary matter-waves, the 3D analogue to the true bright soliton solutions of the 1D GPE.

Chapter 3

Experimental overview

3.1 Introduction

Common to all ultracold gas experiments are a number of key pieces of experimental apparatus. In this chapter we briefly discuss these in the context of our experimental setup and highlight the features designed to allow the production of ultracold gases close to a room temperature surface. A more comprehensive description of the experimental setup and its characterisation can be found in Refs. [44, 43]. Here we focus on the physics governing the optical traps along with typical experimental parameters associated with their implementation.

3.2 Delivery of cold atoms to the science cell

In order to successfully deliver a sample of cold atoms to the science cell we must first trap and cool atoms from a background vapour before loading them into a magnetic trap. These stages of the experimental procedure will not be the focus of this thesis, however a full discussion of the optimisation can be found in [43]. This section provides a brief overview of the key elements associated with the loading of the magnetic transport trap and the delivery of atoms to the science cell.

3.2.1 Vacuum system

The ultimate function of the vacuum system, shown in Fig. 3.1(a), is to enable the study of atom-surface interactions between ^{85}Rb atoms and a super-polished glass Dove prism in an ultra-high vacuum (UHV) environment. As such the system must be capable of maintaining these UHV conditions and designed to minimise the surface 'contamination' of the Dove prism. Optical access close to the prism must also be maximised to allow for a variety of trapping geometries to be explored.

The vacuum chamber can be divided into two parts, the magneto-optical trap (MOT) chamber and the glass science cell housing the super-polished prism (Fig. 3.1(b)), these two being connected via a differential pumping stage. This pumping not only provides the UHV environment at the science cell but also allows the rapid loading of the MOT whilst maintaining long lifetimes for trapped atoms in the science cell. An obstacle, shown in Fig. 3.1(c), (a right angled glass prism) placed along the axis of the system blocks the line of sight between the two ends of the vacuum system. Atoms can be transfered from the MOT chamber to the science cell via magnetic transport (see section 3.2.3) whereby atoms are shifted over this obstacle. By adopting this setup, rather than for example a double MOT system, the surface of the Dove prism is protected from atomic beams of rubidium travelling along the vacuum chamber and we maintain good optical axis at the science cell.

Figure 3.1(a) shows the vacuum chamber prior to the construction of the full apparatus. Visible above the MOT chamber (left of image) is a glass cell housing the rubidium dispensers. This glass surround is designed to potentially allow the implementation of light induced atomic desorption (LIAD) as a means of controlling the rubidium pressure in the MOT chamber [79]. The overall height of the MOT chamber has been minimised to aid the generation of large magnetic fields and gradients. By creating a low profile system the coils used for magnetic transport or to produce bias fields to access Feshbach resonances can be positioned much closer together, hence requiring lower currents to realise the necessary fields.

It should be noted that the vacuum system is housed on a separate optical table to the laser cooling system. This isolates the lasers from any vibrations

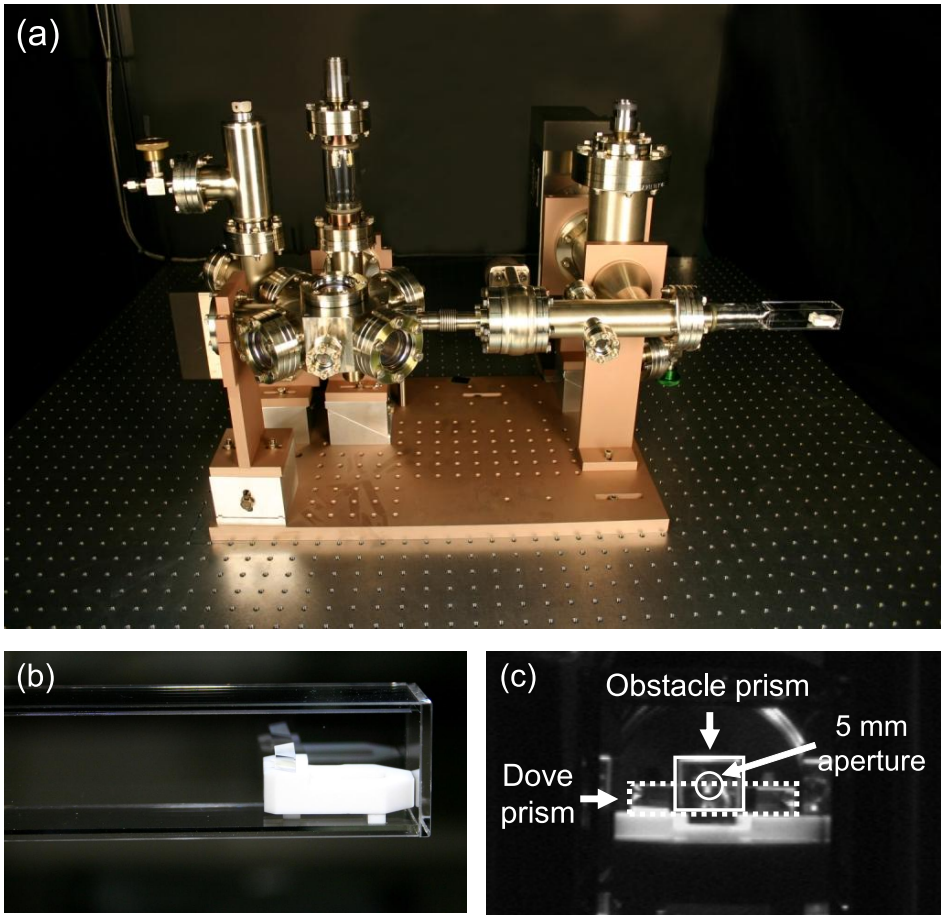

Figure 3.1: Vacuum chamber, obstacle and super polished prisms: (a) To the left of the image is the MOT chamber with viewports for six MOT beams, an optical pumping beam to be retro reflected and a further viewport for fluorescence monitoring of the MOT. To the right is the glass science cell which houses the super-polished Dove prism. The viewport visible part way along the axis of the system allows optical access to the obstacle prism. (b) Super polished Dove prism in the glass science cell. (c) View along the transport axis from the science cell end. In the foreground is the super polished Dove prism in a macor mount and in the background the obstacle prism. The obstacle is centered on a 5 mm aperture out of the MOT chamber, blocking the line of sight between the MOT and the Dove prism.

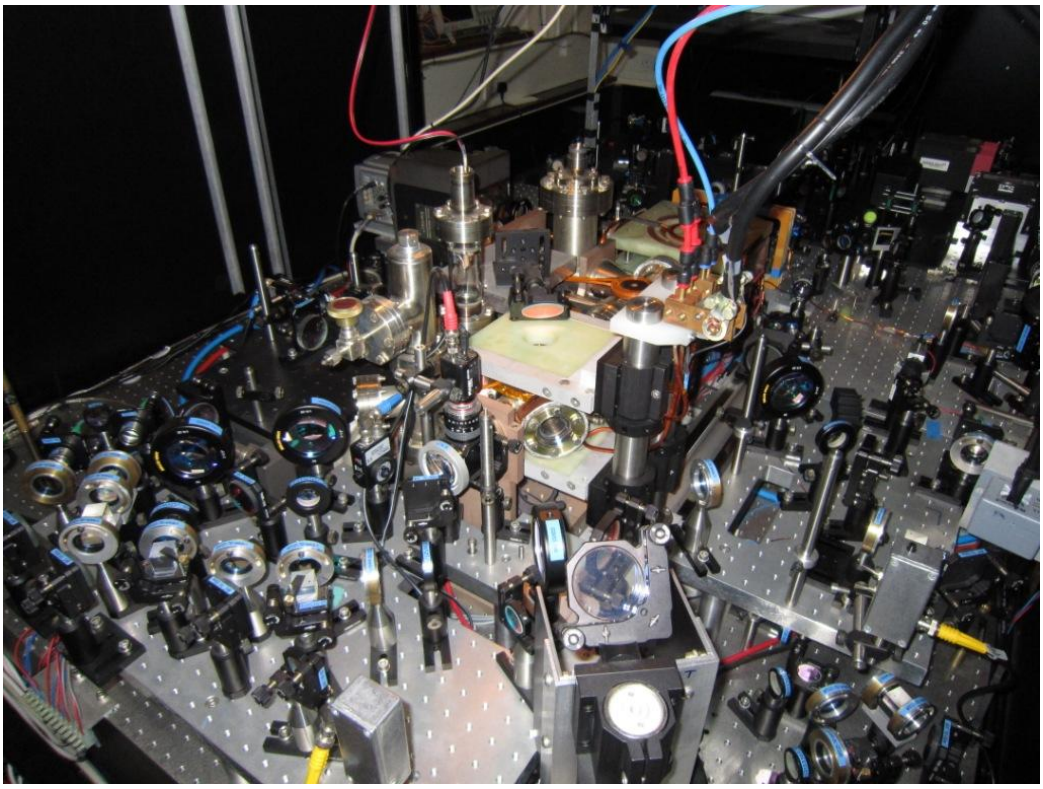

Figure 3.2: MOT optics: Vacuum chamber with MOT optics. The transport coil mount, along with the water and power connectors, can be seen towards the centre of the image.

that may arise as a result of the magnetic transport system (see section 3.2.3) constructed around the vacuum chamber, visible in Fig. 3.2. It also reduces the possibility of stray resonant light being scattered close to the glass cell which would otherwise limit the lifetime of the trapped atoms.

3.2.2 Laser cooling

Generation of laser cooling light

Light for laser cooling is derived from two Toptica DL100 (150 mW) extended cavity diode lasers. In addition, a Toptica BoosTA tapered amplifier is used to increase the power (of the cooling light) available for use in the MOT beams. This allows us to increase the size of the MOT beams (to a $1/e^2$ diameter of 30 mm), and hence the capture volume, whilst still maintaining a reasonable beam intensity.

The frequency of the cooling laser is stabilised using modulation transfer spectroscopy [80]. Locked -230 MHz from the D_2 $5^2S_{1/2}$ $F = 3 \rightarrow 5^2P_{3/2}$ $F' = 4$ transition in ^{85}Rb, the laser frequency is stable to better than 100 kHz. This detuning allows maximum flexibility in the frequencies we can then obtain using acousto-optic modulators (AOMs) (in both single and double pass configuration) to shift the frequency of the light. To repump atoms from the $F = 2$ ground state we stabilise the repump laser to drive transitions from $5^2S_{1/2}$ $F = 2 \rightarrow 5^2P_{3/2}$ $F' = 3$. However, the potential for atoms in the $5^2P_{3/2}$ $F' = 3$ excited state to decay back to both $F = 3$ and $F = 2$ means the repump laser must be locked with an alternative method. This time frequency modulation spectroscopy [81] is chosen, again providing stability on the order of 100 kHz with the laser locked -230 MHz from resonance.

For the work in chapters 4 and 5 involving ^{87}Rb the relevant transitions are the D_2 $5^2S_{1/2}$ $F = 2 \rightarrow 5^2P_{3/2}$ $F' = 3$ for the cycling (cooling) transition and $5^2S_{1/2}$ $F = 1 \rightarrow 5^2P_{3/2}$ $F' = 2$ for the repump light. Again, modulation transfer and frequency modulation spectroscopy are used to stabilise the laser frequencies.

To control the frequency and intensity of the cooling and repump light AOMs are used throughout the optical setup providing fast switching times and precise control of the laser cooling light. In addition, high speed shutters block any stray light from reaching the optical fibres used to deliver light to the experimental setup on the vacuum table.

Cooling in the MOT chamber

The very first step on the road to BEC begins with the trapping of atoms, from a background vapour, in a magneto-optical trap (MOT). Here we will not discuss the details of laser cooling but refer the reader to textbooks such as Refs.[61] and [82]. The MOT uses a standard six beam configuration, shown in Fig. 3.3, allowing up to 1×10^9 atoms to be collected in a $\sim 20-30$ s. Once sufficient atoms have accumulated in the trap, a 20 ms compressed MOT stage (CMOT) is carried out. This CMOT stage is achieved by reducing the intensity repump light whilst simultaneously increasing the detuning of the cooling light from -15 MHz to -35 MHz and relaxing the

quadrupole gradient (from 10 Gcm^{-1} to 5 Gcm^{-1}). This allows atoms to fall into the dark $F = 2$ state, decreasing the photon scattering rate and thus reducing heating effects to create a denser atomic sample.

Next we apply a 15 ms optical molasses phase. Here the quadrupole gradient is removed entirely leaving the atoms experiencing only the frictional force as a result of the scattering force of the MOT beams. The detuning of the cooling light is increased again, this time to 90 MHz. Following the molasses we optically pump the atoms, using a 2 ms pulse, to the low field seeking $F = 2, m_F = -2$ state in preparation for magnetic trapping and transport.

3.2.3 Magnetic transport

Central to the experimental setup is a magnetic transport apparatus. The ability to transfer atoms away from the high pressure MOT chamber to a much 'emptier' ultra high vacuum glass cell is key to the production of Bose-Einstein condensates. A full discussion of the transport procedure and hardware, along with details of its optimisation can be found in Ref. [44]. Here we only briefly discuss the key points associated with the final implementation.

Experimental implementation

Magnetic transport of cold atoms can be carried out in one of two ways. The first involves the sequential loading of multiple magnetic traps, each one slightly overlapped with the last [83]. In this way, the atoms, along with the magnetic potential can be translated over large distances. However the physical implementation requires the winding of many coil pairs and careful control of the currents flowing in each. An alternative scheme is to physically displace the trap itself rather than merely the potential by means of a motorized translation stage [84]. It is this latter approach that we adopt in our transport scheme. The magnetic potential used to create the 'transport' trap is formed from a pair of coils connected in an anti-Helmholtz configuration, producing a quadrupole potential.

To realise the motion of the trap the transport coils are mounted on a motorized translation stage (Parker XR404). The motion of the trap is then

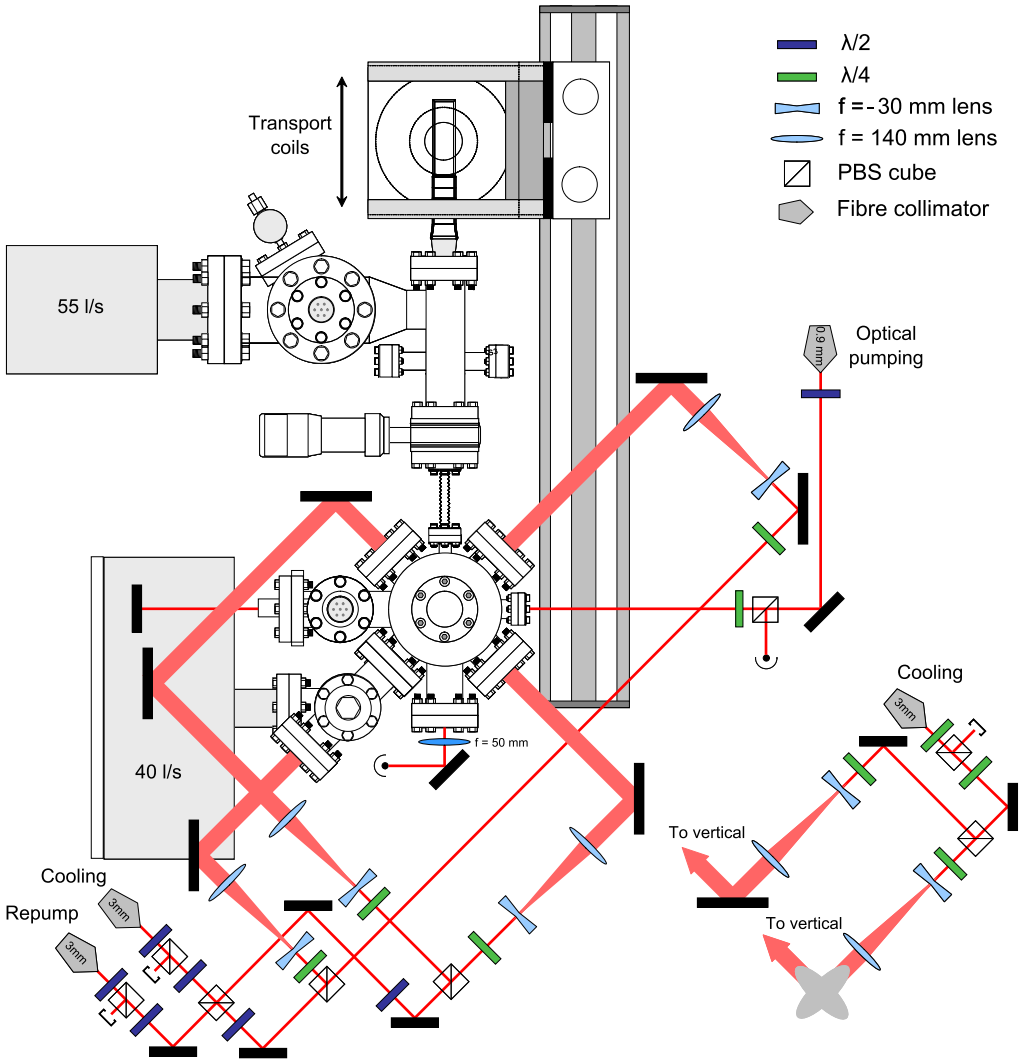

Figure 3.3: Vacuum chamber and MOT setup: Optical fibres deliver cooling and repump light from the laser table to the experimental table (shown). Light from one cooling fibre is split into four and expanded using telescopes to form the horizontal MOT beams. Light from a second cooling fibre is split into two paths and expanded to produce light for the vertical direction where a periscope (grey ellipses) is used to direct the light into the chamber. Repump light is only added into the horizontal beams. Also shown is the optical pumping beam used to transfer atoms into the $F = 2, m_F = -2$ ($F = 1, m_F = -1$) state in ^{85}Rb (^{87}Rb).

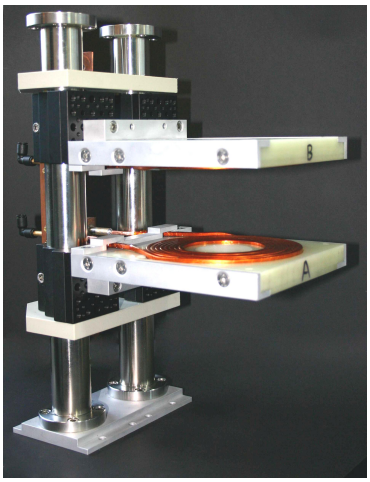

Figure 3.4: Magnetic transport apparatus: Atoms can be transfered between the MOT chamber and glass science via a magnetic transport apparatus. A quadrupole trap, mounted on a motorized translation stage physically moves the trapping potential along the length of the vacuum system before transferring the atoms contained within to a second, static trap.

programmed using commercial software, allowing full control of the transport profile, i.e. the acceleration, deceleration and velocity, and the position of the stage along its mounting rails. Dependent on the deceleration of the stage, its final position can be controlled to $\pm 10 - 50$ μm.

For atoms to remain in the trap during the transport process we require that the translational acceleration of the trap itself does not exceed the acceleration experienced by atoms due to the magnetic potential. We can approximate a value for this trapping acceleration by calculating the force on an atom due to the horizontal quadrupole gradient,

$$F = ma = m_F g_F \mu_B \frac{dB}{d\rho}. \tag{3.1}$$

For an atom in the $F = 2, m_F = -2$ state of ^{85}Rb , transported in a 180 Gcm^{-1} trap (90 Gcm^{-1} horizontally), this is equivalent to $\sim$40 ms^{-2}. Of course, the acceleration of the trap on its translation stage falls far short of this figure.

Loading and transporting

To load the trap the quadrupole gradient of the transport coils is switched on abruptly to 45 Gcm^{-1}. This is then ramped in 500 ms to the full transportation gradient of 180 Gcm^{-1}. The lifetime of atoms in the magnetic trap whilst still in the MOT chamber is severely limited (to around 10 s) due to collisions with background gas atoms. It is therefore advantageous to transport out of this region reasonably quickly. The rails accelerate initially at 1 ms^{-2} to reach their maximum velocity, 0.26 ms^{-1}. This velocity is maintained for the remaining duration of the transport before a deceleration stage, again at 1 ms^{-2}, brings the trap to rest at the location of a second, static quadrupole trap (the quadrupole trap referred to in all subsequent discussions), constructed around the glass science cell. The transport process takes around 2 s in total, physically moving the atoms a distance of 51 cm.

Once here the atoms must be transfered between the two traps. We do this by ramping the coil currents simultaneously, the transport current to zero and the quadrupole current to produce a gradient of 180 Gcm^{-1}, over an interval of 500 ms. The transport coils can then be moved away from the science cell and back to the MOT chamber, restoring important optical access.

Transport over an obstacle

A key advantage of using a quadrupole potential to produce the magnetic trap is the ease with which the field zero, and hence the trap centre, can be manipulated in space. By applying a bias field we are able to displace the trap vertically hence allowing atoms to be transported over an obstacle in the path of the moving trap.

The motivation for the inclusion of an obstacle is two-fold. Firstly this blocks the line of sight along the transport axis between the MOT chamber and the UHV glass science cell as can been seen in Fig. 3.1(c). As a result stray rubidium atoms meandering through the vacuum system are prohibited from reaching the super polished glass surface positioned in the cell, Fig. 3.1(b). The second reason relates more specifically to the choice of obstacle. By placing a right angled glass prism part-way along the transport axis and in

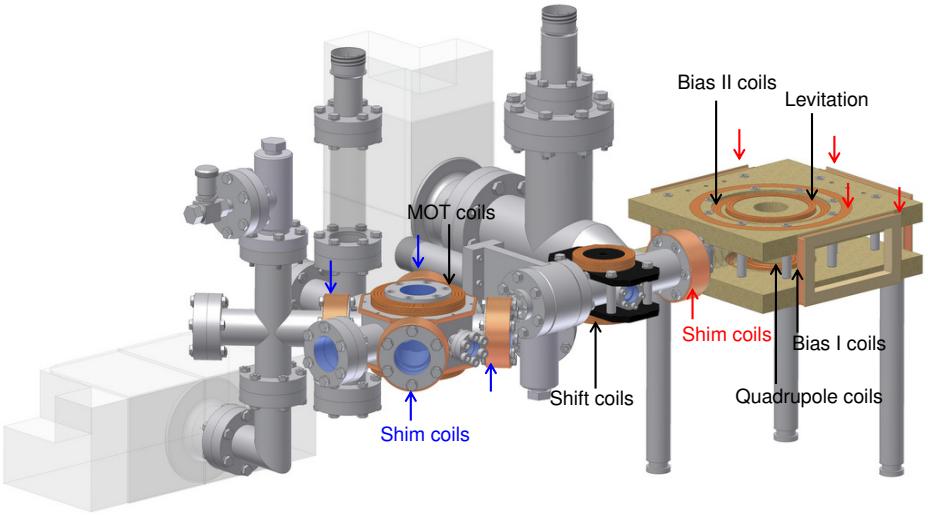

Figure 3.5: Magnetic coils in the experimental setup: The magnetic trapping and bias coils are constructed from Kapton-insulated square cross-section hollow copper tubing to allow water cooling. Shim coils are wound from 1 mm insulated copper wire. Figure from Ref. [43].

line with a view-port it is possible to safely couple high power laser beams (used for dipole trapping) out of the vacuum system. As we shall see in chapters 4 and 7, it is necessary to deliver beams into the science cell through the back surface of the super-polished Dove prism. As a consequence the beams would otherwise be directed into the MOT chamber and onto our fluorescence detector. Instead, total internal reflection of the beam incident on the right angled prism means the direction of propagation is modified such that the light can be safely blocked outside of the vacuum system.

A pair of 'shift' coils positioned around the obstacle produce a bias field of 216 G, enough to displace the cloud 1.2 cm vertically as the atoms are transported over. The position of these coils, along with the others in the experiment, is shown in Fig. 3.5 (figure from [43]). Importantly the shift field and its effect on the transport trap, particularly along the transport axis, is an important consideration in finding an optimum transport velocity. A full analysis of this interplay between the magnetic gradient and bias field can be found in [43].

3.3 Preparation of an ultracold atomic sample

With a cold cloud of atoms trapped at the science cell end of the apparatus we can begin the process of evaporative cooling to increase the phase space density of the sample. Initially this is carried out in the magnetic trap by inducing RF transitions to untrapped magnetic sublevels to forcibly remove the hottest atoms. Once the temperature becomes sufficiently low that losses from Majorana spin flips become appreciable, we switch on an optical trapping beam and reduce the magnetic confinement thus producing a *hybrid* trap. From here we continue to evaporatively cool the atoms by reducing the laser intensity until we reach degeneracy.

3.3.1 Evaporative cooling I: RF evaporation in a magnetic trap

Evaporative cooling is based on a simple principle; selectively removing the hottest atoms from a trapped gas and allowing the cloud to rethermalise through 'good' elastic collisions causes the overall temperature of the sample to decrease. Repeatedly removing the high energy tail of the velocity distribution results in a colder, denser atomic sample, albeit containing fewer atoms. In this way the phase space density can be increased by many orders of magnitude. (For a thorough review of evaporative cooling, see [85] and references therein.)

Although in the idealised case evaporation should be carried out infinitely slowly, removing as few atoms as possible at each stage, in reality the effect of 'bad collisions' with background atoms and inelastic loss mechanisms (see section 6.3.3) means that lifetime effects become an important consideration. The ultimate goal for any evaporator is the attainment of 'runaway evaporation' [86, 87]. Here as the sample cools, the rate of elastic collisions increases causing the process to accelerate.

In a magnetic trap, atoms can be removed using a radio-frequency (RF) driving field to selectively address the hottest atoms. These high energy

(high velocity) atoms sample a larger area of the magnetic trap, hence by applying an RF frequency resonant with only the highest Zeeman energy levels these hot atoms can be removed. The RF 'knife' flips the spins of the atoms such that they eventually couple into untrapped states at which point they are simply lost from the trap. The energy required for each spin flip is given by

$$E_{\text{cut}} = h\nu = \Delta m_F g_F \mu_B B, \tag{3.2}$$

where ν is the frequency of the applied RF and $\Delta m_F = 1$.

Evaporation in magnetic traps in this way has the key advantage that the trapping strength remains unaltered during the process. This generally means that elastic collision rates remain high. The evaporation can be controlled by altering the cut depth of the knife by varying the truncation parameter, η, which determines how far into the velocity distribution atoms are removed.

In order to produce the most efficient evaporation scheme it is useful to know at what frequency the RF knife begins to cut atoms away from the cloud. This frequency can be determined by applying the knife for some time (typically we use 5 s) at a fixed frequency and measuring the number of atoms remaining. Figure 3.6(a) shows the results of such an experiment. Although it can be difficult to determine a precise value for the exact frequency where the cutting occurs this measurement is sufficient to determine a suitable starting point for the evaporation ramps. Using the cut point it is possible to determine η by comparison with the cloud temperature prior to the application of the RF.

Measuring the cloud temperature

Information about the trapped atomic cloud is obtained from absorption images (see section 3.5.2). By measuring the cloud width σ after multiple times of flight τ (Fig. 3.6(b)) one can extract the temperature (T_{fit}) in both the horizontal and vertical directions by fitting a line of the form

$$\sigma^2(\tau) = \sigma_0^2 + \left(\frac{k_{\text{B}} T_{\text{fit}}}{m}\right)\tau^2. \tag{3.3}$$

The typical treatment of cloud expansion described in section 3.5.2 and in [88] assumes a Gaussian profile of the atomic density, however, this is not the case in the quadrupole trap. Fortunately, when released from the trapping potential, the cloud begins to expand with an isotropic Gaussian velocity distribution which, with sufficient time of flight, eventually overwhelms the initial density distribution. This occurs after a shorter expansion time in the vertical direction due to the smaller initial cloud size (as a result of the tighter confinement in this direction), hence we typically use the vertical cloud size (σ_x) to determine the cloud temperature. This is of particular importance for the quadrupole trap as it gives a more reliable result, as discussed in [89].

In the limit of a long time of flight an approximation to this temperature can be made by neglecting the initial cloud width. This allows the temperature to be obtained from a single image. Experimentally, we find $\tau \geq 18$ ms is sufficient to obtain a reasonable estimate.

Determining η

By comparing the energy of the atom in the trap,

$$E_{\text{atom}} = m_F g_F \mu_B B = k_{\text{B}} T, \tag{3.4}$$

with the energy of the cut we can determine the cutting temperature,

$$T_{\text{cut}} = \frac{m_F h\nu}{k_{\text{B}}}. \tag{3.5}$$

η is then the ratio of this temperature and that calculated from the expansion data,

$$\eta = \frac{T_{\text{cut}}}{T_{\text{fit}}}. \tag{3.6}$$

In our quadrupole trap $\eta \approx 8$. After 3 stages of RF evaporation we are typically left with 3×10^7 atoms at $T = 42$ μK and a PSD$= 5 \times 10^{-5}$ for ^{85}Rb and 2.7×10^7 atoms at $T = 32$ μK and a PSD$= 7 \times 10^{-5}$ for ^{87}Rb.

Majorana spin flips

Although further evaporation could be carried out in the quadrupole trap, the effect of Majorana spin [90] flips begins to limit the lifetime of the trapped

gas. Loss due to spin flips can be problematic in quadrupole traps, however this only become significant as the temperature of the cloud decreases and atoms spend more time close to the magnetic field zero. As shown in Ref. [91], the Majorana loss rate is given by

$$\Gamma_{\mathrm{M}} = 1.85\frac{\hbar}{m}\left(\frac{\mu B'}{k_{\mathrm{B}}T}\right)^2, \tag{3.7}$$

where $B' = dB/dx$ is the magnetic quadrupole gradient. Fortunately, during the transport stage the relatively high temperature of the atoms, ~ 300 μK, means this is not a significant consideration as the lifetime in a 180 Gcm^{-1} trap of atoms in the ^{85}Rb $F = 2, m_F = -2$ state is of order 100 s considering Majorana losses alone. However, for a 40 μK cloud, this reduces to around 2 s hence at this point it is better to instead transfer atoms into an optical dipole trap.

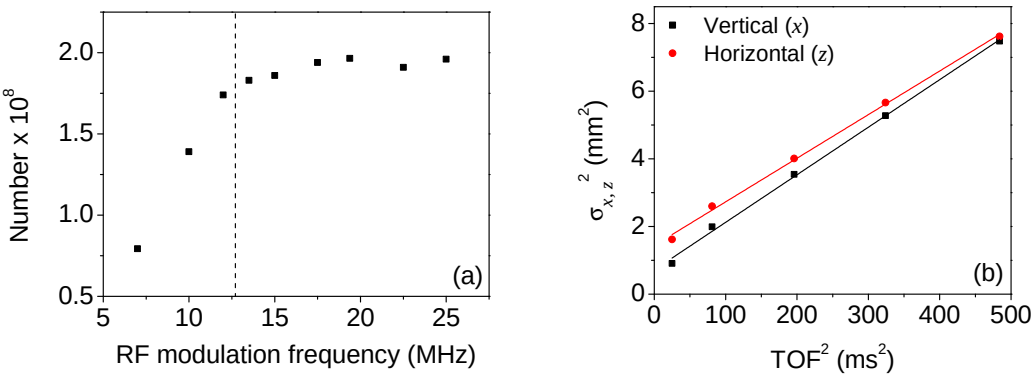

Figure 3.6: RF evaporation in the quadrupole trap: (a) The edge of the cloud can be found by the application of the RF knife at a fixed frequency and measuring the number of atoms remaining after some time. The dotted line gives a rough value of the frequency at which the knife starts to take effect. (b) Cloud width as a function of time of flight (TOF) expansion. Fitting Eq. (3.3) gives temperatures of $T_{\mathrm{v}} = 148(4)$ μK and $T_{\mathrm{h}} = 136(3)$ μK.

3.3.2 Optical trapping

A comprehensive review of optical trapping can be found in Ref.[92]. Here we will discuss only the basic theory of dipole trapping and the origin of the

dipole force as a background to the technique central to the apparatus.

The fundamental principle of an optical dipole trap relies on the interaction between an electric dipole and far detuned light. As a result of this detuning, optical excitations are minimal in this class of trap and light-induced loss mechanisms low, however, depths are limited to typically < 1 mK. In these traps the size of the radiation force from photon scattering is overwhelmed by the dominant dipole force. We begin by considering an atom as a mechanical oscillator, subject to a classical radiation field in order to first derive the equations governing the dipole interaction.

A simplified model

An induced electric dipole moment can be created by subjecting an atom to laser light. The electric field of this light, $\mathbf{E}$, induces a dipole moment $\mathbf{p}$ in the atom, oscillating at the driving frequency ω. As is convention, $\mathbf{E}$ and $\mathbf{p}$ are defined as,

$$\mathbf{E}(\mathbf{r},t) = \hat{\mathbf{e}}\tilde{E}(\mathbf{r})\exp(-i\omega t) + c.c., \tag{3.8}$$

$$\mathbf{p}(\mathbf{r},t) = \hat{\mathbf{e}}\tilde{p}(\mathbf{r})\exp(-i\omega t) + c.c., \tag{3.9}$$

where $\hat{\mathbf{e}}$ is the unit polarization vector. The amplitude of the dipole moment, $\tilde{p}$, is related to the the amplitude of the field, $\tilde{E}$, via the complex polarizability of the atom, α, itself dependent on the driving frequency, such that

$$\tilde{p} = \alpha\tilde{E}. \tag{3.10}$$

The interaction potential of the induced dipole moment in the driving field is then given by

$$U_{\text{dip}} = -\frac{1}{2}\langle\mathbf{pE}\rangle = -\frac{1}{2\epsilon_0 c}\text{Re}(\alpha)I. \tag{3.11}$$

Angular brackets denote a time average over rapidly oscillating terms and the factor of $\frac{1}{2}$ accounts for the induced rather than permanent nature of the dipole moment. The intensity of the laser field is related to the field amplitude as

$$I = 2\epsilon_0 c|\tilde{E}|^2. \tag{3.12}$$

The dipole force can then be found by taking the gradient of this potential

$$\mathbf{F}_{\text{dip}}(\mathbf{r}) = -\nabla U_{\text{dip}}(\mathbf{r}) = -\frac{1}{2\epsilon_0 c}\text{Re}(\alpha)\nabla I(\mathbf{r}). \tag{3.13}$$

This is a conservative force, proportional to the position dependent field intensity.

A second important quantity is the scattering rate. Whereas the real part of the polarizability, responsible for the dispersive properties of the interaction, gives rise to the dipole force, the imaginary part partially describes the power absorbed by the oscillator,

$$P_{\text{abs}} = \langle \dot{\mathbf{p}}\mathbf{E} \rangle = 2\omega \text{Im}(\tilde{\text{p}}\tilde{\text{E}}^*) = \frac{\omega}{\epsilon_0 \text{c}} \text{Im}(\alpha) I. \tag{3.14}$$

If one considers the laser light to be a stream of photons with energy $\hbar\omega$ the absorption can be thought of as a series of absorption and spontaneous re-emission processes amounting to scattering with a rate

$$\Gamma_{\text{sc}}(\mathbf{r}) = \frac{P_{\text{abs}}}{\hbar\omega} = \frac{1}{\hbar\epsilon_0 c} \text{Im}(\alpha) I(\mathbf{r}). \tag{3.15}$$

Atomic polarizability

Keeping with a classical picture of simple oscillators, the atomic polarizability can be derived from a model of an electron, elastically bound to a core [92]. The polarizability is then given by,

$$\alpha = \frac{e^2}{m_e} \frac{1}{\omega_0^2 - \omega^2 - i\omega\Gamma_\omega}, \tag{3.16}$$

where

$$\Gamma_\omega = \frac{e^2\omega^2}{6\pi\epsilon_0 m_e c^3}, \tag{3.17}$$

is the damping rate due to radiative energy loss. Defining an on-resonance damping term $\Gamma \equiv \Gamma_{\omega_0} = (\omega_0/\omega)^2\Gamma_\omega$, Eq. (3.16) then becomes

$$\alpha = 6\pi\epsilon_0 c^3 \frac{\Gamma/\omega_0^2}{\omega_0^2 - \omega^2 - i(\omega^3/\omega_0^2)\Gamma}. \tag{3.18}$$

For reference, frequency-dependent polarizabilities for the alkalis can be found in Ref. [93].

In the case of dipole trapping the far-detuned nature of the light means saturation effects are of little consequence. As a result, this classical model returns an almost identical result to the semi-classical approach, considering an atom as a two-level system interacting with a classical radiation field, with only a slight modification to the calculation of the damping rate, Γ, to differentiate between the two.

The dipole potential

In this limit of large detuning and negligible saturation we have,

$$U_{\mathrm{dip}}(\mathbf{r}) = -\frac{3\pi c^2}{2\omega_0^3}\left(\frac{\Gamma}{\omega_0-\omega}+\frac{\Gamma}{\omega_0+\omega}\right) I(\mathbf{r}), \tag{3.19}$$

$$\Gamma_{\mathrm{sc}}(\mathbf{r}) = \frac{3\pi c^2}{2\hbar\omega_0^3}\left(\frac{\omega}{\omega_0}\right)^3\left(\frac{\Gamma}{\omega_0-\omega}+\frac{\Gamma}{\omega_0+\omega}\right)^2 I(\mathbf{r}). \tag{3.20}$$

It is generally the case that the trapping laser used is close enough to resonance such that the detuning $\Delta \equiv \omega - \omega_0$ fulfills $|\Delta| \ll \omega_0$. As a consequence, the counter-rotating term (resonant at $\omega = -\omega_0$) can be neglected in the rotating wave approximation and it is reasonable to set $\omega/\omega_0 \approx 1$. We then arrive at the somewhat simplified yet familiar results

$$U_{\mathrm{dip}}(\mathbf{r}) = \frac{3\pi c^2}{2\omega_0^3}\frac{\Gamma}{\Delta} I(\mathbf{r}), \tag{3.21}$$

$$\Gamma_{\mathrm{sc}}(\mathbf{r}) = \frac{3\pi c^2}{2\hbar\omega_0^3}\left(\frac{\Gamma}{\Delta}\right)^2 I(\mathbf{r}). \tag{3.22}$$

Importantly the scaling of these two quantities, in terms of intensity and detuning, gives clear indications about how to best achieve an effective dipole trap experimentally. Equating Eqs. (3.21) and (3.22) we find the two quantities are related as,

$$\hbar\Gamma_{\mathrm{sc}} = \frac{\Gamma}{\Delta} U_{\mathrm{dip}}. \tag{3.23}$$

In the ideal case intensities should be high to obtain large trap depth. However, for a given trap depth we see that it is advantageous to increase the laser detuning to reduce the scattering rate of the trapped atoms.

The sign of the laser detuning also has a crucial impact on the resulting dipole potential. For a red detuned beam, $\Delta < 0$, the resulting dipole potential is negative hence atoms are attracted into regions of high intensity. In contrast, when the light field is above resonance, or blue detuned, $\Delta > 0$, atoms are repelled from the field. In this case the minimum of the potential corresponds to the minimum of the beam intensity.

Gaussian beams

Knowing the beam intensity is of paramount importance in understanding the dipole potential. Fortunately, most laser beam profiles can be approximated

by Gaussian functions thus obeying Gaussian optics. A Gaussian laser beam propagating along the z-direction can be described by

$$U = U_0 e^{i(kz-\omega t)} \frac{e^{ikr^2/2q}}{q}, \tag{3.24}$$

where $r^2 = x^2 + y^2$, $q = z - z_{\text{waist}} - iz_{\text{R}}$, U is the electric field amplitude, z_{waist} is the position of the beam waist and z_{R} the Rayleigh range. As it propagates, the beam width, or $1/e^2$ radius, evolves as

$$w_i(z) = w_{0i}\sqrt{1 + (z/z_{\text{R}})^2}, \tag{3.25}$$

with the Rayleigh range given by

$$z_{\text{R}} = \frac{\pi w_0^2}{\lambda}, \tag{3.26}$$

where w_0 is the beam waist and λ the wavelength of the light. Over this distance, z_{R}, the width of the beam increases to $\sqrt{2}w_0$.

Again considering propagation in z, the beam intensity can be expressed as,

$$I(x, y) = I_0 e^{-2x^2/w_x^2} e^{-2y^2/w_y^2}, \tag{3.27}$$

allowing for different waists in x and y, with the peak intensity I_0 given by

$$I_0 = \frac{2P_0}{\pi w_x(z) w_y(z)}. \tag{3.28}$$

Optical trapping lasers

Two high power lasers have been used to create optical dipole traps used in this work. In the experiments described in chapter 4 a multimode ELS Versadisk laser capable of producing 50 W of power at $\lambda = 1030$ nm was used to produce the single beam dipole trap. Unfortunately, this disk laser was subject to severe fluctuations in both the beam profile and power hence the only workable solution was to fibre couple the light used for dipole trapping. High power, shielded fibres (shown in Fig. 3.7) fixed the beam size and allowed intensity fluctuations to be servo controlled however, this limited the power delivered to the trap to only 2.5 W. Subsequently this disk laser was replaced by a single frequency IPG fibre laser (IPG: YLR-15-1064-LP-SF) producing 15 W at $\lambda = 1064$ nm.

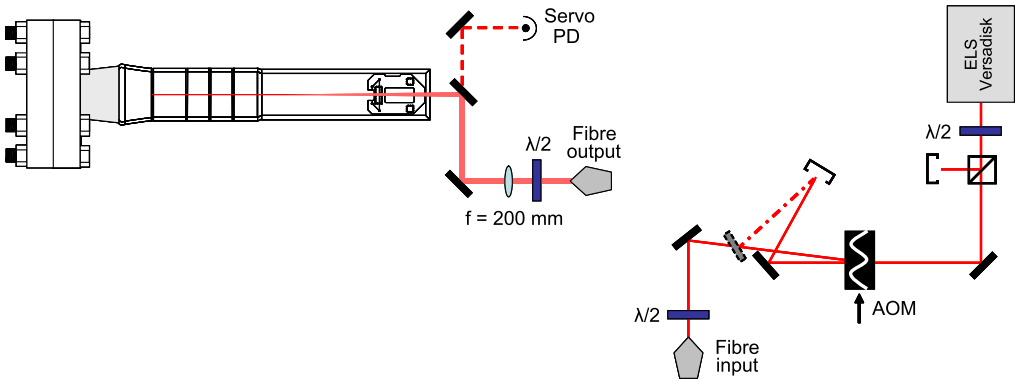

Figure 3.7: Single beam optical dipole trap layout: Light from an ELS Versadisk laser is coupled into a high power optical fibre. The light is then delivered close to the glass science cell where it is focussed to produce a 57 μm waist, $\sim$3.5 mm in front of the super polished Dove prism. Intensity control of the beam is provided by a servo controlled AOM.

As with the laser cooling light, the intensity of the dipole beams is controlled using an AOM. For the ELS laser we use a NEOS 23080-2-1.06 and for the IPG an Isomet M1080-T80L. Intensity fluctuations are corrected for via a servo feedback loop using a monitor photodiode.

Although not producing a trap in the strictest sense, the waveguide beam used in chapter 7 can be considered as an additional dipole trapping beam. The light for this beam is derived from a 2 W Innolight laser, operating at 1064 nm.

Optical trap layout

Figure 3.7 shows the optical layout of the single beam dipole trap used to carry out the work described in chapter 4. Light from the Versadisk laser passes through an AOM before it is coupled into a high power optical fibre. The output of the fibre is positioned close to the glass cell. An adjustable collimator on the output (and input) means the beam size of the light out of the fibre can be adjusted easily.

To produce a narrow beam waist to form the dipole trap a $f = 200$ mm lens focusses the light to 57 μm approximately 3.5 mm from the front face

of the super-polished prism. The small amount of light which leaks through the final delivery mirror is focussed onto a photodiode used in the servo loop control of the AOM. A half-waveplate is also used in the beam path to change the polarisation of the dipole trapping light to controlling the amount of light transmitted through the final delivery mirror and to the servo photodiode.

3.3.3 A hybrid magnetic and optical trap

Throughout this work a *hybrid* trap produced from both magnetic and optical confinement is used to trap and manipulate a sample of ultracold atoms. In chapter 4 we employ the simplest case, a single dipole laser beam positioned a small distance below the field zero of a magnetic quadrupole trap as shown in Fig. 3.8(a). In this system tight radial confinement is provided by the dipole laser beam and weaker axial confinement along the beam arises as a result of the magnetic trap. The full potential is given by [91],

$$U(r) = \mu B' \sqrt{x^2 + \frac{y^2}{4} + \frac{z^2}{4}} - U_0 \exp\left(-2[y^2 + (x - x_{\text{offset}})^2]/w_0^2\right) + mgx + E_0. \tag{3.29}$$

Here μ is the magnetic moment of the atoms and B' the quadrupole gradient in the x direction (along the axis of the coils). The dipole laser is described by its trap depth, U_0, waist, w_0 and offset, x_{offset}, from the quadrupole field zero which is positioned at $x = y = z = 0$. E_0 accounts for the small difference in the trap minimum when the dipole trap is present and is such that $U(r_{\min}) = 0$. Finally m and g are the mass of the atom and the acceleration due to gravity. We assume a geometry whereby the beam propagates along z-direction and is displaced vertically in the x-direction. As the Rayleigh range of laser beams used is typically large compared to the offsets in the trap we neglect the effect of beam focussing.

Radial trap frequency

In the radial directions of the trap the oscillation frequency is dominated by the dipole laser beam. If we take the part of the potential associated with

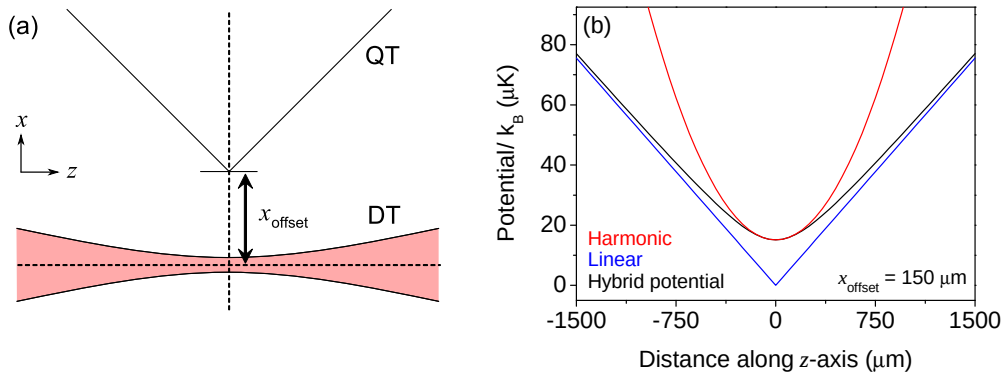

Figure 3.8: Single beam hybrid dipole trap axial potential: (a) Schematic of the experimental setup. The dipole trap (DT) beam is positioned a distance x_{offset} below the field zero of a magnetic quadrupole trap (QT). (b) Axial potential. For small displacements along the axis of the beam $z \ll x_{\text{offset}}$ the trapping potential remains harmonic. Beyond this the linear quadrupole potential begins to dominate.

the laser beam,

$$U_{\text{laser}} = -U_0 \exp\left(-2[y^2 + (x - x_{\text{offset}})^2]/w_0^2\right), \tag{3.30}$$

and set $x = x_{\text{offset}}$ (i.e. looking at the position of the beam), we have,

$$U_{\text{laser}} = -U_0 \exp\left(-2\frac{y^2}{w_0^2}\right) \simeq -U_0 + \frac{2U_0 y^2}{w_0^2}. \tag{3.31}$$

By comparison to the harmonic oscillator solution, $U = \frac{1}{2}m\omega^2 y^2$ we then arrive at

$$\omega_{\text{radial}} = 2\sqrt{\frac{U_0}{m w_0^2}}. \tag{3.32}$$

Axial trap frequency

In a single beam trap the laser beam contributes only very weakly to the trapping in the axial direction. If the thermal energy of the atoms, $k_{\text{B}}T$, is small compared to the trap depth the spatial extent of the atoms in the radial direction is small compared to the beam waist. The cloud is also small in the axial direction compared to the relevant length scale, z_{R} [92]. In this limit the trap potential can be approximated by a harmonic oscillator with

cylindrically symmetric geometry,

$$U_{\text{laser}} \simeq -U_0 \left[1 - 2 \left(\frac{r}{w_0} \right)^2 - \left(\frac{z}{z_{\text{R}}} \right)^2 \right], \tag{3.33}$$

where $r^2 = x^2 + y^2$. Setting $x = y = 0$ the oscillation frequency is given simply by

$$\omega_{\text{dip axial}} = \sqrt{\frac{2U_0}{m z_{\text{R}}}}. \tag{3.34}$$

This gives an axial trapping along the beam due to the laser light of <1 Hz. Instead, trapping in the axial direction is set by the magnetic potential. Considering the magnetic contribution to the total trapping potential,

$$U_{\text{mag}} = \mu B' \sqrt{x^2 + \frac{y^2}{4} + \frac{z^2}{4}} \tag{3.35}$$

it is possible to derive an expression for the trapping frequency. We begin by positioning ourselves at $y = 0$ and $x = x_{\text{offset}}$ thus simplifying the potential to

$$\begin{aligned} U_{\text{mag}} &= \mu B' \sqrt{\frac{z^2}{4} + x_{\text{offset}}^2} \\ &= \mu B' x_{\text{offset}} \sqrt{\frac{z^2}{4 x_{\text{offset}}^2} + 1}. \end{aligned} \tag{3.36}$$

Assuming that $|z^2/4x_{\text{offset}}^2| \leq 1$ we can then Taylor expand Eq. (3.36) to give

$$U_{\text{mag}} = \mu B' x_{\text{offset}} + \frac{\mu B' z^2}{8 x_{\text{offset}}}. \tag{3.37}$$

Again we compare the form of the potential to the harmonic oscillator solution and hence we obtain an expression for the axial trapping,

$$\omega_{\text{mag axial}} = \frac{1}{2} \sqrt{\frac{\mu B'}{m x_{\text{offset}}}}. \tag{3.38}$$

The validity of this expansion is obviously somewhat limited. The constraint of the Taylor expansion, $|z^2/4x_{\text{offset}}^2| \leq 1$, or equivalently that $z \ll x_{\text{offset}}$, means that this harmonic description of the trapping only remains true for axial displacements much less than the offset between the field zero and the laser beam position. Beyond this the linear nature of the quadrupole trap begins to dominate, $U \approx \mu B' z/2$, and this simple model breaks down as shown in Fig. 3.8(b).

If the trap is perfectly levitated, $B' = mg/m_F g_F \mu_B$, Eq. (3.38) reduces to

$$\omega_{\text{mag axial}} = \frac{1}{2}\sqrt{\frac{g}{x_{\text{offset}}}}. \tag{3.39}$$

Typically, the beam is displaced by $x_{\text{offset}} \simeq 150$ μm resulting in an axial frequency of $\sim$20 Hz.

Effect of additional bias fields

The fact that the axial trapping in the hybrid setup is determined by the position of the laser beam relative to the field zero presents an immediate problem should one wish to apply a magnetic bias field in vertical direction (along x). The addition of the bias field produces a shift in the position of magnetic field zero proportional to both the field, B_0 and the gradient,

$$x_{\text{shift}} = \frac{B_0}{B'}. \tag{3.40}$$

Substituting this into Eq. (3.38) we recover an expression for the trap frequency more familiar in the context of the Ioffe-Pritchard trap [32],

$$\omega_{\text{mag axial}} = \frac{1}{2}\sqrt{\frac{\mu B'^2}{mB_0}}. \tag{3.41}$$

As an example, to access the 155 G Feshbach resonance in ^{85}Rb using a 22 Gcm^{-1} gradient to close off the trap would shift the field zero by $\sim$7 cm. Neglecting the initial beam displacement, this reduces the axial trapping to $\sim$0.9 Hz. As such the beam acts less like a trap and more like a waveguide.

To circumvent this problem in chapters 5 and 6 this hybrid trap is extended to a crossed trap geometry. In this case the trap frequency is no longer set by the magnetic confinement, however the levitation provided by the gradient is still important in maximising the trap depth and providing a weak confinement along the arms of the laser beams. The hybrid trap therefore has a larger volume than a pure crossed dipole trap without a magnetic gradient. This can be advantageous when initially loading the dipole trap following the RF evaporation in the quadrupole trap.

3.3.4 Evaporative cooling II: Evaporation in an optical trap

Evaporative cooling in an optical trap is mostly commonly carried out by reducing the intensity of the trapping beam(s). This has the effect of lowering the trap depth U_0, allowing the hottest atoms to escape. However, an unfortunate side effect of reducing the beam power is a corresponding reduction in the trap frequencies as shown in Fig. 3.9(a) and Eq. (3.32). This lowers the elastic collision rate, slowing down rethermalisation. Despite this, it is still possible to create Bose-Einstein condensates in optical traps using exactly this method. Alternatively, using a magnetic field gradient to effectively tilt the optical potential it is possible to maintain the trap frequencies whilst still allowing hot atoms to escape from the trap [87] as shown in Fig. 3.9(b) .

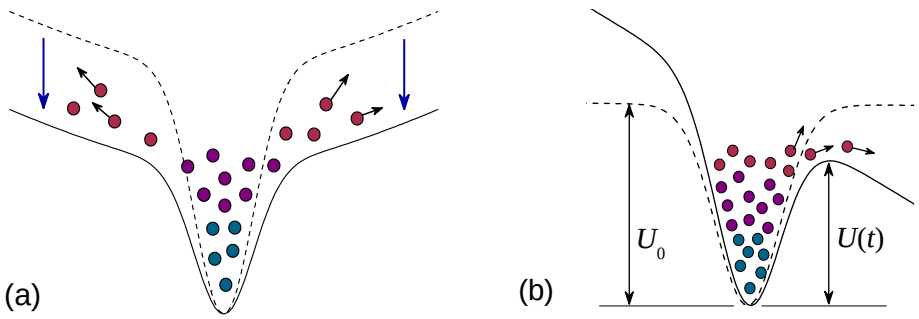

Figure 3.9: Evaporation in an optical dipole trap: (a) By lowering the beam intensity it is possible to reduce the trap depth, allowing the hottest atoms to leave the trap. In lowering the beam intensity, the trap frequencies are also reduced. (b) Alternatively, applying a magnetic field gradient to tilt the trap lowers the trap depth (from U_0 to some reduced value $U(t)$) but maintains the trapping frequencies.

3.4 Experimental control

During any experimental cycle a series of precisely timed operations must be carried out, controlling the laser light and magnetic fields seen by the atoms. This control is realised in the experiment using a National Instruments LabVIEW FPGA system. Field-programmable gate arrays (FPGAs) are reprogrammable silicon chips which physically rewire in order to carry out the user's desired operation. This has the advantage of faster response times yet has the same flexibility of software running on a processor-based system, but it is not limited by the number of processing cores available [94].

A combination of both analog and digital output channels provide complete control over the experimental hardware. Digital TTL signal are used to trigger the majority of operations, switching between levels on μs timescales. Although the board can be configured to give 25 ns resolution this is unnecessary for our current work. The analog channels provide linear ramping (with 2 μs resolution), and are used to control the magnetic coil currents along with the servo controlled high power AOMs used for optical trapping.

Alongside the FPGA control of the experiment a small number of devices are controlled using GPIB. These include the Agilent power supplies controlling the magnetic coil currents and the function generators used to produce signals for RF evaporation. The GPIB system is run independently from the FPGA software, instead communication is achieved through 'start' and 'finish' TTLs sent between the two control computers. This avoids disruption to the precise timing established with the FPGA system.

3.5 Diagnostics

We adopt two commonly used imaging diagnostic techniques to obtain information about our trapped atomic cloud. In the MOT chamber fluorescence from the atoms in the MOT beams is collected allowing a real time assessment of the MOT loading rate. Once we transfer to the science cell absorption imaging is used to measure both the optical depth and the cloud size after a short time of flight allowing the number and temperature of the cloud to be

calculated, along with a range of other properties.

3.5.1 Fluorescence detection

In the MOT chamber fluorescence from the atoms in the MOT is monitored using a photodiode (Thorlabs DET36M). This signal from this monitor can then be converted to an atom number according to [95][1]

$$N = \frac{V_{\text{sig}}}{R(\lambda)R_{\text{PD}}}\frac{16x^2}{d^2}\left(\frac{\hbar\omega_L\Gamma}{2}\frac{C_1^2 I/I_{\text{SAT}}}{1+C_2^2 I/I_{\text{SAT}}+4(\Delta/\Gamma)^2}\right)^{-1}. \tag{3.42}$$

The conversion factors necessary to obtain an atom number depend on properties of the atoms, properties of the MOT light and on experimental parameters. Here I_{SAT} is the saturation intensity, Δ the detuning of cooling light from the $F = 3$ to $F' = 4$ transition, Γ the linewidth of the cooling transition, V_{sig} the photodiode signal (including factors such as filter efficiency and losses due to a 50:50 beam splitting cube), x is the distance from the MOT to the lens collecting the fluorescence, d diameter of the limiting aperture, R_λ photodiode responsivity at 780 nm and R_{PD} (= 0.5 A/W) the load of the photodiode (=1 MΩ due to the oscilloscope used to monitor the signal).

This fluorescence detection can be used to optimise many parameters associated with the laser cooling stage of the experiment. Using recapture measurements, whereby the MOT light and coils are pulsed on again after some experimental sequence, it is possible to measure the fraction of atoms transfered from the MOT into the magnetic trap. However, after the transport process it is more practical to adopt absorption imaging as our diagnostic. This allows more information about the trapped atoms to be obtained, albeit at the cost of destroying the cloud.

[1]Here the coefficient C_1 and C_2 [96] account for the unknown distribution of m_F states present in the MOT. Using an $I_{\text{SAT}-\text{closed}}$ based on only closed transitions or an $I_{\text{SAT}-\text{isotropic}}$ assuming a random distribution of m_F states affects the atom numbers calculated by a factor of two. Using these coefficients gives an atom number which lies between these two conventions.

3.5.2 Absorption imaging

At the science cell end of the apparatus we use both horizontal and vertical absorption imaging to align and characterise the optical and magnetic traps. The optical setup used for the two directions is shown in Fig. 3.10. Absorption imaging allows properties of an atomic cloud to be calculated from the shadow cast by the atoms when subjected to a short pulse of resonant light. As the light passes through the cloud atoms absorb and scatter photons. By imaging the remaining light on a CCD camera it is then possible to extract the column density of the cloud along with its spatial profile by fitting a Gaussian lineshape to the shadow. We will not reproduce the full calculations used to determine the cloud parameters here, rather they can be found in [88].

In the very briefest of overviews we consider how the measured optical depth and cloud size leads to a number and temperature measurement. The optical depth OD, defined as

$$I = I_0 \exp(-\mathrm{OD}(x, z)), \tag{3.43}$$

gives a measure of the drop in intensity I of the probe beam (with initial intensity I_0) as it passes through the cloud. Along with the cloud widths σ_i (defined here as $1/e^2$ radii) the number of atoms in the cloud can be calculated from the peak optical depth at the cloud centre according to

$$N_{\mathrm{fit}} = \frac{2\pi \mathrm{OD}_{\mathrm{peak}} \sigma_{\mathrm{x}} \sigma_{\mathrm{z}}}{\sigma_0}, \tag{3.44}$$

where $\sigma_0 = 3\lambda^2/2\pi$ for a 2-level atom.

In free expansion the width of the cloud depends on the time of flight and the frequency of the trap from which the atoms were released. After a time τ the cloud width is given by

$$\sigma_{x,z}(\tau) = \sqrt{\sigma_{x,z}^2(0) + \omega_{x,z}^2 \tau^2 \sigma_{x,z}^2(0)} = \sigma_{x,z}(0)\sqrt{1 + \omega_{x,z}^2 \tau^2}. \tag{3.45}$$

Here $\sigma(0)$ is the width of the cloud in-trap. From the time of flight width we can then calculate the in-trap size and hence determine the temperature of the cloud,

$$T_{x,z} = \frac{m\omega_{x,z}^2 \sigma_{x,z}^2}{k_{\mathrm{B}}}. \tag{3.46}$$

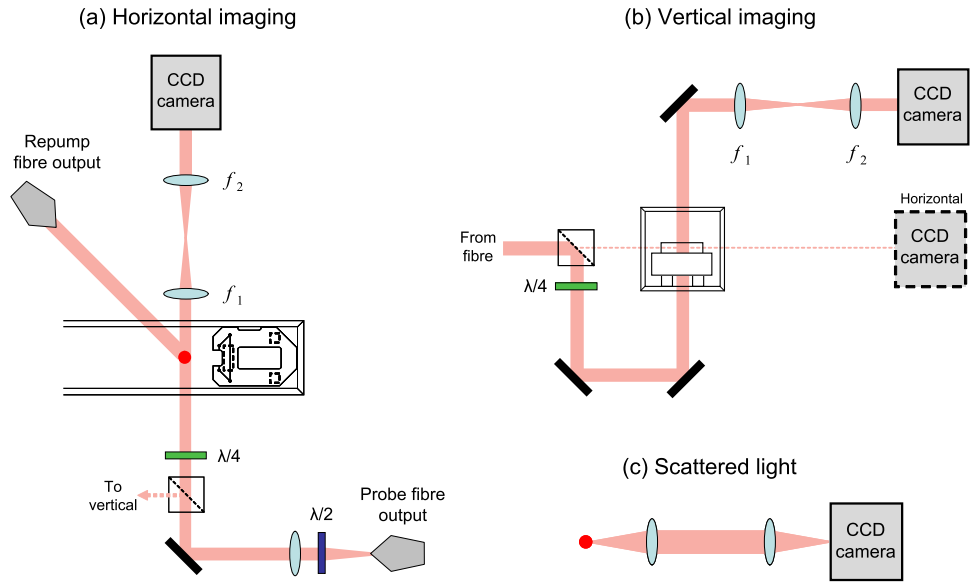

Figure 3.10: Absorption imaging optical layout: (a) Horizontal imaging layout. Atoms are illuminated with both probe and repump light in the horizontal plane. The probe light is then focussed down onto a CCD camera using a pair of lenses. The ratio f_2/f_1 gives the magnification of the imaging system. (b) Vertical imaging layout. The probe light used for the vertical imaging is split off using a PBS cube in the horizontal plane. The same repump light used for the horizontal imaging is used in the vertical setup. (c) Propagation through the optical setup of the light scattered by the atoms.

Levitated time of flight

Due to the high densities present in Bose-Einstein condensates it is often desirable to increase the time of flight before an absorption image is taken. This increased expansion time causes the optical depth to fall. However, the drop time is limited by the field of view of the camera as the atoms fall under gravity during the time of flight.

This problem can be circumvented using a *levitated* time of flight. Here a magnetic gradient remains on during the expansion, cancelling the effect of gravity and levitating the cloud. In addition, a bias field is applied to shift the magnetic field zero far away vertically so the atoms are not forced into the '$2g$' potential (twice the effect of gravity) created above the field zero. The cloud is then able to expand freely in the vertical direction, however, the effect of the magnetic gradient and bias field creates a weak harmonic trap in the horizontal direction (see Eq. (3.41)). As such, calculations of temperature from a levitated time of flight use only the vertical cloud width.

Imaging resolution

For a perfect system the diffraction limit, setting a bound on the resolution of the imaging, is given by

$$d = 1.22\lambda NA = 1.22\frac{f\lambda}{D}. \tag{3.47}$$

The smallest resolvable distance d is therefore determined by the wavelength λ of the light being used and the numerical aperture NA of the imaging lens (NA = focal length, f / diameter, D). In the current absorption imaging setup this gives a diffraction limited resolution of ~ 4 μm. If we also consider our typical magnification, $\times 1$ or $\times 1.5$, this results in an effective pixel size of 8 μm or 5.2 μm. Although these calculations ignore aberrations and assume full illumination of the imaging lens, they give an order of magnitude estimate of the best resolution we can expect to achieve.

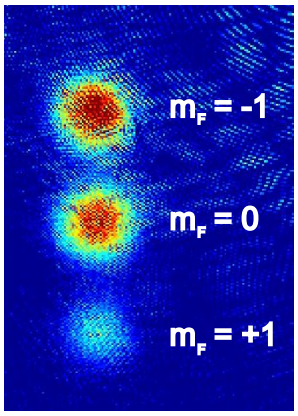

Figure 3.11: Multiple spin states of ^{87}Rb : Application of an RF field to atoms in a magnetic field drives $\Delta m_F = 1$ transitions between magnetic sublevels. In a levitated time of flight these spin states spatially separate. Driving transitions in this way can be used to precisely calibrate the magnetic field seen by the trapped atoms.

3.5.3 Magnetic field calibration

As we shall see in chapter 6 in order to tune the scattering properties of the atomic cloud we will employ a magnetic Feshbach resonance. This allows the scattering length to be varied as a function of the applied bias field, hence, to precisely know the scattering length of the atoms we must first precisely know the magnetic field seen by them.

To calibrate the magnetic field we use Stern Gerlach spectroscopy. The application of an oscillating RF field, perpendicular to the magnetic field, drives $\Delta m_F = 1$ transitions between the magnetic sub levels of the atoms. If the resonant frequency which causes these spin flips can be determined a bias field can be extracted using a Breit-Rabi diagram [97]. Typically a 10 ms pulse of fixed frequency RF is applied and the number of atoms remaining measured after a short hold time. This allows atoms flipped to untrapped states to fall away.

Alternatively, if this hold time is reduced and a levitated time of flight used (where the quadrupole trap and small bias field remain on during the time of flight to cancel the effect of gravity) it is possible to observe the occupation of multiple spin states caused by the spin flips. Figure 3.11 shows ^{87}Rb atoms

in the $F = 1$ state, originally trapped in $F = 1, m_F = -1$. In the time of flight the $m_F = -1$ atoms are levitated, the $m_F = 0$ atoms feel no magnetic levitation and fall under gravity and the $m_F = +1$ atoms are accelerated downwards, feeling the effect of gravity plus an additional magnetic force comparable to gravity (opposite to the levitation experience by the -1 atoms).

3.6 Summary

In this chapter we have introduced the experimental apparatus used to produce ultracold atomic gases, highlighting key features of the setup. In subsequent chapters we will explore the performance of the apparatus, in particular the optical dipole traps, working towards our goal of producing quantum degenerate gases of rubidium close to a room temperature dielectric surface.

Chapter 4

A single beam optical dipole trap: Guided transport of atoms and Bose-Einstein condensation of ^{87}Rb

4.1 Introduction

This chapter details the loading of a single beam optical dipole trap. With atoms trapped we then demonstrate the guided transport of an atomic sample along the beam, up to a room-temperature dielectric surface. The technique exploits a simple hybrid trap consisting of a single beam dipole trap positioned $\sim 125\,\mu$m below the field zero of a magnetic quadrupole potential. Transportation is realised by applying a moderate bias field ($< 12\,$G) to displace the magnetic field zero of the quadrupole potential along the axis of the dipole trap. We use the technique to demonstrate that atomic gases may be controllably transported over 8 mm with negligible heating or loss. The transport path is completely defined by the optical waveguide and we demonstrate that, by aligning the waveguide through a super polished prism, ultracold atoms may be controllably delivered up to a predetermined region of a surface.

We go on to produce a ^{87}Rb condensate using the surface to selectively re-

move atoms as a final evaporation stage in addition to the more conventional method of direct evaporation in the optical trap. We compare the efficiency of evaporation to BEC in three different single beam optical traps using the direct cooling method. Finally we propose a potential scheme for the use of the transport method in future work.

4.2 Motivation: Moving atoms close to a surface

Understanding the fundamental forces which govern the world around us has long been a challenge for the scientific community. Of particular interest is the search for a comprehensive explanation of gravity. Newton published his theory of gravitation in 1687 [98] and since then attempts to experimentally verify its proposal have covered length scales from the astronomical [99] to the sub millimetre [100]. The results of such experiments have not only fundamental significance, but also important technological implications.

Although these experiments seek to, and have imposed, increasingly strict bounds on fundamental forces there are still many open questions regarding the possibility of short-range corrections to gravity which extend beyond the Standard Model. Despite the electromagnetic, strong and weak forces all being well described by quantum field theories, the current description of gravity set out by Einstein's theory of general relativity, which reduces to Newtonian gravity on everyday length scales, breaks down in the quantum limit and as such, is currently excluded from the Standard Model. As a starting point, many experiments look for deviations from the expected inverse square law, with new forces instead being characterised by a Yukawa type potential of the form

$$U(r) = \frac{-G_{\mathrm{N}} m_1 m_2}{r}(1 + \alpha \mathrm{e}^{-r/\lambda}), \tag{4.1}$$

where α is the strength of the force and λ its range. At the $1\,\mu$m level current experimental constraints permit these forces to be as large as 10^{10} times Newtonian gravity [101].

Attempts to measure the gravitational attraction between two masses have

improved dramatically from the first experiments by Cavendish in 1798 [102] and now vary widely in approach from superconducting gravity gradiometers [103] and microcantilevers [104] to planar oscillators [105] and torsion balance experiments [106]. However in scaling down experiments to probe ever decreasing length scales a new, fundamental problem arises. Quantum electrodynamics predicts a macroscopic force between conductors, known as the Casimir force [107]. This force vastly overwhelms the much weaker gravitational attraction between the test masses, such that experiments are forced to search for deviations between the theoretical and experimental Casimir forces. However, precisely calculating such Casimir forces for a specific macroscopic test mass near a surface is generally difficult [108]. In contrast the interaction between a single neutral atom and a plane surface is well understood [109, 110] being characterised by the attractive Casimir-Polder potential,

$$U_{\mathrm{CP}} = \begin{cases} U_{\mathrm{vdW}} = -\dfrac{C_3}{z^3} & \text{for } z < \lambda_{\mathrm{opt}}/2\pi, \quad (4.2) \\ U_{\mathrm{ret}} = -\dfrac{C_4}{z^4} & \text{for } \lambda_{\mathrm{opt}}/2\pi < z < \lambda_{\mathrm{T}}, \quad (4.3) \end{cases}$$

where for longer length scales the $1/z^3$ form of the van der Waals potential, characterised by C_3, becomes $1/z^4$ due to retardation effects. This new regime is characterised by C_4 with the transition point between the two regimes determined by the wavelength corresponding to the dominant excitation energy of the interacting atoms, λ_{opt} [111]. Further from the surface (larger than the thermal wavelength of photons, $\lambda_{\mathrm{T}} = \hbar c/k_{\mathrm{B}}T$) the interaction becomes dominated by the thermal fluctuation of the electromagnetic field [112]. In our case these length scales are $\lambda_{\mathrm{opt}}/2\pi \approx 0.12\,\mu$m and $\lambda_{\mathrm{T}} \approx 7.6\,\mu$m.

The inherent advantage of directly probing the atom-surface interaction has prompted the recent proposal of a new generation of experiments which aim to exploit the precision and control offered by atomic physics and ultracold quantum gases to push the measurement of short-range forces into a new regime [113, 114, 115, 116]. Indeed a number of proof-of-principle experiments have already utilised ultracold atomic gases to explore the short range van der Waals and Casimir-Polder potentials [117, 118, 119, 120]. Nevertheless such experiments are in their infancy and considerable refinement is

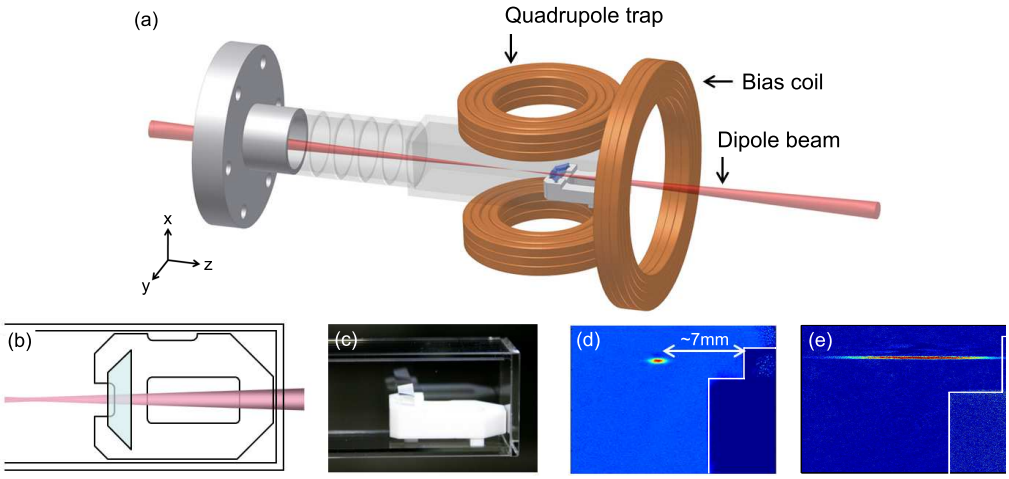

Figure 4.1: Experimental setup: (a) Trapping geometry near the surface. A single laser beam is delivered through the back surface of the glass prism, focussing 3.5 mm from its front surface. Axial confinement along the beam is provided by a magnetic quadrupole field. A single coil positioned behind the prism is used to produce a bias field to shift the location of the quadrupole field zero along the beam direction. (b) Schematic of the glass cell, the Dove prism, the macor prism mount and the dipole laser beam from above. (c) Photograph of the prism within the glass cell. (d) False colour absorption image of atoms trapped 7 mm from the prism surface. (e) False colour absorption image of atoms in the waveguide without magnetic confinement.

required before they become competitive with the classical 'Cavendish style' experiments as a test of short-range gravitational forces. Common to all these new atomic physics experiments is the need to controllably manipulate ultracold atoms near a room-temperature surface.

4.3 Experimental setup

Our approach uses a hybrid optical and magnetic trap formed from a single beam optical dipole trap positioned $\sim 125\,\mu$m below the field zero of a magnetic quadrupole potential (see Fig. 4.1(a)-(c)). For this first series of experiments the dipole trapping beam is derived from a $\lambda = 1030$ nm Yb disk laser (ELS Versadisk). The light is delivered close to the experimental chamber via a high power optical fibre before being focussed to a waist of

57 μm with an $M^2 = 1.06$ and Rayleigh range $z_R = 9.9$ mm. By positioning the beam below the field zero of the quadrupole trap (see section 4.5.1) we obtain the trapping potential shown in Fig. 4.2(a). The quadrupole gradient is usually set to approximately cancel gravity (30.6 G cm^{-1} for ^{87}Rb in the $F = 1, m_F = -1$ state) hence the full trap depth is determined by the dipole beam alone. However, if the dipole trap is positioned above the field zero, the trapping potential and the gravitational acceleration add to produce a tilted trap which lowers the potential barrier and hence trap depth as shown in Fig. 4.2(b).

4.4 Modelling the trap potential

It is important to fully understand the hybrid potential formed by the combined magnetic and optical trap if atoms are to be translated up to and away from the surface in a controlled way. The total potential seen by the atoms has four contributions,

$$U_{\text{total}} = U_{\text{dipole}} + U_{\text{mag}} + U_{\text{g}} + U_{\text{CP}}, \tag{4.4}$$

where U_{dipole} is the optical dipole potential, U_{mag} is the magnetic potential (consisting of both the quadrupole and bias fields), U_{g} is the earth's gravitational potential and U_{CP} is the potential produced by the atom-surface interaction. This net potential is depicted in Fig. 4.2(a) for a trap positioned far from the surface.

The optical contribution to the trap potential is modelled as a sum over any significant transitions from the ground state according to,

$$U_{\text{dipole}} = 3c^2 \left(\sum_i \frac{\Gamma_i}{\Delta_i \omega_{0_i}^3} \right) \frac{P}{w^2(z)} \exp\left(-\frac{2r^2}{w^2(z)} \right). \tag{4.5}$$

Here Δ_i is the laser detuning from the transition of frequency ω_{0_i} and natural linewidth Γ_i. P is the power of the dipole beam propagating in the z direction, $w(z)$ is the beam size, given by $w(z) = w_{0\text{M}}[1 + (z\lambda M^2/\pi w_{0\text{M}}^2)^2]^{1/2}$ (where $w_{0\text{M}}$ is the $1/e^2$ radius at the beam waist), and r is the radial distance from the beam centre.

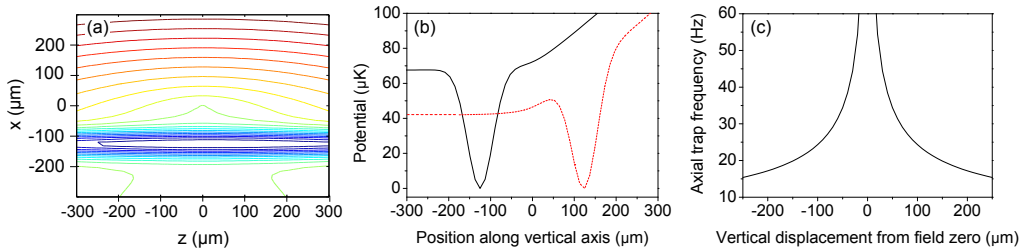

Figure 4.2: Potential produced by the single beam hybrid trap: (a) Equipotential of the hybrid trap in the plane $y = 0$ (see co-ordinate system in Fig. 4.1(a)). (b) The potential obtained in the x direction for a magnetically levitated trap with the dipole beam positioned 125 μm below (solid, black line) and 125 μm above (red, dashed line) the magnetic field zero. (c) Axial trap frequency as a function of vertical beam displacement from the magnetic field zero.

4.4.1 Case I: Idealised transport in the hybrid trap

In this hybrid trap configuration tight radial confinement is created by the dipole laser beam. Axial confinement along the beam is provided by the quadrupole field. (Without any magnetic confinement the cloud extends along the waveguide, centered around the beam waist, due to the low ($\sim$ 2 Hz) axial trap frequency produced by the dipole beam alone as shown in Fig. 4.1(e).) The axial potential produced by the quadrupole field is harmonic for $z \ll x_{\text{offset}}$ (where x_{offset} is the vertical separation between the beam and field zero) and linear otherwise. The harmonic trap frequency is determined by the quadrupole gradient and the vertical displacement of the beam from the field zero [91] as shown in Fig. 4.2(c). Here the quadrupole gradient is sufficient to support atoms against gravity. In this hybrid trap the position of the atoms along the dipole beam is determined not by the beam waist but instead by the location of the quadrupole trap centre. The application of a horizontal bias field parallel to the dipole beam produces a shift of the field zero along the direction of the beam. In this way atoms can be transported along the length of the dipole beam and delivered up to a region of the prism surface determined solely by the path of the dipole trapping beam.

4.4.2 Case II: Transport with an offset bias field

In the idealised case the application of the bias field moves the field zero purely along the z-axis thus keeping the distance between the dipole beam and the field zero, and hence the axial trap frequency, constant. However, due to physical constraints of the apparatus it is unfeasible to position a pair of bias coils symmetrically about the beam. Instead we must use a single coil, displaced 17 cm in the z-direction from the field zero. Additionally the symmetry axis of the coil is offset 1.5 cm vertically. Theoretically accounting for the offset of the bias coil produces small deviations from the trapping expected for displacement along a Gaussian beam. This is the result of the trajectory taken by the field zero as the bias field is increased due to a non-axial magnetic field component produced by the offset of the bias coil. As shown in Fig. 4.2(c) any vertical displacement translates into a change in axial trap frequency. The theoretical model of this axial frequency change is shown, along with experimentally determined values, in section 4.6.2. However, we stress that even in this non-ideal case the atoms are still transported along the dipole beam regardless of the exact path of the magnetic field zero.

4.5 Production of ultracold gases near a dielectric surface

4.5.1 Loading the hybrid trap

As described in chapter 3, to prepare the atomic sample ^{87}Rb atoms are loaded from a magneto-optical trap (MOT) into a quadrupole trap mounted on a motorised translation stage. Once loaded, this quadrupole trap is moved horizontally, transporting the atoms towards a second, static quadrupole trap (shown in Fig. 4.1(a)) into which the atoms are transferred. The atoms are then further cooled by forced RF evaporation resulting in a sample of 2.7×10^7 atoms at a temperature of 32 μK.

To load the hybrid dipole trap the quadrupole gradient is relaxed from 192 G cm^{-1} down to 29.3 G cm^{-1} in 1 s. The combined potential produced

by the laser beam and quadrupole field results in trap frequencies of $\omega_r = 2\pi \times 480\,\text{Hz}$ and $\omega_z = 2\pi \times 24\,\text{Hz}$ at the beam waist. To optimise the loading of the trap, the positioning of the beam relative to the quadrupole field zero is of great importance. We demonstrate this by scanning the beam using the final steering mirror in the optical setup and measuring the atom number after a 500 ms hold in the trap. From Fig. 4.3 it is possible to roughly determine the position of the field zero in the beam scan. Here atoms are lost from the trap as a result of Majorana spin flips and hence a dip in atom number is observed.

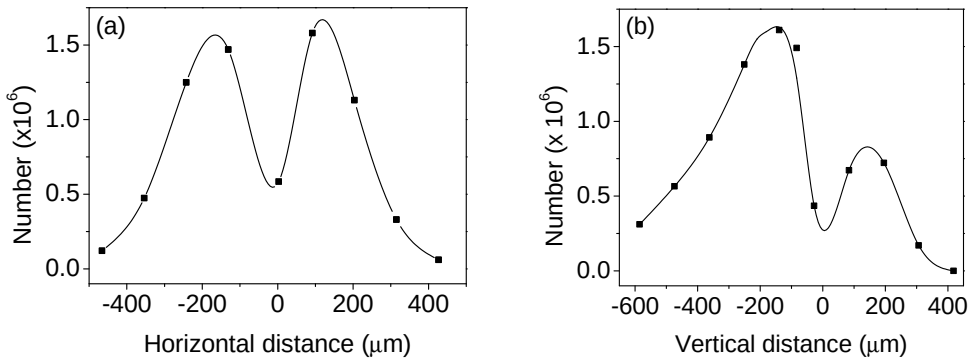

Figure 4.3: Aligning the single beam trap: Atom number in the trap is maximised by scanning the dipole beam horizontally (a) and vertically (b) using the final steering mirror. In both scans the position of the magnetic field zero presents itself as a drop in atom number between two peaks. Lines shown are as a guide only.

As a brief aside, it is interesting to note how the position of the dipole beam affects other important parameters. Fig. 4.4 shows the dependence of the number, phase space density and axial trap frequency on relative beam displacement from the field zero. (Note this data is for a different beam waist than that described in the rest of this chapter, hence the offset in the maximum number position compared to Fig. 4.3(b).) Although it can be advantageous in terms of the number of atoms loaded into the trap to be far below the field zero there is a significant gain in axial trapping frequency as this separation is decreased. The knock-on effect is an improvement in phase space density, often sufficient to merit a trade off - reduce the number of atoms transfered by moving the beam closer to the field zero but ultimately

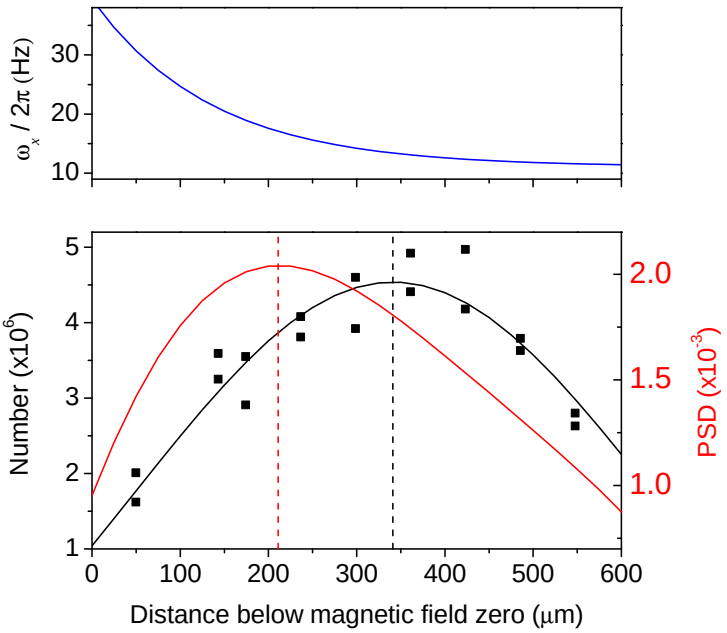

Figure 4.4: Effect of dipole beam position relative to the magnetic field zero in a hybrid single beam trap: Although the peak in the atom number (black) may appear the optimum position for loading the dipole trap it is important to account for the change in axial trap frequency (blue) as the beam is moved further from the quadrupole zero. The change in frequency impacts on the PSD (red) of the trapped cloud, hence it may be advantageous to load the trap with the beam closer to the field zero in order to maximise the PSD and elastic collision rate (which follows the same position dependence). The dotted lines give an indication of the vertical position of the peaks in both number and PSD.

gain in phase space density. The elastic collision rate also follows a very similar position dependence to the phase space density. Experimentally we find that the evaporation performance can be improved by again moving the beam closer to the field zero.

4.5.2 Trap frequency measurement: Parametric heating

In this hybrid optical and magnetic trap the radial trap frequencies are dominated by the dipole laser beam. The frequencies associated with the optical

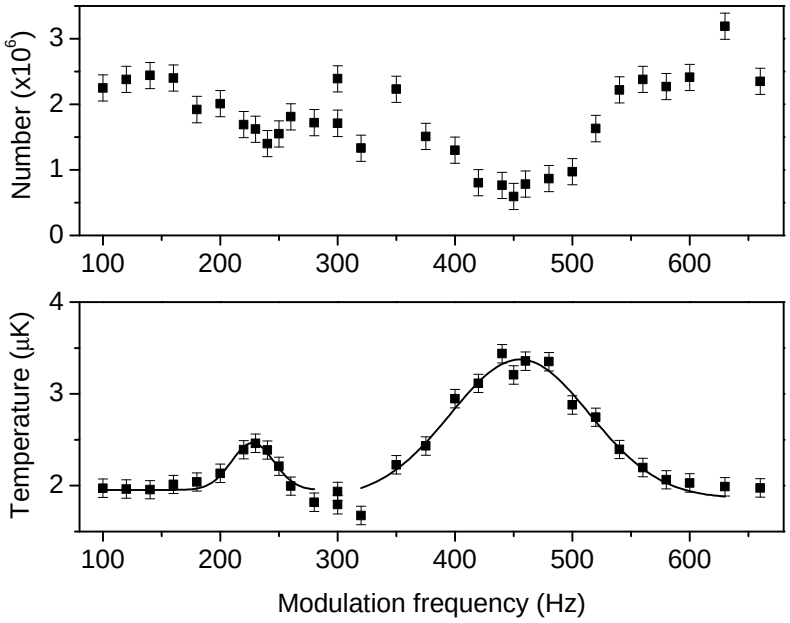

Figure 4.5: Parametric heating: Modulating the dipole trapping light causes heating of the atoms at the resonant frequency (and harmonics) of the trap, also leading to atom loss. Fitting the temperature curve using a Gaussian profile allows these resonant frequencies to be extracted.

trap can of course be predicted from the known beam parameters (i.e. beam waist, power) and are approximately given by [91],

$$\omega_{\mathrm{r}} \approx 2\sqrt{\frac{U}{mw_{0\mathrm{M}}^2}}. \tag{4.6}$$

However, measuring this in situ using the atoms themselves is useful to ensure the beam is correctly aligned and performing as expected. We measure the radial trap frequency using parametric heating. By adding a sinusoidal modulation to the optical trapping light it is possible to create a driven oscillator system. This then exhibits resonant behaviour at ν and 2ν causing the atoms in the trap to be heated and, in some cases, lost from the trap. More specifically, position noise (resonant at ν) leads to a constant heating rate whilst intensity fluctuations, resonant at 2ν, lead to an exponential growth of energy [121].

The results of the trap modulation are shown in Fig. 4.5 for a trap using one quarter of the full beam power. Here atoms are first evaporatively cooled to

increase the optical depth of the cloud. Following a short hold the modulation is applied for 3 s (by summing the normal optical trapping light control signal with a sinusoidally varying term, a 0.1 V modulation on a 2 V signal). Fitting the temperature data, as this produces a cleaner signal, it is possible to extract the frequency of the fundamental and first harmonic, 227(3) Hz and 454(4) Hz, respectively. These frequencies are not only in excellent agreement with each other but also with those predicted from the known beam parameters, confirming the measured beam waist of 57 μm.

4.5.3 Trap frequency measurement: Axial oscillation

The axial trapping along the length of the laser beam is given by [91]

$$\omega_z = \frac{1}{2}\sqrt{\frac{\mu B'}{m x_{\text{offset}}}}, \tag{4.7}$$

where x_{offset} is the position of the trap minimum, effectively describing the distance between the beam and the field zero. As the trapping in this direction is largely dominated by the contribution of the magnetic quadrupole trap parametric heating is an unsuitable method to measure the trap frequency in this direction. Instead we measure the oscillation of the cloud in the trap by applying a small bias field to first offset its position and then abruptly switching off the field, setting the atoms in motion. By measuring the position of the atoms at various hold times after the field switch off the motion of the atoms can be tracked. The oscillation is then fitted using a damped sine wave to extract the period as shown in Fig. 4.6(a). From this we obtain an axial trap frequency of 18(1) Hz.

Importantly the oscillation amplitude must be small compared to the cloud size (210 μm) and ideally the excursion of the atoms should be sufficiently small that they remain in the harmonic region of the trapping potential, see Fig. 4.6(b). Beyond this, atoms start to sample the linear regions of the trap, dominated by the quadrupole potential, and the assumption of harmonic motion used in the fit to extract the trap frequency breaks down.

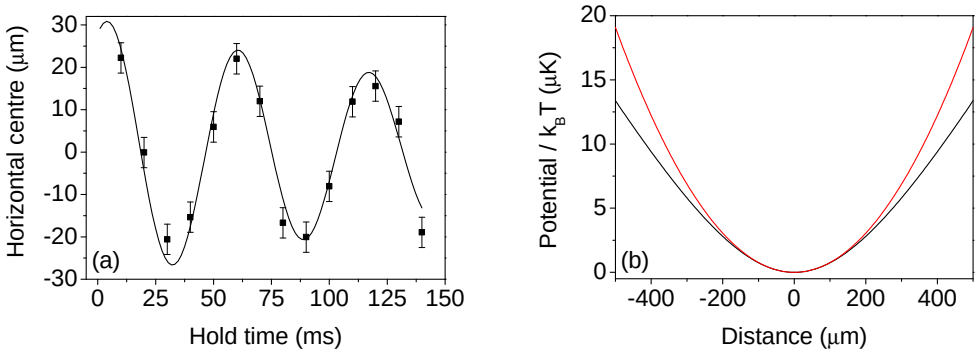

Figure 4.6: Axial trap frequency: (a) Atoms offset in the trap using a small bias field begin to oscillate under the influence of the axial magnetic trapping. Fitting a damped sine wave allows the period of the oscillation and hence the trap frequency to be extracted. (b) The axial trapping remains harmonic (red) over a small region close to the trap centre. Further away, the potential becomes dominated by the linear quadrupole potential (black).

4.6 Displacement of the cloud along the dipole trap laser beam

After loading, the cloud rapidly equilibrates to around $U_0/10$, where U_0 is the depth of the trap (this fraction we experimentally verify in section 4.6.2). For the parameters of our trap this equates roughly 7 μK. Further evaporation can then be performed by reducing the beam intensity. Throughout all experiments the laser beam propagates through the rear anti-reflection (AR) coated face of the Dove prism, along the axis of the glass cell (see Fig. 4.1). The waist is positioned 3.5 mm from the front super-polished surface. Initially the quadrupole trap centre is located 6.8 mm from the prism surface, as shown in Fig. 4.1(d). This geometry is chosen such that in moving up to the surface the cloud is always confined less than half a Rayleigh range from the beam waist, leading to minimal variation in the radial trapping potential. The cloud can be moved closer to and further from the prism by application of the bias field (where a positive displacement moves the cloud from the initial quadrupole trap centre, closer to the surface) as shown in Fig. 4.7.

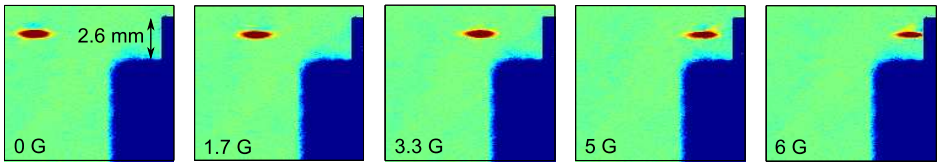

Figure 4.7: False colour absorption images of atoms approaching the surface: Bias fields applied range from 0 G to 9.5 G. To the right of each image the glass prism can be seen sharply defined on top of its macor mount (unfocussed edges).

The magnitude of this shift is given by,

$$z = \frac{B_{0,z}}{B'_x/2}, \tag{4.8}$$

where $B_{0,z}$ is the applied bias field and B'_x is the quadrupole field gradient along the axis of the coils. For the (approximately) levitated potential the use of $-12\,\mathrm{G} \leq B_{0,z} \leq 12\,\mathrm{G}$ produces displacements of $-8.2\,\mathrm{mm} \leq z \leq 8.2\,\mathrm{mm}$, on the order of a Rayleigh range ($z_R = 9.9\,\mathrm{mm}$).

4.6.1 Speed of transport

The maximum speed of the cloud transport without setting up sloshing in the trap is governed by the magnetic field gradient used to close off the trap along the axis of the dipole beam. Ideally the bias field ramp should be adiabatic to reduce any heating effects. This can be experimentally investigated by measuring the amplitude of the oscillation induced by the transportation. In order to map out the oscillation, absorption images of the cloud are taken after quarter trap period time steps for atoms at temperatures of $1.5\,\mu\mathrm{K}$ and $7\,\mu\mathrm{K}$. Figure 4.8(a) shows that to complete a shift of 4.2 mm without setting up an oscillation requires a ramp time of $\sim$ 2.5 s. As expected, this is independent of cloud temperature. In principle this time can be reduced with the use of a tighter field gradient at the expense of requiring a higher bias field.

4.6.2 Characterisation of the hybrid trapping potential: A 'single-shot' diagnostic

With the flexibility to displace the trap centre anywhere along the beam, it is possible to use the trapped atoms to characterise the profile of the dipole beam. We use a 'single-shot' diagnostic routine to measure important trap properties quickly and reliably. This approach is suitable when high radial trap frequencies are used, for example in single beam dipole traps. After a time of flight, τ_{TOF}, the width of the cloud, σ_i, is given by

$$\sigma_i^2 = \left(\frac{k_{\mathrm{B}}T}{m\omega_i^2}\right)(1+\omega_i^2\tau_{\mathrm{TOF}}^2). \tag{4.9}$$

In the limit that $\omega_i\tau_{\mathrm{TOF}} \gg 1$, i.e. in the case of the radial trap frequency, the cloud width after time of flight is governed only by the cloud temperature and not the frequency of the trap at release. Hence, it is possible to determine the cloud temperature without prior knowledge of the trapping potential in a single shot. The axial trap frequency can then simply be calculated from the axial cloud size and the temperature (assuming thermal equlibrium) as determined from the radial size. If the cloud is held in the trap sufficiently long before release such that the gas reaches full thermal equilibrium with the potential, the radial trap frequency can also be derived from this measurement; knowledge of the dipole trap beam power together with the assumption that the cloud equilibrates to some fraction of the trap depth, $1/\eta$, (which we establish later in this section) allows the $1/e^2$ beam radius and hence the radial trap frequency to be determined from the temperature measurement. Such measurements are found to be in good agreement with the values obtained from parametric heating (see section 4.5.2). This method allows the position of the beam waist to be located precisely and the distance between the magnetic field zero and the dipole beam to be determined over the full range of transport distances.

Figure 4.8(b) shows the effect of transport along the beam on atom number for a cloud initially allowed to come into thermal equilibrium with the trapping potential through evaporation. For shifts sufficiently far from the prism such that the atoms do not interact with the surface, there is no detectable atom loss. Closer to the prism there is a sharp drop in the atom number,

the red (open) circles, as the atoms hit the surface (see section 4.7). The effect of the same transport on the cloud temperature is shown Fig. 4.8(c). The observed temperature change is due simply to the adiabatic compression and relaxation of the cloud as the radial trapping potential varies along the optical waveguide and not as a result of a heating mechanism associated with the motion of the cloud. Knowing the beam power at the trap and the beam waist (determined from parametric heating measurements) it is possible to model the trap depth along the waveguide. The solid line in Fig. 4.8(c) demonstrates that the temperature data are consistent with a cloud in thermal equilibrium with the trapping potential for $\eta \approx 9$. Note again the two red (open) circles correspond to a shift sufficient for the surface potential to open up the trap, hence reducing the trap depth and leading to atom loss. As such, we do not expect agreement with the model potential for these points. To test explicitly for heating due to the transport, measurements were performed shifting a cloud cooled to 1/20 of the trap depth to suppress evaporation. Under such conditions some moderate heating was observed. For example, for a $1\,\mu$K cloud transported a round trip distance of 8 mm, heating rates of $\sim 0.1\,\mu\mathrm{Ks}^{-1}$ were observed for speeds that do not excite axial oscillations (see Fig. 4.8(a)). However, the fact that the cloud remains in thermal equilibrium with the trapping potential (Fig. 4.8(c)) and the absence of any atom loss (Fig. 4.8(b)) demonstrates that this does not prohibit efficient transport of the atoms.

Analysis of the measured axial trap frequency moving along the beam confirms the theoretical prediction (solid line Fig. 4.8(d)) that the vertical distance between the beam and the magnetic field zero does not remain constant when applying a bias field as a result of the bias coil's spatial offset from the beam axis. This leads to the small but measurable variation in trap frequency evident in Fig. 4.8(d). However, this would be eliminated with a coil arrangement producing a field in the axial direction only.

4.7 Loss due to the surface

Far away from the surface, the atomic cloud is unperturbed by displacement

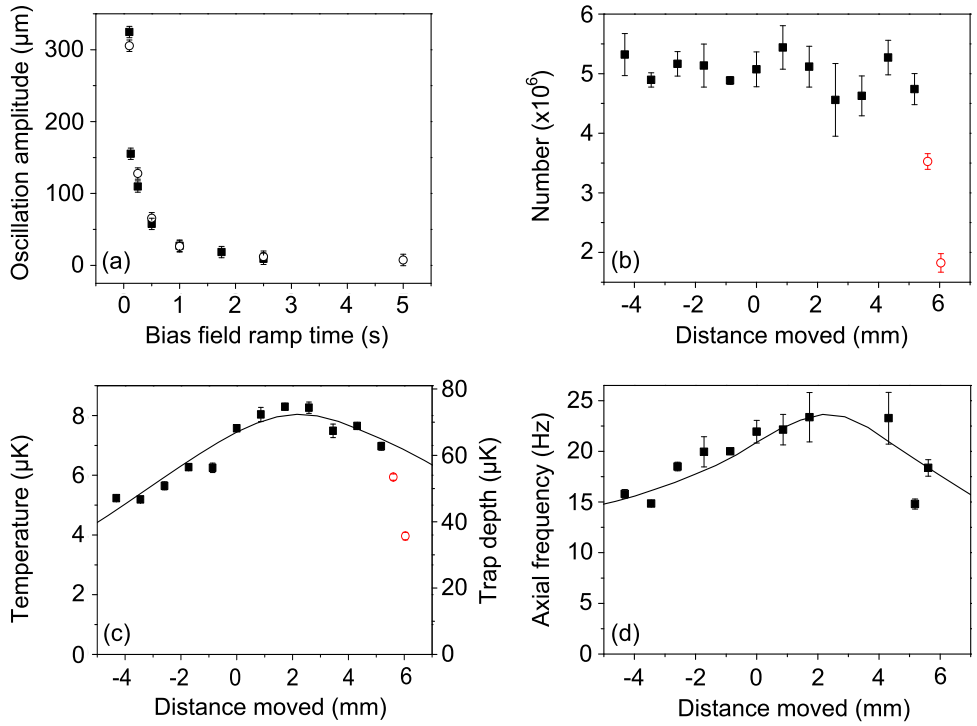

Figure 4.8: Characterisation of the transport along the waveguide: (a) Oscillation set up by shifting the cloud 4.2 mm by displacement of the magnetic field zero in different lengths of time. Filled squares are for a cloud at 1.5 μK. Open circles are for a cloud at 7 μK. (b) Atom number as a function of horizontal trap shift caused by movement of the quadrupole field zero along the dipole beam. Red circles are for clouds sufficiently close to the surface that atoms are lost due to the atom-surface interaction opening up the trapping potential. (c) Vertical cloud temperature as a function of horizontal trap shift. Red circles are for clouds sufficiently close to the surface that atom loss from the cloud becomes a factor in the temperature. Solid line: Theoretical trap depth calculated from known dipole and quadrupole trap properties, accounting for an off axis bias field. Note the scale is $\times 9$ that of the experimental data indicating $\eta = 9$ (see text). (d) Experimentally determined axial trap frequency derived from the radial temperature and axial size of the cloud after time of flight. Solid line: Theoretical axial trap frequency calculated from known dipole and quadrupole trap properties, accounting for off axis bias field. Displacements are with reference to the initial quadrupole trap centre location with no applied bias field.

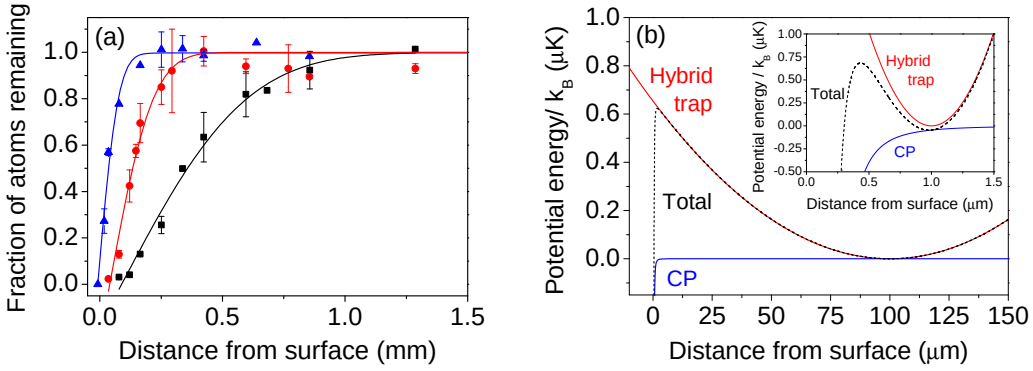

Figure 4.9: Atoms near the surface: (a) Atom loss as a function of distance from the prism surface for cloud temperatures of 7.0 μK (black squares), 1.4 μK (red circles) and 0.3 μK (blue triangles). Fitted lines are of the form $N = N_0 \mathrm{erf}((z - z_0)/(\sqrt{2}\sigma))$ for $z > z_0$. (b) Total trapping potential resulting from the hybrid trap and Casimir-Polder (CP) atom-surface potential when the trap is positioned 100 μm from the prism. Inset: The same resultant potential for a much tighter trap (4.5 kHz) located only 1 μm from the surface.

along the beam. However, once the distance of the trap centre from the surface becomes comparable to the axial cloud size, atom loss is observed. This is a direct consequence of the strong attractive Casimir-Polder potential leading to a finite trap depth along the optical waveguide (see Fig. 4.9(b)). Atoms whose energies are sufficient to escape over the finite barrier collide with the surface and are either adsorbed or re-emitted at room temperature speeds. In this way the surface may be used as a knife for evaporative cooling [122]. We demonstrate how the atom loss caused by a controlled contact with the surface can be used to infer properties of the cloud such as size and temperature. We then proceed to produce a Bose-Einstein condensate by exploiting the evaporation of hot atoms at the surface.

To probe the atom loss as the cloud approaches the surface, we begin by loading atoms into the hybrid trap with no initial bias field and allowing the cloud to equilibrate to 7 μK . The bias field is then ramped to the necessary level in 5 s. Following this, the cloud is held at the shifted location for 50 ms (on the order of one axial trap period) before being shifted away from the surface a short distance and imaged. In the case of the colder cloud (1.4 μK) an evaporation ramp in the dipole trap is first applied before the cloud is

displaced along the beam. To produce the coldest cloud near the surface (0.3 μK) an initial dipole evaporation stage is carried out and the cloud is shifted 0.8 mm from the prism before a further evaporation stage is employed to reach the final temperature.

The results of the measurement of loss due to the surface are shown in Fig. 4.9(a) as a function of the distance from the trap centre to the surface. Assuming harmonic axial confinement, it is possible to fit the observed atom loss as function of distance using an error function of the form

$$N = N_0 \mathrm{erf}\left(\frac{z - z_0}{\sqrt{2}\sigma}\right), \tag{4.10}$$

for $z > z_0$ where N is the number of atoms remaining at a given distance z from the surface, N_0 is the initial atom number far from the surface and σ is the cloud width. The offset z_0 accounts for the observation that, for the hotter clouds, complete atom loss occurs well before the trap centre reaches the prism. From the fit of Eq. (4.10) to the loss data we find the cloud widths to be 400(20) μm (for the 7.0 μK cloud), 140(20) μm (1.4 μK cloud) and 65(6) μm (0.3 μK cloud). Converting these widths to temperatures using $\sigma = (k_B T/m\omega_z^2)^{1/2}$ we find reasonable agreement with time of flight measurements for the colder clouds. For the hotter clouds the anharmonic nature of the axial confining potential leads to deviations from the simple theoretical lineshape given by equation (4.10).

The atom loss shown in Fig. 4.9(a) can be understood by consideration of the competing potentials as the hybrid trap is brought close to the surface. Figure 4.9(b) shows the result when the hybrid trap ($\omega_z = 2\pi \times 18$ Hz) is positioned 100 μm from the surface. At these length scales the strong atom-surface potential causes a truncation of the harmonic trap resulting in a reduced trap depth. This leads to loss of hot atoms from the trap. The offset parameter z_0 can be understood by assuming that, due to finite signal to noise, all the atoms appear to be lost when the trap depth is reduced to 5 – 10 % of the initial cloud temperature. For example, for the cloud temperatures used in the experiment this reduction to 5 % occurs for trap-surface distances of 72 μm (for the 7.0 μK cloud), 32 μm (1.4 μK cloud) and 15 μm (0.3 μK cloud). These distances are broadly in agreement with the observed offsets in Fig. 4.9(a).

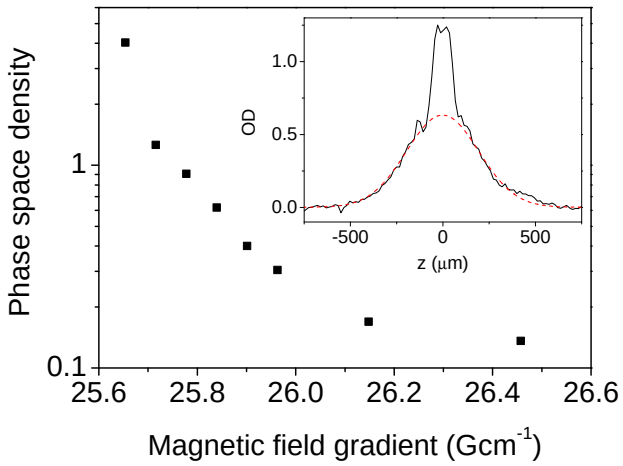

Figure 4.10: Cooling through the BEC transition using the surface: Phase space density as a function of magnetic field gradient for a fixed dipole beam intensity for a cloud initially positioned to be just in contact with the surface. Inset: Cross section through a cloud, initially at 1.5 μK and a phase space density of 2×10^{-2}, following evaporation to degeneracy using the surface.

4.8 Evaporation to ^{87}Rb BEC

4.8.1 Controlled evaporation using a surface

This truncation of the trapping potential by the surface, if controlled, can also be used to cool the trapped atoms. Relaxation of the field gradient reduces the trapping along the dipole beam thus allowing atoms to extend outwards from the trap centre, towards the prism, coming into contact with the 300 K surface. The resulting atom loss due to the surface is very similar to the application of an RF knife to selectively remove the most energetic atoms. Carrying out evaporation in this way allows the BEC transition to be reached (see Fig. 4.10) without the need to reduce the dipole intensity which would otherwise reduce the radial trapping.

Due to the limited and hence inefficient evaporation surface produced by the trapping geometry we are unable to evaporate to degeneracy solely using this surface technique. (The elongated geometry created by the hybrid trap and

its orientation relative to the surface means atoms are cut away only from a single narrow end of the cigar shaped trap). Instead some initial cooling must be carried out by lowering the dipole trap depth. In this first stage we prepare a cloud at 1.5 μK with a PSD of 2×10^{-2}. We then shift the atoms close to the surface (a transport of $\sim$6 mm) and relax the quadrupole trap gradient over 5 s. After a 5 ms hold the atoms are then shifted back a short way from the surface before imaging. The condensates created in this way are generally small, containing only a few 10^4 atoms.

4.8.2 Direct evaporation in the optical trap

Although the demonstration that a room temperature surface can be used to selectively evaporate atoms from a trapped cloud is in itself novel, the efficiency with which the evaporation occurs is not so remarkable. Instead it is therefore more sensible to continue with direct evaporation to BEC; selectively removing the hottest atoms by reducing the trap depth.

To reach degeneracy a series of 10 s linear ramps, each time quartering the dipole beam power are carried out, followed by a 5 s hold step after each to allow the cloud to rethermalise. The evaporation trajectory for the 57 μm trap (initial U_0=63 μK) is shown in Fig. 4.11. Also shown is the trajectory in an alternative trap with more power but a much larger waist, 9.4 W of $\lambda = 1064$ nm light focussed to 160 μm (initial U_0=37 μK). This larger trap has radial frequencies around a factor of 4 less than that of the 57 μm beam. For comparison the trajectory of one further single beam trap with a waist of 136 μm and 11.1 W of power (initial U_0=56 μK) is also shown (this forms the first of our crossed dipole trap beams as described in chapter 5).

From Fig. 4.11 we note an obvious characteristic of ^{87}Rb sadly not mirrored by the other isotope. The condensation of ^{87}Rb benefits greatly from a trap with a narrow waist and high trapping frequencies. This increases the elastic collision rate and hence evaporation and rethermalisation proceed rapidly. This is illustrated by the slopes of the data in Fig. 4.11. For the 57 μm trap the efficiency (gradient of the trajectory) is $\sim$2.8(2) whereas in the weaker 160 μm trap this drops to only 2.0(1). Therefore the most efficient way to produce ^{87}Rb BECs is to keep traps tight and collision rates high. As we will

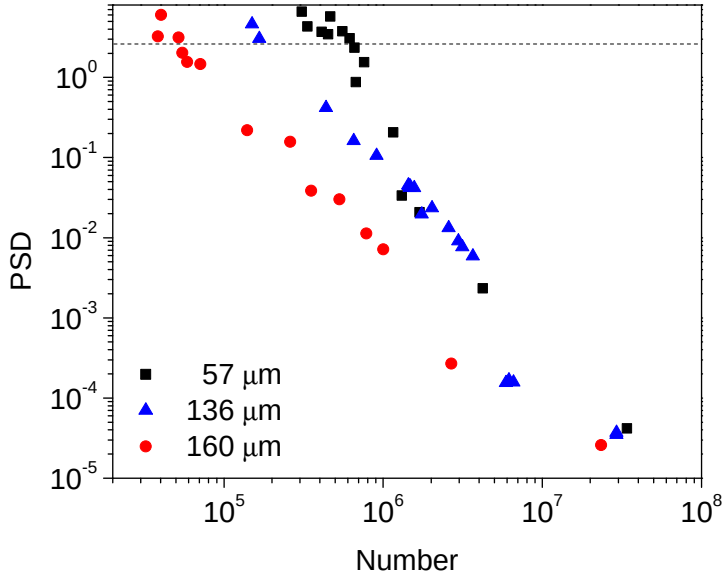

Figure 4.11: ^{87}Rb BEC in a single beam dipole trap: Evaporation trajectory for ^{87}Rb cooled in three, single beam optical dipole traps with differing waists, 57 μm, 136 μm and 160 μm. The dotted line shows the BEC transition point, PSD= 2.61.

see in section 6.3, a combination of inelastic losses and reductions in elastic scattering rates will make the route to ^{85}Rb BEC far less trivial.

4.9 Outlook: Future applications of the guided transport method

Although the main thrust of our current investigation is to study the formation of bright matter-wave solitons using a ^{85}Rb BEC, in the long term the technique described in this chapter could be used to load an optical trap in the vicinity of the surface which is suitable for studying atom-surface interactions. Typically such a trap needs to be tightly confining [119, 123, 124, 125, 126] so that the spatial extent of the atomic cloud becomes comparable to the range of the Casimir-Polder potential. This allows the atomic gas to be positioned much closer ($< 10\,\mu$m) to the surface. For example, the inset to Fig. 4.9(b) shows the resulting trapping potential for a 4.5 kHz harmonic trap positioned at a distance of 1 μm from the sur-

face. At such length scales the Casimir-Polder potential leads not only to a reduction in the trap depth but also to a change in the trapping frequency, an observable which can itself be useful [127].

The use of a Dove prism in our experiment permits the addition of evanescent wave potentials at the surface through the total internal reflection of light within the prism. In particular, the use of a blue-detuned laser will create a repulsive barrier close to the surface (an evanescent wave atomic mirror [128, 129, 130, 117, 131, 132, 133]) that will prevent the observed loss as the atoms are transported up to the surface.

Unlike previous magnetic transportation schemes [134], the work presented here benefits hugely from the optical waveguide used to confine the atoms radially. This leaves the transport path insensitive to stray magnetic fields as the atoms are guided along the beam towards the target point on the surface. The technique also has the advantage of simplicity over other transport schemes involving optical lattices [135, 123].

Following the transport the atoms will then be loaded into a tight surface trap created either by the addition of a second red-detuned evanescent field [136, 137, 138, 139] or by the reflection of a red-detuned laser incident at a shallow angle on the surface from the vacuum side. The latter approach can be used to generate a 1D optical lattice close to the surface [126] which can potentially be tailored in order to test a number of novel schemes to measure the atom-surface potential, including interferometry in a double-well potential [140] and the study of Bloch oscillations [141].

Ultimately, to probe short range corrections to gravity will require a detailed comparison of the measured and theoretical Casimir-Polder potentials. Pushing ultracold atom experiments to the precision to be competitive with traditional approaches will be challenging and will undoubtedly require the development of further techniques to transport and manipulate atomic gases close to surfaces.

4.10 Summary

In this chapter we have demonstrated the successful transport of an atomic sample along an optical waveguide up to a room-temperature dielectric surface. The technique exploits a simple hybrid trap consisting of a single beam dipole trap positioned $\sim 125\,\mu$m below the field zero of a magnetic quadrupole potential. Transportation is realised by applying a moderate bias field ($< 12\,$G) to displace the magnetic field zero of the quadrupole potential along the axis of the dipole trap. We use the technique to demonstrate that atomic gases may be controllably transported over 8 mm with negligible heating or loss.

The transport path is completely defined by the optical waveguide and we demonstrate that, by aligning the waveguide through the super polished Dove prism, ultracold atoms may be controllably delivered up to a predetermined region of the surface. Upon approaching the surface we observe strong atom loss once the distance of the trap centre from the surface becomes comparable to the axial cloud size. This is simply a direct consequence of the presence of the surface leading to a reduced trap depth along the optical waveguide. Such loss is akin to evaporative cooling and, indeed, we demonstrate how the effect can be utilized to cool an atomic gas through the transition to a Bose-Einstein condensate.

Using the more conventional approach of lowering the dipole trap depth we also reach BEC in this narrow single beam trap and compare this evaporation trajectory using three different beam waists. In doing so we highlight the advantage of tight traps for the cooling of ^{87}Rb but ultimately must move away from this geometry if we are to produce a ^{85}Rb condensate. In the next chapter we develop a new, larger volume crossed beam trap better suited to the creation of ^{85}Rb condensates. However, we will return to this single beam geometry in chapter 7 where we show a similar transport scheme can be used to manipulate the velocity of a solitary wave propagating in an optical waveguide.

Chapter 5

^{87}Rb Bose-Einstein condensation in a crossed dipole trap

5.1 Introduction

It has been shown previously [30] that to achieve Bose-Einstein condensation of ^{85}Rb requires the use of a magnetic Feshbach resonance, allowing one to tune the elastic and inelastic scattering properties of the atoms. To access the broad resonance in the $F = 2, m_F = -2$ state, this means the application of a 155 G bias field. Unfortunately, this field pushes the quadrupole field zero far away from the dipole trap, dramatically reducing any confinement along the length of the beam. Although the drop in density is favourable in terms of 3-body loss, rates of which are high in ^{85}Rb, the low trapping frequency is detrimental to the rethermalisation process required for evaporative cooling. As such, the single beam trap described in chapter 4 is unsuitable for the cooling of ^{85}Rb to degeneracy.

In this chapter we address this problem, describing the development of a crossed beam dipole trap. Here horizontal confinement is created by the intersecting beams. To take full advantage of the beam power available, we use a single dipole beam in a 'bow-tie' layout. It is possible to produce a crossed trap with or without the addition of the quadrupole potential and

we discuss the differences between these cases. Initial characterisation of the crossed trap is carried out using ^{87}Rb for simplicity and we demonstrate Bose-Einstein condensation in 3 distinct crossed trap configurations. Finally we explore the effect of polarisation on the crossed trap, creating a ^{87}Rb BEC in an optical lattice, and observe the effect of Kapitza-Dirac scattering.

5.2 Setup and alignment

5.2.1 Experimental setup

For our crossed beam trap we require an entirely new optical trapping layout. The ELS disk laser used for the work described in chapter 4 is no longer used but instead a single frequency IPG 15 W fibre laser (IPG: YLR-15-1064-LP-SF) takes its place. Whilst working with the ELS laser it became apparent that thermal lensing effects played an important role in determining the waist size and position of the output beam. As a result, changes in the laser current or even the temperature of the external cooling circuit were sufficient to entirely change the laser output and hence the geometry of the optical trap. For example, the beam waist was found to change by as much as 15 %, with its location also shifting by around 15 mm. Although the problem of the beam profile could be partially circumvented with the implementation of high power optical fibres, the fibre input was still limited to $\sim$5 W and therefore the power available at the trap to $\sim$3 W, only a fraction of the laser's 50 W maximum output. The fibre laser employed as a replacement not only solves this problem of a changing beam profile but allows us access to much higher trapping powers, on the order of 11 W at the trap itself.

With this increased power it then becomes possible to create a larger volume trap (by increasing the beam sizes). Brief, preliminary investigations loading ^{85}Rb into the 57 μm trap showed that the small beam waist and high trap frequencies resulted in an inefficient transfer of atoms into the optical trap and poor efficiency of the subsequent evaporation. This is to be expected from consideration of the elastic and inelastic scattering properties of ^{85}Rb (discussed in greater detail in chapter 6). The greater power available therefore means a larger volume trap can be produced yet still with sufficient trap

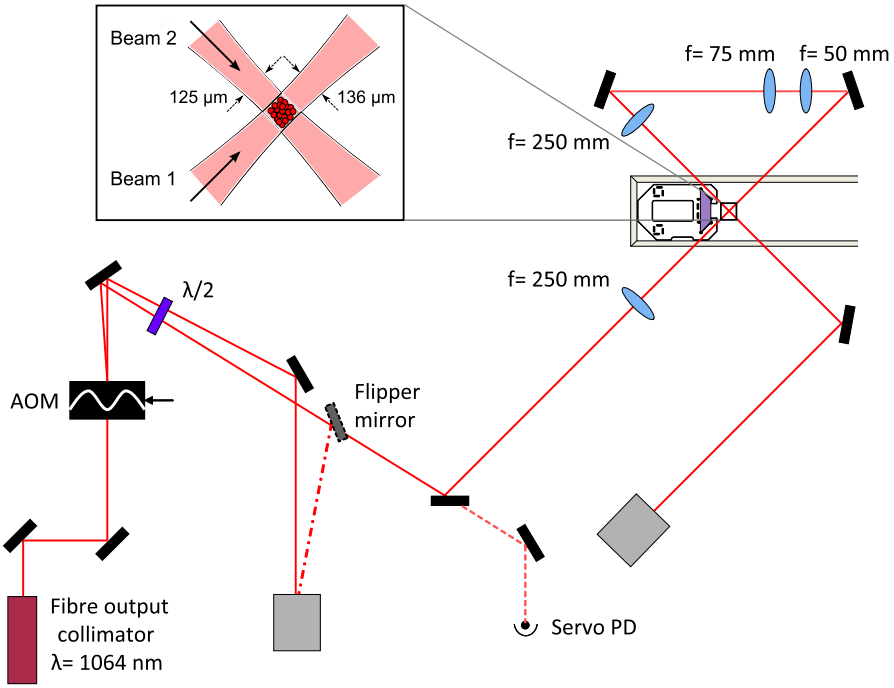

Figure 5.1: Optical trapping layout for the crossed beam trap: Light for the optical trap is derived from an IPG fibre laser. From the fibre output collimator the light passes through an AOM, used for intensity control, before being focussed down into the glass cell. Initially the light is vertically polarized to maximise the diffraction efficiency of the AOM however a $\lambda/2$ plate after the AOM rotates the light to be horizontally polarized to reduce reflection losses at the glass cell. A motorised flipper mirror safely directs the first order beam from the AOM into a beam dump when it is not needed but allows the RF power in the AOM to be kept high to avoid thermal effects.

depth to ensure a reasonable transfer of atoms from the magnetic trap.

The experimental setup used to create the optical trap is shown in Fig. 5.1. The dipole beam first enters the cell at 45° to the glass, focussing down to 136(1) μm. The polarisation here is set to be horizontal to minimise reflections. To form the crossed trap the beam which exits the cell must be reshaped before being refocussed back into the trap. A telescope is used to increase the beam size before a final lens focusses the beam down to 125(5) μm. Although the setup contains only one laser beam, for clarity, we refer to the beam entering the cell from the IPG laser as 'beam 1' and the second, reshaped beam, as 'beam 2'. Intensity control of the beam is achieved using a single AOM with servo feedback control.

This choice of beam waists was an informed one, based on previous measurement of the evaporation of ^{85}Rb in smaller traps (formed from the ELS and IPG lasers each producing one beam of a crossed trap) which proved unsuccessful[1]. In creating a trap with larger waists (and hence lower trap frequencies) the devastating density dependent losses prevalent in ^{85}Rb can be reduced, however, there is a limit to how much we may increase our beam sizes. As the optical trap is loaded from the magnetic quadrupole an important consideration is the depth of the optical potential. Due to the constraints of the laser power available, to obtain a reasonable trap depth, ~ 100 μK, the beam waists cannot be increased much further than those chosen hence we arrive at our current experimental parameters. A coincidental advantage of such large beam waists is the size of corresponding Rayleigh range, 5.5 cm (4.6 cm) for the 136 μm (125 μm) beam, which makes aligning the focus of the trap considerably easier.

5.2.2 Alignment

The alignment of beam 1 is carried out in much the same way as the single beam hybrid trap described in section 4.5.1. However, as the crossed trap is

[1] In addition to this work the condensation of ^{85}Rb was also attempted using a second cold atom experiment in Durham [142]. In this setup beam waists of 68 μm were used in the optical trap. Despite initial evaporation proceeding well, this experiment failed to reach degeneracy in ^{85}Rb owing to the experimental geometry.

formed of a single beam it is not possible to use the same technique to align beam 2. Without the ability to switch off the first beam, creating a single beam trap with beam 2 and locating the field zero becomes impossible. In fact, care must be taken to avoid the creation of two separate single beam traps which, in expansion, may look like an increased number of atoms in a single crossed trap.

To circumvent this potential problem the optimum loading position of the crossed trap is found using a pure trap (see section 5.3) where the quadrupole potential is removed. To load the trap the dipole beams are switched on during the RF evaporation stage in the quadrupole trap. Following the evaporation the quadrupole gradient is ramped to 29.3 Gcm^{-1} in 5 s. The atoms are then held for 500 ms before the quadrupole gradient is ramped to zero in 200 ms. After a further 500 ms hold, the atoms are imaged following a 18 ms time of flight expansion.

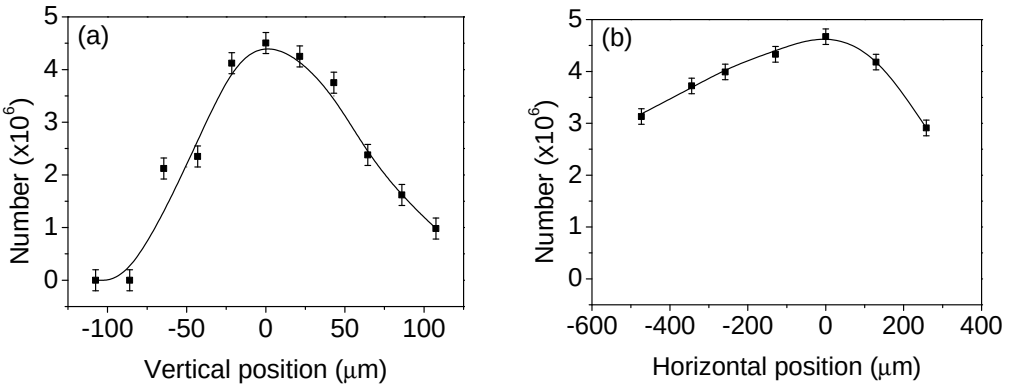

Figure 5.2: Aligning the crossed trap: Atom number in the trap is maximised by scanning the second dipole beam (a) vertically and (b) horizontally using the final delivery mirror. To ensure no atoms are trapped in a single beam dipole trap the quadrupole gradient is switched off. Solid lines are a guide only.

Figure 5.2 shows the trap load dependence on beam 2's alignment in both the horizontal and vertical directions. The second beam can be scanned over only a small range vertically, this being set by the beam waists. The alignment is less sensitive in the horizontal direction due to the experimental geometry and the relative ease of intersection with beam 1.

The alignment of the two beams and the angle between them can be also

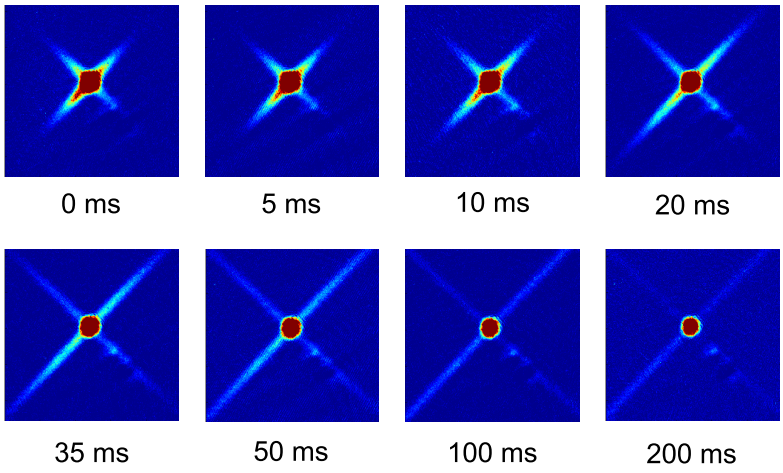

Figure 5.3: Crossed trap from above: False colour images of the crossed trap, viewed from above, after various hold times. With the magnetic confinement of the quadrupole trap removed, atoms escape horizontally along the arms of the beams. After ∼200 ms a small dense cloud of atoms remains, trapped in the intersection of the beams.

be assessed using the vertical imaging. Figure 5.3 shows atoms in the pure crossed trap, viewed from above. Here the quadrupole ramp to zero has been shortened to 10 ms. The atoms are held in the pure trap for some variable length of time (shown) before being imaged after 2 ms time of flight. Imaging in this direction also has the benefit that it allows the evaporation from the trap to be observed (see section 5.3.2).

5.2.3 Trap frequencies

As for the single beam case we obtain the trapping frequencies of this new trap using the parametric heating technique (see section 4.5.2). Blocking the light used for beam 2 it is possible to easily obtain the radial trap frequency associated with beam 1, Fig. 5.4(a). The fundamental and first harmonic observed are in good agreement and, along with other measurements at different trap depths, give a measured trap waist of 136(1) μm.

Measuring the trap frequencies associated with beam 2 alone is obviously not as trivial. Instead we take the same heating measurement, extracting the resonant frequencies shown in Fig. 5.4(b), and use this in conjunction

with the parameters already ascertained from the first measurement of beam 1. This leads to a beam waist of 125(5) μm for beam 2. At full power, 10.9 W, the crossed trap has frequencies of $\omega_{x,y,z} \approx 2\pi \times (195, 167, 254)$ Hz

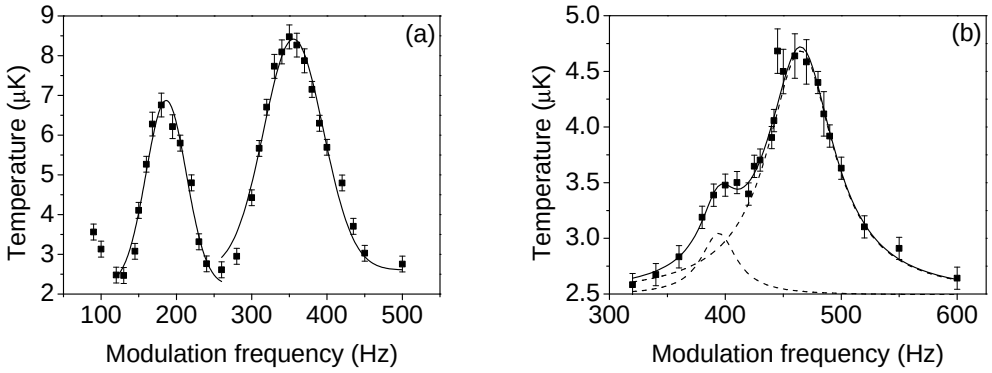

Figure 5.4: Parametric heating to obtain crossed dipole trap frequencies: (a) Fundamental and first harmonic for beam 1 only at full power. (b) Trap frequencies for the crossed trap at a reduced power. Using this and information from (a) the waist of beam 2 can be determined. Solid lines are Lorentzian fits to the data to extract the peak centre but have no physical significance.

5.3 Trap configurations

Considering the contribution of the optical dipole beams, the quadrupole trap and a magnetic bias field it is possible to devise three distinct crossed trap configurations:

(i) The hybrid trap

(ii) The levitated trap

(iii) The pure trap.

The potentials produced in the horizontal and vertical directions for each of these configurations are shown in Fig. 5.5.

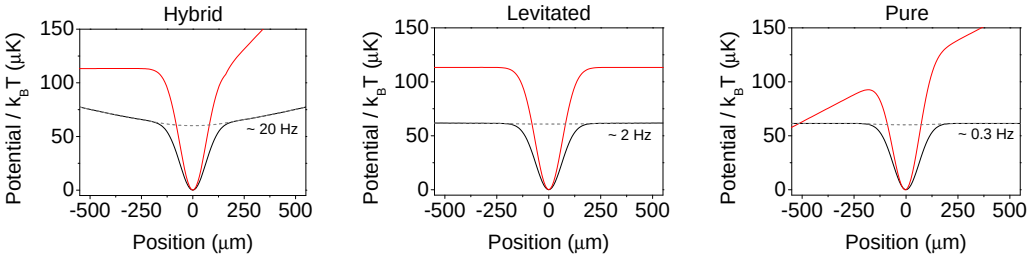

Figure 5.5: Crossed dipole trap configurations: Example horizontal (black) and vertical (red) trapping potentials in each of the three crossed trap configurations. Away from the tightly confining dimple potential produced by the intersection of the two beams is a much weaker trap (dotted lines) produced as a result of the magnetic (hybrid, levitated) or optical confinement (pure) along the horizontal direction of the laser beams.

(i) ***The hybrid trap*:** In the hybrid trap, the crossed trap beams are accompanied by the magnetic quadrupole potential. The magnetic gradient provides levitation of the trapped atoms meaning the full trap depth of the beams can be obtained (see section 5.3.2). The quadrupole potential also has the effect of significantly increasing the trapping volume as atoms are confined not only in the crossed region but also some way along the dipole beams. The quadrupole produces an effective magnetic bowl around the crossed trap, confining the atoms and significantly restricting atom loss horizontally and hence the evaporation in this direction. As a result, evaporation in the hybrid trap primarily occurs in the vertical direction.

(ii) ***The levitated trap*:** A levitated trap is obtained by the application of a bias field to the hybrid configuration. This has the effect of shifting the quadrupole field zero far away from the crossed beams (a distance proportional to the applied field and dependent on the levitation gradient). The result is a trap where the effect of gravity is still compensated, however the magnetic confinement along the dipole beams is severely diminished (see section 4.5.3). Atoms only remain in the crossed region of the beams. In a levitated trap the addition of the dipole beams means the trap depth vertically is approximately double that of the horizontal. Consequently, evaporation in the levitated trap is primarily horizontally, along the length of the dipole beams.

(iii) ***The pure trap*:** A pure trap is created in the absence of any quadrupole potential. Here the atoms are supported against gravity by the crossed dipole beams alone. As a result, much higher beam powers are required to obtain the same trap depth as in the hybrid or levitated cases. A bias field must still be present in the pure trap to define a quantisation axis. Without this, atoms may spin flip to other states. Although this may not necessarily result in their loss from the trap, in order to maintain a spin polarised sample the bias field should be applied. At high powers, the trapping force of the dipole beams is sufficient to overwhelm the effect of gravity. However, as the beam power is decreased the gravitational force becomes more comparable to that of the dipole beams. As a result the trap begins to open up vertically. Evaporation in a pure trap initially occurs horizontally (see Fig 5.3) however, below this threshold a transition to vertical evaporation occurs.

5.3.1 Trap loading

It is interesting to consider if the loading of the crossed dipole trap saturates in any of these three cases or if simply more power in the trap and hence a deeper trap depth ultimately leads to more atoms being confined. We begin by assessing the sensitivity of the loading to the quadrupole ramp time (from 180 Gcm^{-1} to 29.3 Gcm^{-1}). From this we conclude that a ramp time $\geq$ 500 ms is sufficient to maximise the number of atoms transferred into the trap however it is advantageous to use a slow ramp in terms of the cloud temperature. We choose a 5 s ramp time as a compromise between the temperature achieved and the duty cycle of the experiment. With this time established we compare the number of atoms transferred into each dipole trap as a function of the power in beam 1.

From inspection of Fig. 5.6(a) it is clear that none of the traps saturate as the power is increased. Also apparent is the effect of the levitation provided by the quadrupole trap as the pure trap requires almost 1 W more power than the hybrid trap before the trapping force is sufficient to support atoms against gravity. The temperature of the trapped atoms is shown in Fig. 5.6(b) after a 500 ms hold in each trap, which, due to the high elastic collision rate, is sufficient time for the cloud to rethermalise. The high trapping

frequencies result in collision rates of several hundred per second (∼400-600 s^{-1}) and even at low trap powers, collision rates are still on the order of many tens per second. As a general figure of merit, only ∼3 collisions are required for a cloud to rethermalise [85] hence we should be well into this equilibrium regime. As expected, the enhancement of the trap depth due to the quadrupole gradient means both the hybrid and levitated traps support higher temperature clouds, and in general, a larger atom number equates to a higher temperature at the initial loading stage.

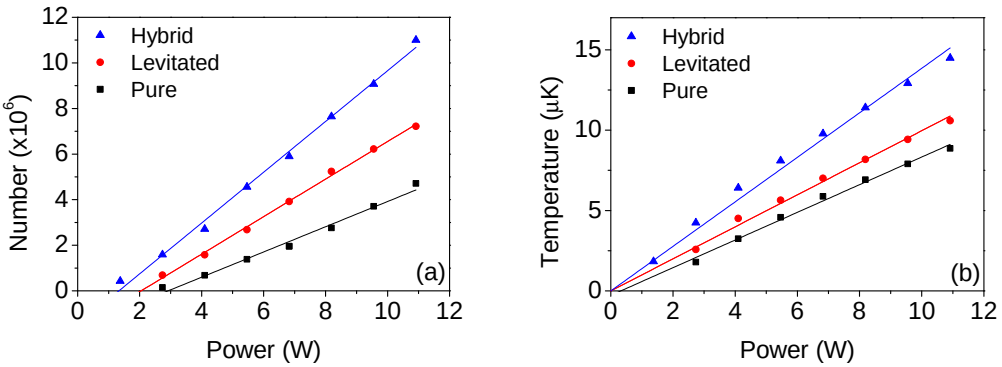

Figure 5.6: Trap loading vs. power: (a) Atom number in the hybrid, levitated and pure crossed dipole traps as a function of beam power. (b) Corresponding temperature of the atoms after a 500 ms hold in the trap. Solid lines are linear fits to the data.

5.3.2 Trap depth and evaporation

Trap depth in all directions

Unlike the single beam case where evaporation is always in the vertical direction, as described in the previous section, this is not the case for the crossed dipole trap. Although it may not be immediately apparent from the shape of lifetime curves, see Fig. 5.7, the evaporation in each of the three trap configurations described in section 5.3 can be very different. By examining the

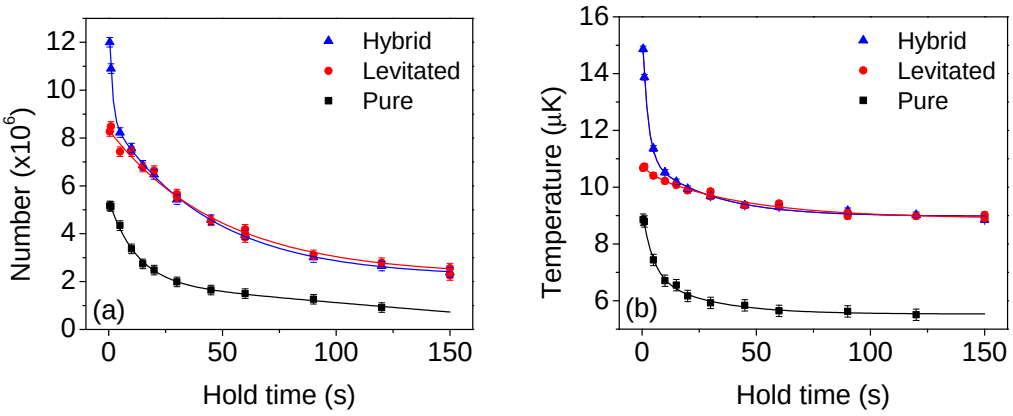

Figure 5.7: Crossed dipole trap lifetime: The number (a) and temperature (b) of atoms held in each of the three crossed dipole trap configurations. From the shape of the decay curves there is no immediately discernible difference between the trap configurations beyond the very early fast atom loss stage.

trap depth in x, y and z it is possible to determine in which direction atoms will preferentially evaporate. As an illustration of this point we calculate the trap depth of the pure trap in three directions for two beam powers. Here the x and y axes are orientated to be along the direction of the two beams. Figure 5.8 shows the trap depths for 10 W and 2 W beam powers, highlighting the transition from horizontal to vertical evaporation. The effect of gravity on the lower power trap is sufficient to cause the trap to sag. This can be seen in Fig 5.8 as a shift in the trap centre in z.

Evaporation parameter

Knowing in which direction atoms will preferentially evaporate (from consideration of the trap potential) it is possible to compare experiment and theory to establish the 'evaporation parameter' for the trap, η. As in section 4.6.2, η is defined as $U_0 = \eta k_B T$ and relates the temperature of cloud, once it reaches equilibrium, to the trap depth.

To determine the equilibrium temperature atoms are loaded into the dipole trap and any bias field required is ramped on. Some evaporation is then carried out to produce a colder, denser sample. This increases the optical depth of the cloud thus improving the signal obtained from absorption imaging. Following the evaporation the dipole trap power is ramped to the value of

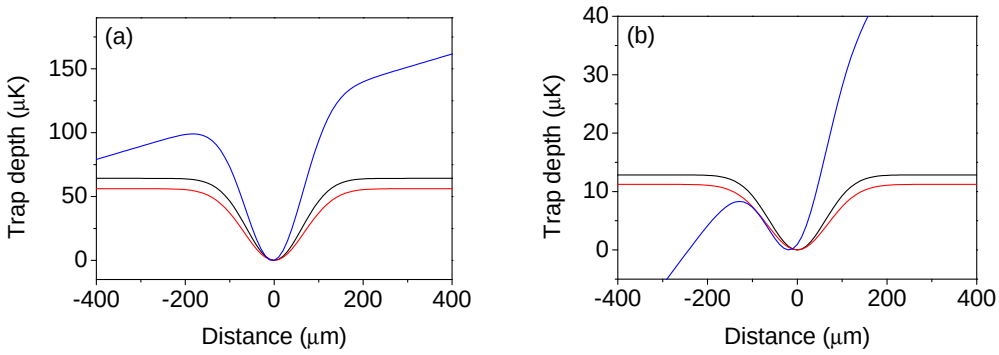

Figure 5.8: Effect of gravity on the trap depth of a pure crossed dipole trap: Shown is the trap depth in the x (black), y (red) and z (blue) directions. (a) At high power (10 W) the total trap depth is set by the horizontal directions. (b) At lower power (2 W) the effect of gravity relative to the dipole force becomes more significant and the trap becomes tilted in z, lowering the trap depth. Atoms now evaporate preferentially in this direction. This weakening in z also causes the trap to sag, shifting slightly in position.

interest and the cloud is held for 20 s to allow it to equilibrate with the trap. This choice of 20 s comes from consideration of lifetime curves for the dipole trap. When initially loaded, there is a rapid loss of atoms before equilibrium in the temperature is reached, see Fig. 5.7. By 20 s we are safely into the region where this rapid loss has ceased and a more representative temperature can be measured.

This measurement of temperature is carried out at several beam powers for each of the three trap configurations. The experimental data are then scaled by η to fit the theoretical prediction of the trap depth (from the known beam waists and powers). The results of both theory and experiment are shown in Fig. 5.9. It is clear from Fig. 5.9 that zero power does not correspond to zero trap depth. This is to be expected for the pure trap, however the discrepancy for the hybrid and levitated traps can be explained by much the same reason. As the magnetic gradient applied is just below that needed to support the atoms against gravity (as this improves evaporation) there is still some small tilt in the trap hence at low power a trap is not necessarily immediately formed.

The data for the hybrid trap is shown in blue. The vertical evaporation

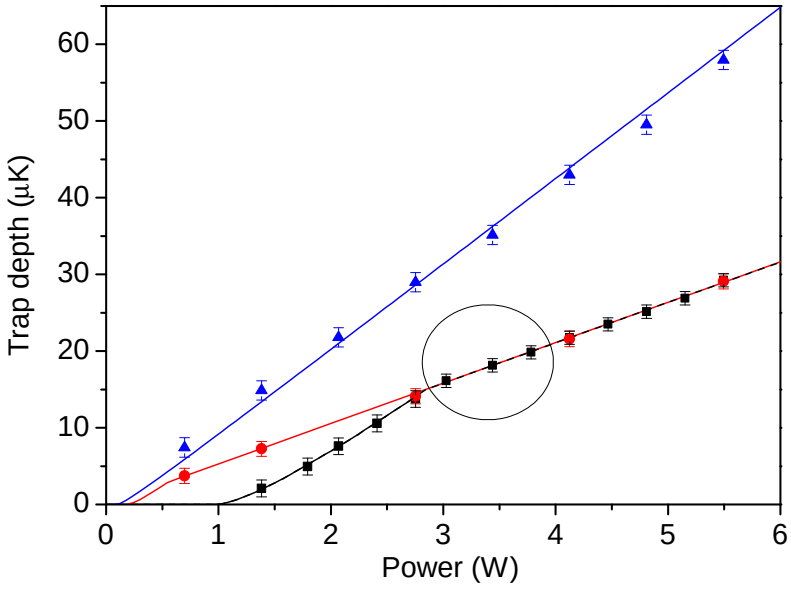

Figure 5.9: Trap depth in the crossed optical dipole trap: Trap depth as a function of the beam power for the hybrid (blue), levitated (red) and pure (black) crossed dipole trap calculated from known beam parameters. Data points are the calculated cloud temperature after a 20 s hold in the trap, scaled by η.

gives a value of η=12.6(5). By comparison, the horizontal evaporation which occurs in the levitated trap, shown in red, returns a much lower value of η=9.8(5). Arguably the most interesting case is that of the pure trap. Here it should be possible to see a transition from horizontal to vertical evaporation. Indeed this is the case and as such we must fit to different η values in the two regions. For the high trap power, horizontal evaporation, η=8.7(5) which increases to η=11.0(5) for the low power, vertical evaporation. For the circled points between the two clearly distinct regions $8.7 < \eta < 11.0$, as one might expect.

From the data it is clear that when evaporation is in the vertical direction a much higher value of η is found. A potential explanation for this difference could be the experimental geometry. η itself can be interpreted as a measure of the heating and evaporation going on in the trap. If the heating in the trap is low, the ratio between the trap depth and cloud temperature, i.e. η, increases and the atoms equilibrate to a lower fraction of the trap depth. If atoms evaporate vertically they are immediately lost from the trap, falling away under the effect of gravity, hence vertical evaporation results in high values for η. Conversely, atoms lost horizontally may still be weakly confined along the dipole beams, oscillating back and forth at some low frequency, potentially back into the crossed region of the trap. This may suggest that, despite the multiple exit routes along the beams, the horizontal evaporation is a somehow less 'clean' form of atom loss hence the lower value of η.

5.4 Bose-Einstein condensation of ^{87}Rb in a crossed dipole trap

With the evaporation in each trap well characterised the next logical step is to attempt the condensation of ^{87}Rb in each distinct configuration. Common to all three condensation routines is the need to load the dipole trap from the magnetic quadrupole trap. The dipole beams are initially switched on during the RF evaporation however, the trap loading is reasonably insensitive to the precise time of beam turn on. To complete the loading of the dipole trap, the quadrupole gradient is ramped from 180 Gcm^{-1} to $\sim$29.3 Gcm^{-1} in 5 s.

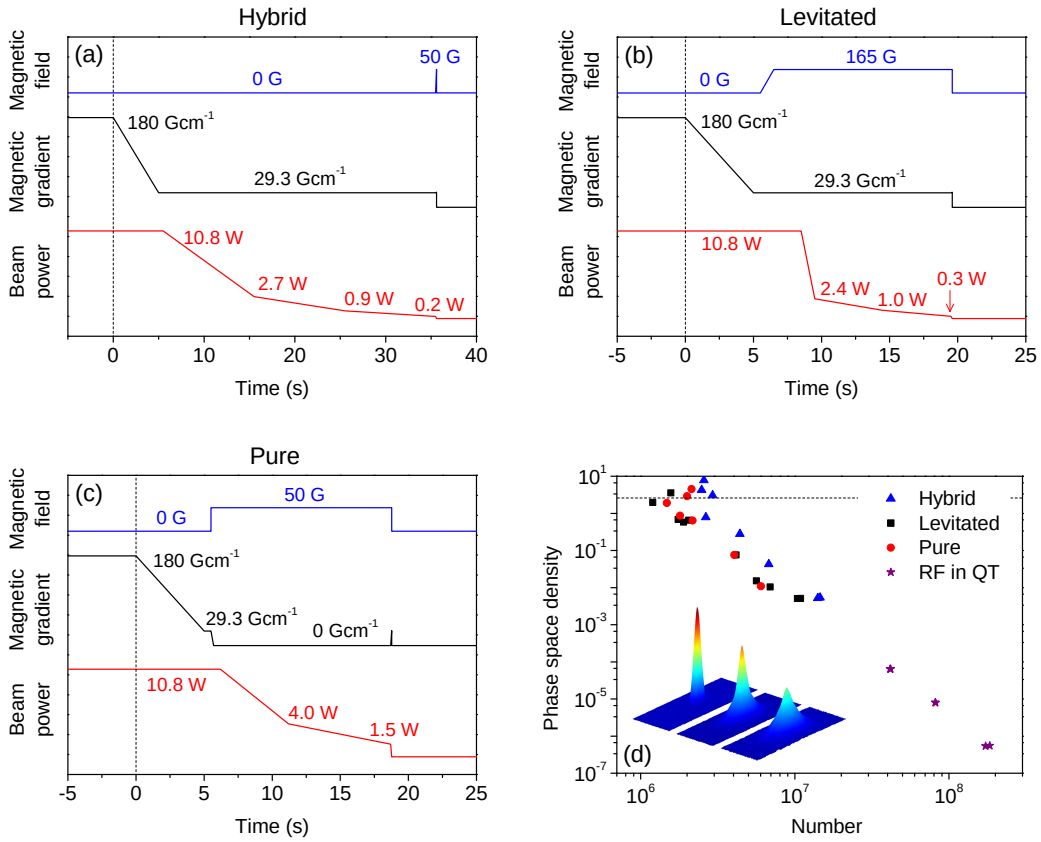

Figure 5.10: ^{87}Rb BEC in a crossed dipole trap: The experimental evaporation routines used to reach ^{87}Rb BEC in the (a) hybrid, (b) levitated and (c) pure crossed dipole trap. The dotted vertical line shows marks the end point of the RF evaporation stage. (d) Evaporation trajectory showing the the number and phase space density evolution as evaporation is carried out, first in the quadrupole trap (purple) and subsequently in the hybrid (blue), levitated (red) or pure (black) crossed dipole traps. The dotted line shows the BEC transition, PSD= 2.61. Inset: False colour images of evaporation to BEC in a hybrid trap.

A 500 ms hold step follows the ramp and allows any atoms not transfered into the dipole trap to fall away. At the end of the RF evaporation stage the atomic sample contains $4.2(1)\times10^{7}$ atoms with a PSD of $6.4(1)\times10^{-5}$. (Here the atom number has been increased by extending the MOT loading time.) Approximately 25-35 % of these atoms are successfully transfered into the optical trap, resulting in a ∼100-fold gain in PSD due to the increased trap frequency and the lower trap depth. From here the route to BEC must be

individually tailored for each trap configuration. Each experimental routine is shown schematically in Fig. 5.10 along with the evolution of both number and PSD as the gas is cooled.

5.4.1 Hybrid trap

The simplest evaporation routine occurs in the hybrid trap. Here a series of 3 linear ramps are employed to cool the sample, approximately quartering the temperature with each step. In each stage the dipole ramp occurs over 10 s, taking the beam power first from 10.8 W to 2.7 W, then down to 0.9 W. The final evaporation stage sees the beam power reduced to 0.2 W, resulting in trap frequencies of $\omega_{x,y,z} = 2\pi \times (39, 35, 45)$ Hz. In this trap the characteristic double distribution is observed with $N = 2.0(5) \times 10^6$. With further evaporation, pure condensates of around $9(1)\times10^5$ atoms can be created. (Note, the short bias field pulse shown in Fig. 5.10 (a) occurs for the duration of the levitated time of flight before imaging.)

5.4.2 Levitated trap

In the levitated trap the application of the bias field leads to a rapid loss of atoms as the trapping volume is dramatically reduced. Therefore, the speed of the bias field switch on must be carefully chosen. Following the same 5 s quadrupole ramp and 500 ms hold, the bias field is ramped to 165 G in 1 s. At this stage, the choice of field is a nominal one and in no way impacts on the scattering properties of the sample. (As we will see in section 6.4, the field chosen and the point at which it is applied will be much more crucial in the evaporation of ^{85}Rb.) The atoms are then held for 3 s to allow rethermalisation, causing a slight increase in PSD. Again, 3 linear ramps of the dipole power are needed to reach BEC. The first reduces the power from 10.8 W to 2.4 W in just 1 s. The second from 2.4 W to 1.0 W happens over 5 s, as does the final ramp to 0.3 W.

The final power of the levitated trap results in trap frequencies of $\omega_{x,y,z} = 2\pi \times (31, 27, 37)$ Hz. The onset of BEC is observed with $N = 1.2(3) \times 10^6$, however pure condensate of only around $N = 6(1) \times 10^5$ are produced.

5.4.3 Pure trap

In the hybrid and levitated traps the reduction in power in each evaporation stage was roughly comparable. However, the nature of the pure trap means that the evaporation ramps here can be very different. Without the quadrupole gradient to levitate the atoms, the dipole trap depth is severely diminished. As a result, to obtain a similar trap depth, relative to the first two traps, a much greater laser beam power is required.

Following the 500 ms hold at 29.3 Gcm^{-1} the gradient is ramped away completely in 200 ms. Importantly the bias field is switched on during this step (to ∼50 G) to maintain a well defined quantisation axis for the atoms. Following the ramp, 500 ms of equilibration time is allowed before the first of the dipole ramps, from 10.8 W to 4.0 W in 5s, is applied. Only one further evaporation ramp is required to reach degeneracy, reducing the dipole power to 1.5 W in 7.5 s. This power level leads to much higher final trap frequencies of $\omega_{x,y,z} = 2\pi \times (74, 63, 87)$ Hz. Consequently the collision rate in the trap is significantly higher and hence the time needed to reach BEC in the pure trap is considerably shorter than in the hybrid trap, as can be seen in Fig. 5.10 (c).

In the pure trap the two-component signature signalling the onset of BEC is observed with $N = 1.6(3) \times 10^6$ atoms. As with the levitated trap the size of the pure condensate is again smaller than in the hybrid case, generally only reaching $N = 6(1) \times 10^5$.

5.5 BEC in a 1D optical lattice

It is potentially of interest to explore the possibility of using the IPG fibre laser to produce an optical lattice. Future experiments, for example the study of Bloch oscillations [141] close to a surface, call for the use of optical lattices and hence a brief foray into the world of lattice physics is arguably of some merit, particularly as the crossed trap presents just such an opportunity.

An optical lattice is formed as the result of interference between two laser beams. Importantly, some component of the beams' polarisation must be

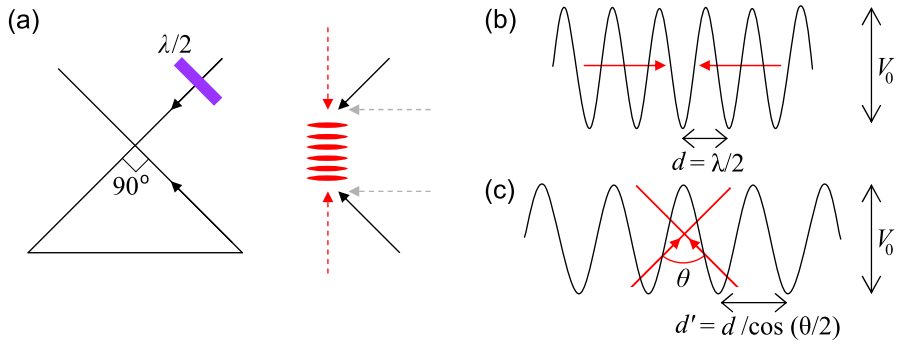

Figure 5.11: Forming an optical lattice: a) Schematic of the crossed dipole trap with the addition of a half waveplate to control the beam polarisation. The two dipole beams can be resolved into orthogonal components (dotted lines) revealing both co- and counterpropagating beams. b) A lattice created by two counterpropagating beams. c) The effect of the relative beam angle on the lattice spacing.

parallel for the lattice to form. In general, our crossed beam trap does not meet this criteria. In order to minimise reflections from the glass cell, the beam polarisation is set to be horizontal. This, coupled with the 90° intersection of the beams means that the polarisations of beam 1 and beam 2 are entirely perpendicular. To circumvent this problem a half waveplate, shown in Fig 5.11, is used to add a small component of vertical polarisation into the dipole beams, at the cost of a minor drop in power at the trap. In this way we are able to create a lattice and explore its effect on a Bose-Einstein condensate. In the next section we will address some of the basic theory underlying optical lattices, however, for a comprehensive review of lattice physics see [143].

5.5.1 1D optical lattices

In the simplest case, the two beams forming the lattice are identical and counterpropagating, overlapping fully as shown in Fig. 5.11(b). In this simple case the interference pattern created has a lattice spacing of $d = \lambda/2$. In this instance the potential seen by the atoms is given by

$$V(x) = V_0 \cos^2(\pi x/d), \tag{5.1}$$

where V_0 is the lattice depth. This depth is defined as the difference in potential from peak to trough and is typically expressed in units of the recoil energy

$$E_R = \frac{\hbar^2 k^2}{2m} = \frac{\hbar^2 \pi^2}{2md^2}. \tag{5.2}$$

Using a power series expansion around the minimum of the potential, i.e. $x = d/2$, it is possible to derive the harmonic oscillation frequency of an atom trapped in a lattice. Starting from Eq. (5.1) we expand around $x = d/2 + \Delta x$. This yields,

$$V(x) \approx \frac{V_0 \pi^2 \Delta x^2}{d^2}. \tag{5.3}$$

This can be equated to the potential of an atom in a harmonic trap,

$$\frac{V_0 \pi^2 \Delta x^2}{d^2} = \frac{1}{2} m\omega^2 \Delta x^2, \tag{5.4}$$

thus we obtain,

$$\omega_{\text{lattice}} = \frac{\pi}{d}\sqrt{\frac{2V_0}{m}}. \tag{5.5}$$

Considering the typical lattice spacings achievable, it becomes immediately apparent that even with modest laser powers, it is possible to generate trap frequencies of a few kHz with relative ease when using optical lattices.

The lattice potential can be manipulated in a number of ways, for example by the wavelength of the light used or the power of the laser beam. The angle of intersection of the beams also plays a key role in the lattice formed, changing the resultant lattice spacing. Choosing an angle $\theta < 180°$, as shown in Fig. 5.11(c), increases the spacing between neighbouring lattice sites. As a result, the usual spacing, $d = \lambda/2$, becomes,

$$d(\theta) = \frac{d}{\cos(\theta/2)}. \tag{5.6}$$

Of course adding more beams opens up the possibility to create higher dimensional lattices. However, we will not consider this here. Our primary aim is to determine whether the IPG fibre laser is suitable for the production of optical lattices and if it is possible to observe qualitative features associated with the formation of a Bose-Einstein condensate in a lattice.

5.5.2 Creating a BEC in a lattice

Producing a BEC in a lattice rather than mere ultracold atoms has a number of advantages [143]; the lower temperatures and higher densities offered by the condensate means the lowest lying energy levels of the lattice will be populated without the need for further cooling. The increased filling factor of the lattice, again due to the high density, creates an approximately fully occupied 'crystal', ideal for condensed matter simulations. In addition, interatomic interactions are generally more appreciable for BECs in lattices compared to ultracold atoms in the same lattice. As a result more diverse physics applies in this system. The lattice's effect on the condensate is also important. Its presence introduces a new length scale, much smaller than the condensate size, along with a periodicity previously absent from the trap.

Bose-Einstein condensates in optical lattices can be prepared in one of two ways. Either the BEC is first created in some conventional magnetic or optical trap and then adiabatically transfered into the optical lattice or the condensation process occurs in the lattice itself. As we have no means of creating a separate, independent lattice potential, we must use the latter method.

We begin by loading the hybrid crossed dipole trap as described in section 5.4. After a 500 ms hold, we apply a series of 3 ramps of the dipole laser power: ramp 1: 10.6 W to 3.8 W in 10 s, ramp 2: 3.8 W to 0.8 W in 15s, ramp 3: 0.8 W to 0.15 W in 10s. Following this, the atoms are held for a further 2 s before BEC is achieved.

5.5.3 Signature of condensation

To confirm the creation of a Bose-Einstein condensate in the lattice we must image the atoms vertically after their release from the trap[2]. In doing so one is able to observe the momentum distribution of the atoms. In a harmonic trap, a condensate has a Gaussian momentum distribution in the limit of weak interactions and a Thomas-Fermi distribution when the interactions dominate over the kinetic energy. In contrast, a condensate in a lattice has

[2]In general we choose ∼100 ms levitated time of flight.

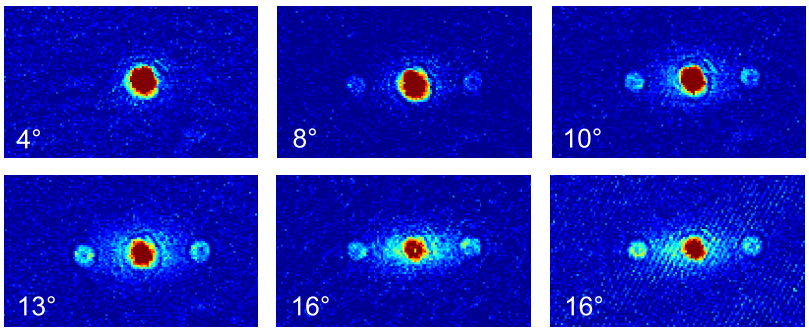

Figure 5.12: Emergence of an optical lattice: Vertical images of an ^{87}Rb BEC formed in an optical lattice as a function of polarisation angle from the horizontal.

additional momentum components in multiples of $2\hbar k_L$ (where $k_L = 2\pi/\lambda$) [143], the weighting of these components depending on the lattice depth. If the lattice is deep, in the 'tightly binding' limit, the condensate can be thought of as many wavefunctions, each occupying their own lattice site. These then expand independently once the lattice is switched off, overlapping and interfering. This interference pattern then corresponds to the Fourier transform of the initial condensate.

Figure 5.12 shows the emergence of a lattice as the polarization of the dipole beams is rotated. The angle stated is the direction of polarisation of the beam, relative to horizontal. As more vertically polarized light is added, the lattice becomes deeper and the secondary momentum peaks become more visible.

Because of the necessity to image vertically (due to the horizontal lattice formed in the same direction as the horizontal imaging beam) a levitated time of flight is required to keep the atoms in focus with the imaging optics. The quadrupole trap, along with a bias field, is used to provide this levitation. However, an unfortunate side effect is a weak horizontal trapping produced by the combination of magnetic fields. We can observe this effect by imaging the condensate, released from the same trap, and varying the time of flight. A collection of such images are shown in Fig. 5.13. Fitting the evolution of the side peak position with time does however allow this trapping frequency (∼2 Hz) to be determined which we find to be in agreement

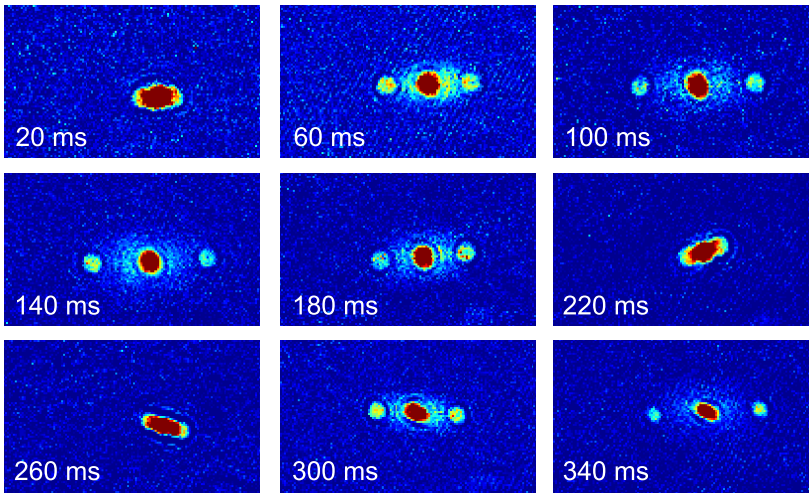

Figure 5.13: Momentum peak evolution with time: In order to levitate the atoms in time of flight both the quadrupole trap and a bias field are left on during the expansion from the lattice. This results in a weak axial trapping causing the observed position of the $2\hbar k$ momentum peaks to oscillate in time.

with the calculated value.

5.5.4 Kapitza-Dirac scattering

Calibration of the lattice depth can be done in a number of ways. Although it is possible to calculate the lattice depth (V_0) from knowledge of the atomic polarizability and the lattice beam parameters, it can be difficult to measure the latter accurately. Instead one can use the response of the atoms to various perturbations of the lattice to recover information about V_0.

For a static lattice, calibration examples include:

- **Parametric heating leading to atom loss:** By modulating the lattice light at a frequency twice that of the harmonic trapping of the wells, the atoms contained within can be parametrically heated [144]. This leads to atom loss from the trap and a net heating of the remaining cloud. The trap depth can then be calculated according to Eq. (5.5).
- **Expansion from the lattice:** After loading the lattice adiabatically

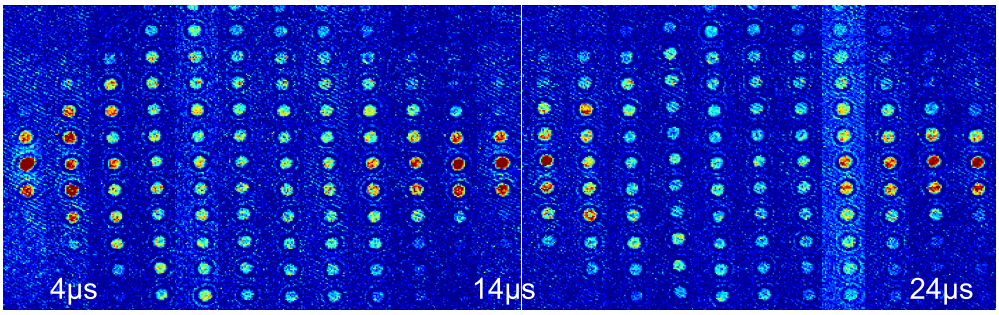

Figure 5.14: Kapitza-Dirac scattering: Pulsing the lattice on at an increased power for a time Δt transfers atoms into different momentum states, the population of which oscillates with time. Images shown are for $\Delta t = 3$ μs to $\Delta t = 25$ μs, increasing (from left to right) in 1 μs steps.

the light is abruptly turned off. As the atoms expand and interfere the diffraction pattern observed is the product of a series of momentum peaks and a Gaussian envelope, the width of which reflects the distribution of local wavepackets in the lattice. For deep lattices the lattice depth is calculated from the relative population $P_{\pm 1}$ of the 0 and $\pm 2\hbar k_L$ momentum peaks according to

$$s = \frac{V_0}{E_R} = \frac{16}{[\ln(P_{\pm 1})]^2} P_{\pm 1}^{1/4}. \tag{5.7}$$

- **Kapitza-Dirac scattering:** (Also known as Raman-Nath diffraction) By pulsing on the lattice for a short time $\Delta t \ll 1/\omega$ the resulting diffraction pattern can be used to determine V_0 using the relative population of the 0 and $\pm 2\hbar k_L$ bands [145].

The most visually spectacular result arises from the Kapitza-Dirac scattering method. By rapidly pulsing on the lattice, atoms populate a number of different Bloch states. Whilst the lattice remains switched on the population of these states evolves in time until the lattice is switched off again and the atoms are released. As a consequence, the observed population of the different momentum peaks oscillates as a function of the pulse duration Δt. If only bands 0 and $2\hbar k_L$ are populated (odd bands remain unpopulated as a result of symmetry arguments) the variation in time is sinusoidal. Fitting the period of this population cycle allows V_0 to be then be extracted.

Examples of typical population transfer are shown in Fig. 5.14. Here a BEC is created in the lattice (as described earlier) by reducing the power in the lattice beams to evaporatively cool the atoms. Once BEC is reached the lattice light is then pulsed on at a much higher power for some variable time Δt before the atoms are released from the trap. After 60 ms of expansion the atoms are destructively imaged.

5.6 Summary

In this chapter we have characterised the evaporation of ^{87}Rb in a crossed optical dipole trap. Using three distinct trap configurations we are able to control the evaporation surface and from here, go on to produce ^{87}Rb condensates in all cases. By changing the polarization of the trapping light we then show that it is possible to create a 1D optical lattice using the IPG fibre laser in this crossed trap setup. We demonstrate the formation of a Bose-Einstein condensate in the lattice and observe the experimental signatures in time of flight.

From this point, the next step is to load ^{85}Rb into the crossed trap and explore the evaporation trajectory in both the hybrid and levitated cases. Here the bias field applied will have a significant impact on the scattering properties of the atoms and hence will determine the efficiency of the evaporation.

Chapter 6

Bose-Einstein condensation of ^{85}Rb

6.1 Introduction

In this chapter we explore the nature of the elastic and inelastic scattering properties of ^{85}Rb. We then go on to describe a simple method for the creation of Bose-Einstein condensates of ^{85}Rb by direct evaporation in a crossed optical dipole trap. The independent control of the trap frequencies and magnetic bias field afforded by the trapping scheme permits full control of the trapped atomic sample, enabling the collision parameters to be easily manipulated to achieve efficient evaporation in the vicinity of the 155 G Feshbach resonance. We produce nearly pure condensates of up to 4×10^4 atoms and demonstrate the tunable nature of the atomic interactions. Finally, we review previous work on the collapse phenomenon of attractive condensates and demonstrate the same effect using the ^{85}Rb BEC produced in the crossed dipole trap.

6.2 Why use ^{85}Rb?

The use of magnetically tunable Feshbach resonances [146] to control the interaction between atoms is now commonplace in many ultracold atomic gas experiments. The ability to precisely tune the s-wave scattering length, a_s,

near a broad resonance has resulted in many exciting breakthroughs in the study of atomic Bose-Einstein condensates (BECs) and degenerate Fermi gases [14, 147]. At the same time, Feshbach resonances have found applications in the coherent association of ultracold molecules [14, 148], bringing quantum degenerate samples of ground state molecules within reach [149, 150]. Although essentially all single-species alkali-metal atoms exhibit some sort of Feshbach spectrum, broad resonances suitable for tuning the scattering length are generally less accessible. For example, the broadest resonance in ^{87}Rb, the workhorse of many quantum gas experiments, is at a field of 1007 G and just 0.2 G wide [151]. In contrast, a resonance exists for ^{85}Rb atoms in the $F = 2$, $m_F = -2$ state at 155 G which is 10.7 G wide [152, 37] yielding a variation of the scattering length with magnetic field of $\sim 40\ a_0\ \mathrm{G}^{-1}$ in the vicinity of $a_s = 0$. This has already been used successfully to precisely tune the atomic interactions in a BEC [30, 35, 34, 7, 153, 38]. Despite this, ^{85}Rb has been notably underused in quantum gas experiments owing to its perceived reputation as a difficult species to cool to degeneracy.

The difficulties associated with attempting to evaporatively cool ^{85}Rb are well documented [30, 154, 155]. The elastic collision rate in samples trapped directly from a magneto-optical trap (MOT) is severely suppressed due to an unfortunately placed zero in the s-wave scattering cross section [154]. Additionally, the two- and three-body inelastic collision rates in ultracold samples are unusually high and vary strongly in the vicinity of the Feshbach resonance [155]. Nevertheless, carefully optimized evaporation in a weak Ioffe-Pritchard magnetic trap produced stable condensates of $\sim 10^4$ atoms [30]. However, with the development of optical trapping, the modern evaporator is equipped with a broader array of tools than her predecessor, allowing her to navigate the potential pitfalls associated with ^{85}Rb with greater ease. For example, recent experiments [33, 31] have almost circumvented these problems entirely by employing ^{87}Rb to sympathetically cool low density samples of ^{85}Rb, yielding condensates of up to 8×10^4 atoms [33], at the expense of added experimental complexity.

6.3 Scattering properties

In this section we consider the specifics of both elastic and inelastic scattering in an ultracold gas of ^{85}Rb atoms. It is important to strike a fine balance between the two mechanisms if efficient evaporation is to be achieved. We discuss the nature of the mechanisms and importantly how they vary in the vicinity of the 155 G Feshbach resonance present in collisions between atoms in the $F = 2, m_F = -2$ state of ^{85}Rb.

6.3.1 Elastic scattering

The success of evaporative cooling is largely dependent on the elastic collisions responsible for rethermalisation of the cloud. The elastic collision rate is given by

$$\Gamma_{\rm el} = \langle n \rangle \sigma_{\rm el} \langle v_{\rm rel} \rangle, \tag{6.1}$$

where $\langle n \rangle$ is the mean density, $\sigma_{\rm el}$ the scattering cross section and $\langle v_{\rm rel} \rangle$ the mean relative velocity. For a harmonically trapped gas the density and velocity are then defined as,

$$\langle n \rangle = \frac{1}{N} \int n(\mathbf{r})^2 d^3r = \frac{N \omega_\rho^2 \omega_z}{8} \left(\frac{m}{\pi k_{\rm B} T} \right)^{3/2}, \tag{6.2}$$

and

$$\langle v \rangle = \left(\frac{16 k_{\rm B} T}{m \pi} \right)^{1/2}. \tag{6.3}$$

However, the exact form of the $\sigma_{\rm el}$ depends very much on the collision energy (and therefore the temperature) of the atoms and, as this decreases, on the scattering length of the atomic sample. For this reason Eq. (6.1) is sometimes expressed as $\Gamma_{\rm el} = \langle n \rangle \langle \sigma_{\rm el} v_{\rm rel} \rangle$.

High temperature collisions

In the limit of 'high' temperature, i.e. 100s of μK, the scattering cross-section of ^{85}Rb varies rapidly as can be seen in Fig. 6.1 [156]. The minimum[1]

[1]This is a Ramsauer-Townsend [157, 158] type minimum associated with low energy collisions.

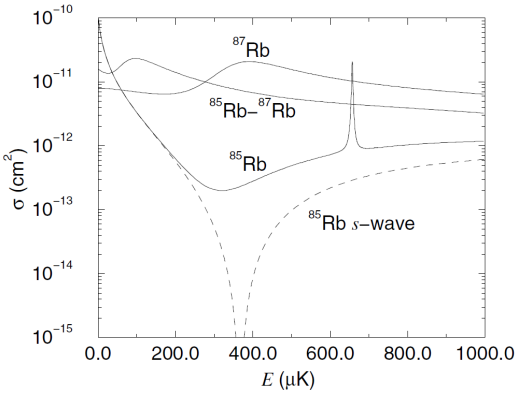

Figure 6.1: Total elastic cross-section for rubidium collisions as a function of collision energy: Figure taken from [156]

in the s-wave collisions at 375 μK causes the slow rethermalisation of atoms in the magnetic trap (these collisions happen at around 6-8 $k_{\mathrm{B}}T$) during the RF evaporation stages and makes conventional techniques of adiabatic compression [159] ineffective.

One of the most striking features of Fig. 6.1 is the contrast between ^{85}Rb and ^{87}Rb. Not only is the cross-section for ^{87}Rb almost flat over the entire temperature range shown but is around two orders of magnitude larger than that of ^{85}Rb.

Low temperature collisions

In its most general form, the elastic scattering cross-section is given by

$$\sigma_{\mathrm{el}} = \frac{8\pi a_s^2}{(1 - r_e k^2 a_s/2)^2 + k^2 a_s^2}. \tag{6.4}$$

Here a_s is the scattering length, r_e the effective range and the wavevector, k, is defined as

$$k = \left(\frac{16 m^* k_{\mathrm{B}} T}{\pi \hbar^2}\right)^{1/2}, \tag{6.5}$$

taking into account the temperature, T and reduced mass, m^*. This full expression describes scattering with no inelastic processes but with an effective range correction [160, 161], accounting for the non-zero temperature effect on the scattering length. This is given by

$$r_e = C\overline{a}\left(1 - 2\frac{\overline{a}}{a_s} + 2\left(\frac{\overline{a}}{a_s}\right)^2\right), \tag{6.6}$$

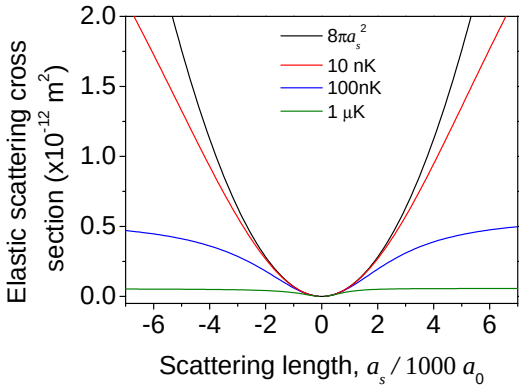

Figure 6.2: Elastic scattering cross-section: Dependence of Eq. (6.4) on scattering length as a function of temperature. Also shown is the simplification $\sigma_{\rm el} = 8\pi a_s^2$.

where $C = \frac{1}{3}\Gamma(\frac{1}{4})^2\Gamma(\frac{3}{4})^{-2}$ and $\overline{a} = 2^{3/4}\Gamma(\frac{3}{4})/\Gamma(\frac{1}{4})(\mu C_6)^{1/4}$.

If the deBroglie wavelength of the atom is much larger than the geometric mean of the scattering length and the effective range, then the elastic cross section reduces to

$$\sigma_{\rm el} = \frac{8\pi a_s^2}{1 + k^2 a_s^2}, \tag{6.7}$$

a more widely used form owing to its relative simplicity. In this case the scattering is determined by a_s^2 and hence is independent of the sign of the scattering length. In the unitarity limit, where $ka_s \gg 1$ (or equivalently $a_s \gg \lambda$), $\sigma_{\rm el} = 8\pi/k^2$ whereas in the ultracold limit, $ka_s \ll 1$, the scattering rate reduces down to $\sigma_{\rm el} = 8\pi a_s^2$. In this ultracold case the atoms scatter like hard spheres.

It is interesting to contrast these cases and to examine at what sort of temperatures the additional terms become non-negligible. Figure 6.2 shows the breakdown on the simple $\sigma_{\rm el} = 8\pi a_s^2$ approximation when contrasted to the more complex Eq. (6.4) at various temperatures. As we expect, the simplification is most valid in the limit of low temperature and small scattering length. For low T and small a_s we find that there is little deviation between the full effective range corrected form of the scattering, Eq. (6.4) and $\sigma_{\rm el} = 8\pi a_s^2$. However, once we increase the temperature into the μK range,

the discrepancy between Eq. (6.4), Eq. (6.7) and the simple $\sigma_{\mathrm{el}} = 8\pi a_s^2$ becomes more dramatic as can be seen in Fig. 6.3.

Figure 6.3 shows the three cases at both 10 μK and 100 μK. Not only is there a rapid departure from the full effective range calculation with temperature but also with scattering length. Thus we conclude, that at large scattering lengths, the effective range contribution is significant and cannot be neglected.

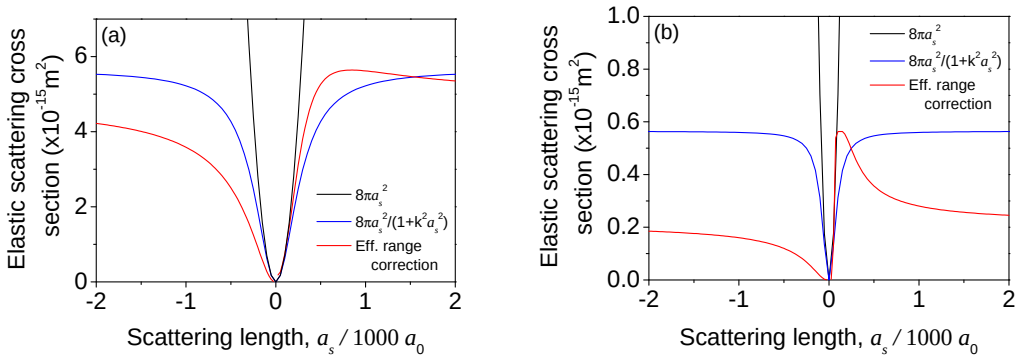

Figure 6.3: Effective range contribution: The deviation of approximations to the elastic scattering cross-section at temperatures of (a) 10 μK and (b) 100 μK.

6.3.2 Tuning atomic interactions: Feshbach resonances

The use of magnetically tunable Feshbach resonances [14] to control the interaction between atoms is now commonplace in many ultracold atomic gas experiments. These resonances allow the value of the s-wave scattering length, a_s, to be changed over many orders of magnitude in both the positive and negative domain by simply changing the magnetic field. In the case of broad resonances where $\Delta \gtrsim 1$ G, the change of scattering length with field around the zero crossing makes precise control over the atomic scattering properties possible. For Bose-Einstein condensation of some species (e.g. ^{85}Rb, ^{7}Li) this is of particular importance as it allows the creation of stable condensates with repulsive interactions ($a_s > 0$) despite a negative background scattering length away from the resonance.

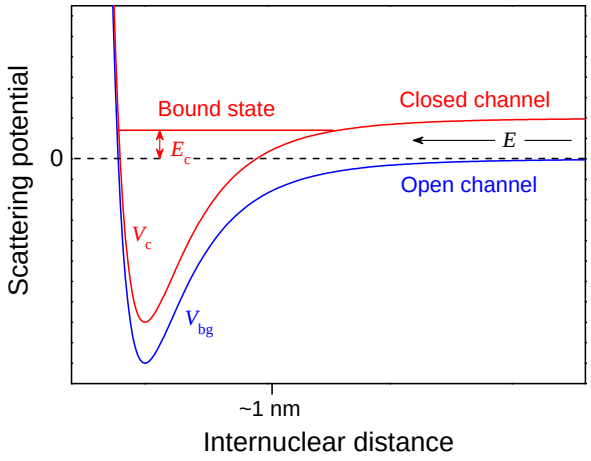

Figure 6.4: Feshbach resonances: A two channel model of a Feshbach resonance. A resonance occurs when two atoms colliding with energy E resonantly couple to a bound state of the closed channel.

Feshbach resonances arise when a resonant coupling occurs between the collisional open and closed channels of an atomic system. For large internuclear distances, the interaction between two atoms can be described by the background potential, V_{bg}. If two free atoms approach, colliding with low energy, E, this potential represents the open or entrance channel for the collision. In contrast, closed channels (described by V_{c}) are able to support molecular bound states. A Feshbach resonance occurs when the energy of a bound molecular state in the closed channel, E_{c}, approaches that of the open channel. In this instance a strong mixing between the two channels can occur even in the presence of only weak coupling. By changing the magnetic field applied this energy difference can be tuned if the magnetic moments of the two channels differ thus the scattering properties of the atomic sample can be modified.

The ability to precisely tune the atomic scattering properties of a trapped sample using a Feshbach resonance is of huge importance and makes many BEC experiments possible. Their application has led not only to the realisation of bright solitary matter-waves [5, 6, 7] but also the formation of molecular BECs [162, 163, 164] and the exploration of the BEC-BCS crossover [165, 166]. Using a resonance to increase the scattering length to large positive values in condensates with high N also allows one to probe beyond

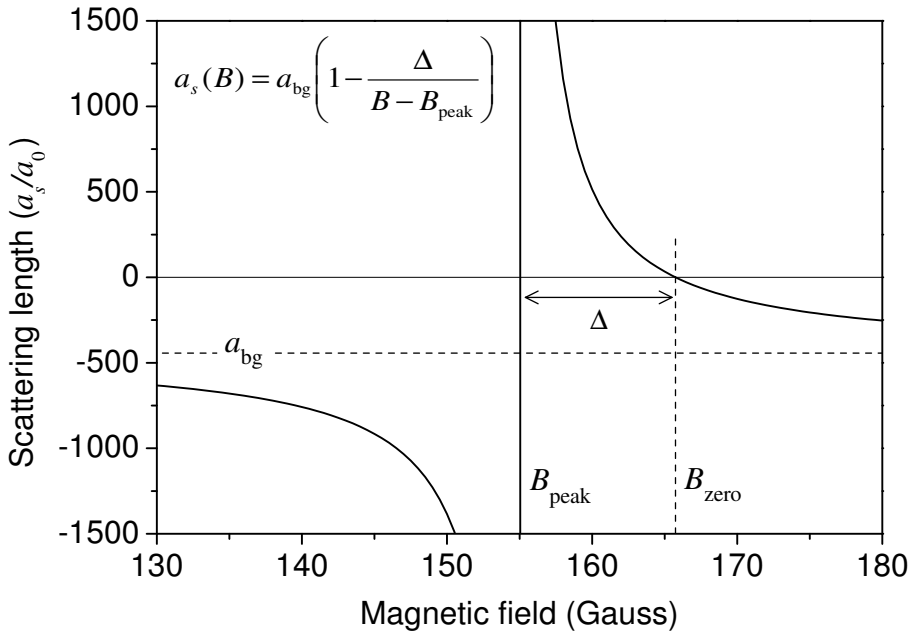

Figure 6.5: ^{85}Rb $F = 2, m_F = -2$ Feshbach resonance: Positioned at B_{peak}=155.041(18) G the broad, Δ = 10.71(2) G, resonance of the $F = 2, m_F = -2$ state of ^{85}Rb gives tuning of the scattering length on the order of $\sim 40\ a_0\text{G}^{-1}$ close to the zero crossing at B_{zero}=165.85(5) G. Away from the resonance the background scattering length is $a_{\text{bg}} = -443(3)\ a_0$. Resonance data taken from [37].

mean-field effects where the validity condition of the GPE, $n|a_s|^3 \ll 1$ begins to break down [167, 153]. Alternatively, tuning the scattering length close to zero reduces the decoherence usually observed in Bloch oscillations, extending observation times from a few to more than 20,000 Bloch oscillation periods [168].

^{85}Rb $F = 2, m_F = -2$ state Feshbach resonance at 155 G

Following work using two-color photoassociation to measure the last 20 GHz of bound levels in the lowest molecular singlet and triplet states of ^{85}Rb, (thus allowing a complete set of Rb_2 interaction parameters to be precisely determined [169]) three magnetic Feshbach resonances in collisions between

atoms in the $F = 2, m_F = -2$ state of ^{85}Rb were predicted by Heinzen and co-workers [170]. Of these three, two were predicted to be broad, lying at at 142 G and 524 G with the third, a much narrower feature, at 198 G. The same group later went on to observe one of the broad resonances [171] pinpointing its position as 164(7) G. Subsequent work by Roberts *et al.* improved this measurement, initially measuring the position as 155.2(4) G [152], later revised to 154.9(4) G [172].

Although many more resonance have now been theoretically predicted in the $|2, -2\rangle$ state [173], most work still focuses on the 155 G resonance. The magnetic field dependence of the scattering length close to a Feshbach resonance is given by

$$a_s = a_{\rm bg}\left(1 - \frac{\Delta}{B - B_{\rm peak}}\right). \tag{6.8}$$

Most recently the use of very high precision bound-state spectroscopy [37] to measure the 155 G feature returned values of $a_{\rm bg} = -443(3)\ a_0$, $\Delta = 10.71(2)$ G and $B_{\rm peak}$ =155.041(18) G. Here magnetic field pulses were used to induce coherent atom-molecule oscillations, which could in turn be used to calculate the molecular binding energy, $E_b = -\hbar^2/(ma_s^2)$. The frequency of these oscillations ($E_b = h\nu$) was mapped out as a function of magnetic field and compared to coupled channel calculations. Using Eq. (6.8) to describe the variation of the scattering length close to the resonance, the oscillation frequency can be expressed as [174],

$$\nu = \frac{\hbar}{2\pi m a_{\rm bg}^2}\frac{(B - B_{\rm peak})^2}{(B - B_{\rm zero})^2}. \tag{6.9}$$

This, when used along with measurements of $a_s = 0$ from collapse studies [35], meant that the scattering length and binding energy could be completely characterised close to the Feshbach resonance with far greater precision than had been seen previously.

This resonance is shown in Fig. 6.5 and is central to the work carried out in this thesis. By working close to the feature one is able to manipulate the value of a_s over many orders of magnitude, allowing direct control over the scattering properties of the atomic sample. Far from the resonance the large negative background scattering length of atoms in the $|2, -2\rangle$ state makes it impossible to form stable condensates. Close to the zero crossing of the

resonance, the variation of the scattering length can be approximated by differentiation of Eq. (6.8),

$$\frac{da_s}{dB} = \frac{a_{\rm bg}\Delta}{(B_{\rm peak} - B)^2}. \tag{6.10}$$

At $B = B_{\rm zero} = B_{\rm peak} + \Delta$, Eq. (6.10) becomes

$$\frac{da_s}{dB} \approx \frac{a_{\rm bg}}{\Delta}. \tag{6.11}$$

For the 155 G resonance the scattering length therefore varies at a rate of $\sim$ 40 $a_0\mathrm{G}^{-1}$ near to the zero crossing in the scattering length. (For comparison, the broad resonance at $\sim$20 G in the $F = 3, m_F = 3$ state of Cs has a magnetic field dependence of $\sim$ 66 $a_0\mathrm{G}^{-1}$ and has also been used to reach BEC [175].)

Elastic scattering close to the Feshbach resonance

Using the variation in scattering length as a function of magnetic field described by Eq. (6.8) along with Eq. (6.4) one can calculate how the elastic scattering cross-section varies close to the Feshbach resonance. The full calculation including the effective range correction is shown in Fig 6.6 for three different temperatures. From Fig. 6.6 it is clear that as the temperature falls the elastic scattering cross-section is enhanced and can be varied precisely using the magnetic field.

However, it is also important to consider inelastic collisions which also vary over many orders of magnitude close to the resonance [155]. A delicate balance must be struck between 'good' and 'bad' collisions if evaporation is to proceed efficiently.

6.3.3 Inelastic scattering

Inelastic loss mechanisms result in not only a decrease in the number of trapped atoms but can also cause heating of the sample. In the case of density dependent processes, atoms are preferentially lost from the cold, dense centre of the cloud leading to 'anti-evaporation'.

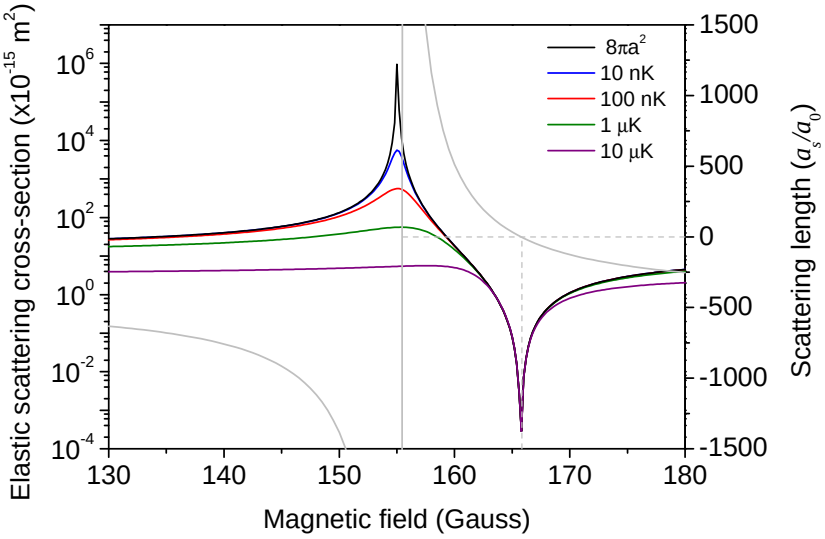

Figure 6.6: Elastic scattering cross-section close to the 155 G Feshbach resonance: Full effective range calculation of $\sigma_{\rm el}$ for cloud temperatures $T =$ 10 nK, 100 nK, 1 μK and 10 μK along with the simplified $\sigma = 8\pi a_s^2$ calculation. Shown in light grey is the 155 G resonance. Dotted lines show the position of the zero crossing in the s-wave scattering length.

Background loss

Background loss results from collisions of trapped atoms with surrounding room temperature atoms and molecules present due to the imperfect nature of the vacuum. However, atoms lost in this way take with them the average energy per atom associated with the cloud, 3 $k_{\rm B}T$ and hence do not cause any heating. Losses happen at a rate $\alpha = 1/\tau_b$ where τ_b is a characteristic lifetime associated with losses of this kind. Although not density dependent, background collisions are sensitive to the vapour pressure providing the source of background atoms. Typically in the science cell, lifetimes in excess of 100 s are possible considering this type of loss alone.

Two-body collisions

Two-body loss, as the name suggests, occurs as the result of collisions of two atoms with a number of specific mechanisms being grouped under this same title.

When the atomic separation is small enough such that the electron wave functions of the two atoms are able to overlap, an exchange interaction arises due to the anti-symmetry of the electronic wave function. The exchange interaction can couple singlet and triplet states [161] yet, due to its spherical symmetry, conserves internucleus angular momentum L and m_L thus implying only transitions with $\Delta m_F = 0$ are allowed. By pumping atoms to the stretched state (e.g. $F = 2, m_F = -2$) this exchange interaction can be eliminated. However, the lifetime of such a sample is still limited by other loss processes such as dipolar interactions.

Dipolar interactions originate from the spin-spin interaction between atoms. These can be direct (magnetic dipole-dipole) or indirect (2nd order spin-orbit). In the case of ^{87}Rb these contributions almost exactly cancel, leading to a significantly reduced two-body loss coefficient. Unfortunately, this is not the case in ^{85}Rb. Dipolar relaxation occurs when two atoms collide, exchanging angular momentum between their orbital motion and their intrinsic spin thus scattering into an untrapped spin state. The rate for such losses goes as $K_2\langle n\rangle$ and so losses of this nature are more prominent in regions of higher density. As a consequence, atoms lost in this way take with them $E = 9/4\ k_{\mathrm{B}}T$; less than the average energy of the cloud (where the average applies to a sample in a harmonic trap) and thus contribute to its heating.

Three-body collisions

In the cold, dense centre of the trap there is an increased probability of finding multiple atoms close together, the result of this being three-body collisions (three-body recombination)[2]. Such collisions can lead to molecule formation between two of the atoms with the third remaining unbound, carrying away

[2]Three-body recombination rates differ between noncondensate and condensate samples as confirmed experimentally in [176]. Theoretical models [177] predict a factor of 3! difference should be apparent between the two cases with thermal samples displaying the greater losses. This is the result of statistical correlations between atoms, leading to density fluctuations which are more prominent in the thermal cloud compared to the condensate, i.e. condensate atoms are less bunched than noncondensate atoms. As a result there is a higher probability of finding three atoms close together in the thermal cloud, hence three-body loss increases.

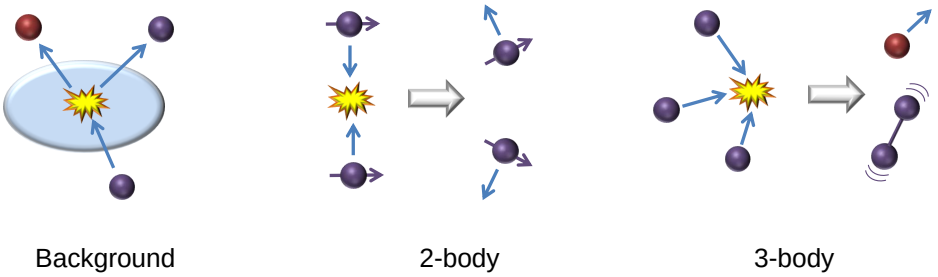

Figure 6.7: Inelastic loss mechanisms: Atoms can be lost from the trap as a result of simple collisions with other background gas atoms or as a result of more complicated two and three-body processes. Here atoms are lost as a result of spin flips or increases in energy, sufficient to liberate them from the trapping potential.

excess energy and momentum from the collision. In the recombination process the molecular binding energy ϵ is released as kinetic energy with the molecule receiving $\epsilon/3$ and the atom $2\epsilon/3$ [178]. If ϵ is large compared to the trapping potential both the atom and the molecule will be expelled from the trap. Alternatively either just the atom or just the molecule will escape the trap. If the molecule remains trapped there is potential for further collisions (to quench its high vibrational level) thus expelling more atoms from the trap. Recombination heating can then arise as excess kinetic energy is distributed within the ensemble.

Three-body losses have a stronger density dependence than two-body with the associated rate scaling as $K_3\langle n^2\rangle$. Atoms lost via a three-body process contribute more significantly to the heating of the sample, on average only taking away 2 $k_{\mathrm{B}}T$. Atoms being lost in this way, preferentially from the trap centre, causes 'anti-evaporation' as the coldest atoms are removed.

In the case of large positive a_s theoretical studies [179, 180, 181, 182] predict three-body loss should scale as a_s^4, with different mechanisms responsible for the loss when $a_s < 0$ and $a_s > 0$ [181]. This has been experimentally verified using a magnetic Feshbach resonance to precisely tune the scattering length of cesium atoms [183]. The importance of avoiding the hydrodynamic collision regime during evaporative cooling is also highlighted in Ref. [183] as recombination heating (caused by collisions of the atoms or molecules) can

limit the efficiency of evaporative cooling such that it becomes impossible to reach degeneracy.

Two and three-body loss close to the 155 G Feshbach resonance

Both two and three-body losses have previously been studied close to the 155 G Feshbach resonance [155]. At 250 G these were measured to be $K_2 = (1.87 \pm 0.95 \pm 0.19) \times 10^{-14}$ cm^{3}s^{-1} and $K_3 = (4.24^{+0.70}_{-0.29} \pm 0.85) \times 10^{-25}$ cm^{6}s^{-1}, decreasing to a minimum as the magnetic field is reduced before peaking at the Feshbach resonance. Fortunately, the minimum of the inelastic scattering rate does not coincide with that of the elastic scattering. Instead the inelastic minimum is located at ∼175 G. Here K_3 falls to around 10^{-26} cm^{6}s^{-1} and K_2 remains at 10^{-14} cm^{3}s^{-1}. Using these values we can calculate a rough estimate of the lifetimes associated with these losses in ^{85}Rb, assuming an atomic density of 1×10^{12} cm^{-3},

$$\tau_{2\text{body}} \sim \frac{1}{K_2 \langle n \rangle} \approx 50 \text{ s}, \tag{6.12}$$

$$\tau_{3\text{body}} \sim \frac{1}{K_3 \langle n^2 \rangle} = \frac{1}{\frac{8}{\sqrt{27}} K_3 \langle n \rangle^2} \approx 1.5 \text{ s}. \tag{6.13}$$

Predicted [184] and experimentally verified [176] to be low, the loss rates for ^{87}Rb atoms are in stark contrast to those of ^{85}Rb. It is interesting to contrast the values for K_2 and K_3 in ^{85}Rb to typical values measured for ^{87}Rb. Work by Burt *et al.* investigated the loss in both condensate (c) and non-condensate (nc) ^{87}Rb atoms [176], bounding the two-body rate, $K_2^{\text{nc}} \leq 1.6 \times 10^{-16}$ cm^{3}s^{-1}, and measuring $K_3^{\text{nc}} = 4.3(1.8) \times 10^{-29}$ cm^{6}s^{-1} and $K_3^{\text{c}} = 5.8(1.9) \times 10^{-30}$ cm^{6}s^{-1} (confirming the 3! difference predicted theoretically [177] for condensate and non condensate atoms). The two orders of magnitude difference in K_2 and five orders of magnitude difference in K_3 between ^{85}Rb and ^{87}Rb highlights one of the key obstacles in the cooling of ^{85}Rb to degeneracy. It is therefore imperative to devise an evaporation strategy which exploits the field dependence of both elastic and inelastic scattering.

6.3.4 Heating rate in the dipole trap

Although, strictly speaking, heating due to the scattering of photons from the optical trap does not constitute an inelastic loss mechanism, it falls into a similar category of processes which work *against* the evaporation. The heating rate for a red detuned dipole trap is given by [92],

$$\dot{T}_{\mathrm{red}} = \frac{2/3}{1+\kappa} T_{\mathrm{rec}} \frac{\Gamma}{\hbar|\Delta|} |U_0|. \tag{6.14}$$

The parameter $\kappa = \bar{E}_{\mathrm{pot}}/\bar{E}_{\mathrm{kin}}$ is the ratio of potential to kinetic energy and for a 3D harmonic trap, $\kappa = 1$. The recoil temperature, $T_{\mathrm{rec}} = \hbar^2 k^2/(2mk_{\mathrm{B}})$, is the temperature associated with the kinetic energy gain by emission of a single photon.

At the initial point of loading into the crossed dipole trap the photon scattering rate of 0.04 s^{-1} leads to a heating rate of $\sim$4 nKs^{-1}. By the final stage of our evaporation this has reduced to less than 0.02 nKs^{-1}.

6.4 Evaporative cooling

With this understanding of how the scattering properties of the atoms impact upon the trapped cloud as a whole, we can then proceed to try and evaporatively cool ^{85}Rb in an attempt to reach degeneracy in the crossed dipole trap.

To produce an ultracold cloud of ^{85}Rb atoms in the $F = 2, m_F = -2$ state the same general experimental procedure used to cool and transport ^{87}Rb is employed (with the necessary modifications to the frequencies of the laser light), typically producing a trapped atomic cloud containing $\sim 5\times10^8$ atoms at a temperature of $\sim$ 380 μK. Forced radio frequency (RF) evaporation of the sample in the quadrupole trap is then carried out with the optimized evaporation trajectory taking 26 s in total due to relatively slow rethermalization caused by the low s-wave scattering cross-section in this temperature range [156]. (However, we note that the linear potential produced by the quadrupole trap means it is possible to obtain runaway evaporation for a lower ratio of elastic-to-inelastic collision compared to a harmonic potential [85]). The RF evaporation results in a cloud of 3×10^7 ^{85}Rb atoms at 42 μK

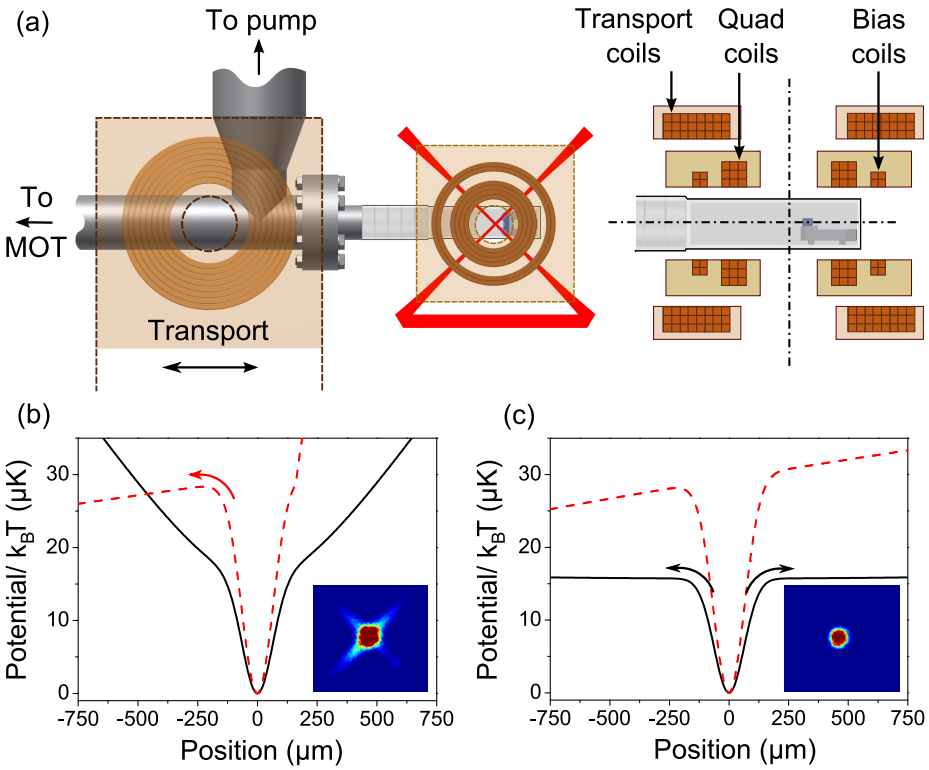

Figure 6.8: ^{85}Rb crossed trap experimental setup: (a) Experimental setup showing the arrangement of coils around the UHV cell and the beam geometry used to create the crossed dipole trap. Trapping: Potentials produced horizontally along one of the beams (black, solid) and vertically (red, dashed) in the hybrid (b) and levitated (c) crossed dipole traps. Insets: False color images of atoms in the respective traps, viewed from above.

with a phase space density (PSD) of 5×10^{-5} in the magnetic quadrupole trap. At this temperature the quadrupole trap lifetime is limited by Majorana spin flips as the coldest atoms spend increasing amounts of time close to the magnetic field zero. To proceed, we transfer a fraction ($\sim$ 20 %) of the atomic sample into the crossed optical dipole trap shown in Fig. 6.8(a) and, in doing so, gain a factor of 30 in PSD due to the drop in temperature and increase in trap frequencies. Despite losing atoms in the transfer, in the new trap atoms equilibrate to $\sim U_0/10$ (roughly 10 μK) which leads to this dramatic increase in phase space density and puts us well into the ultracold regime where the elastic collision cross-section can then be tuned using the (magnetic field dependent) scattering length (see Fig. 6.6).

The same crossed dipole trap described in chapter 5 is used to trap both ^{85}Rb and ^{87}Rb. Again the dipole trap is switched on during the RF evaporation stage. To complete the loading, the quadrupole gradient is relaxed from 180 Gcm^{-1} to $\sim$ 21.5 Gcm^{-1} in 500 ms. The final quadrupole gradient used is just less than that sufficient to support atoms against gravity ($\sim$ 22.4 Gcm^{-1}). The presence of the magnetic gradient leads to weak magnetic confinement along the beams ($\sim$20 Hz) [91], enhancing the trap volume and resulting in a trap depth set by the vertical direction (Fig. 6.8(b)). In addition, the offset from the field zero leads to a small magnetic field ($\sim$ 0.3 G) at the location of the crossed dipole trap which ensures a quantisation axis is maintained. As described in section 5.3, the atoms are subject to both optical and magnetic confinement hence we refer to this as the hybrid trap.

In order to reach the Feshbach resonance it is necessary to apply a moderate bias field ($\sim$ 155 G). The positioning of the bias coils, relative to the quadrupole trap, is shown in Fig. 6.8(a). This leaves the trapped atoms still levitated against gravity, however the confinement produced by the quadrupole trap along the dipole beams is effectively removed, dropping to $\sim$0.9 Hz as shown in section 3.3.3. Atoms now only remain at the intersection of the trap. This is our levitated crossed optical dipole trap. Before switching on the bias field, we first evaporate by ramping down the power of the hybrid trap at low field ($a_s \approx -460\ a_0$ [173]) where inelastic losses are known to be low [185]. This allows us to exploit the enhanced volume of the hybrid trap to improve the transfer into the levitated crossed dipole trap.

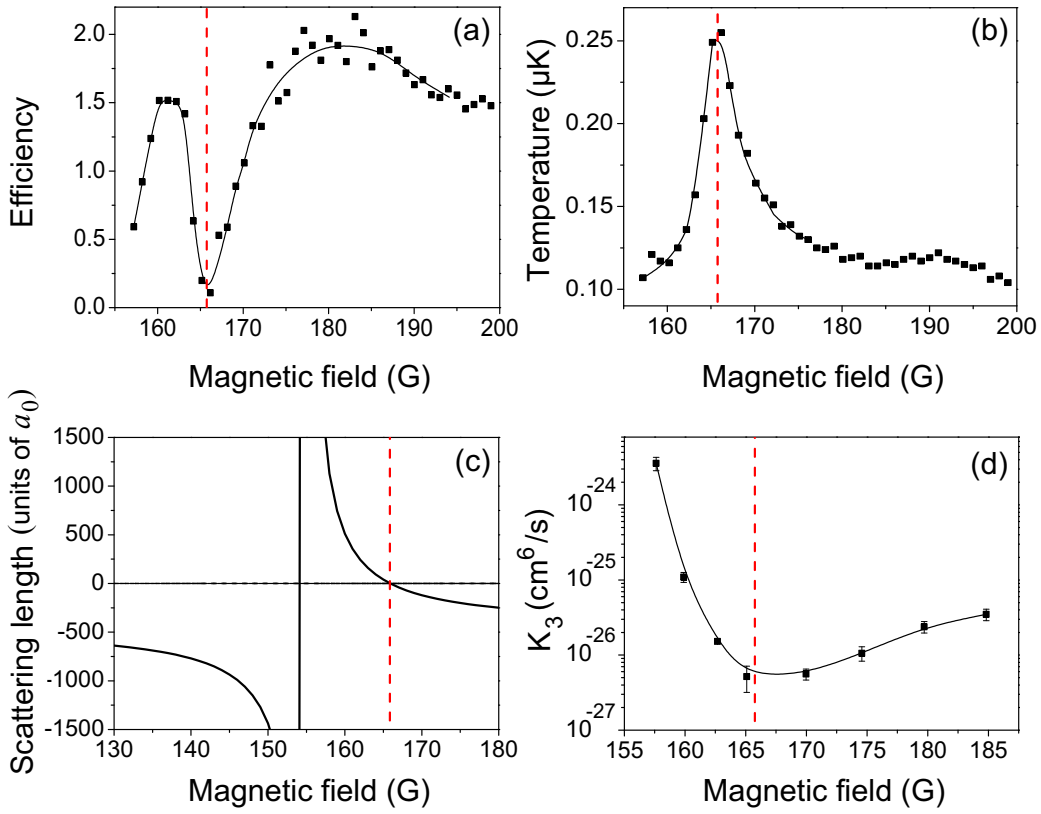

Figure 6.9: ^{85}Rb Collisional properties: Position of $a_s = 0$ is marked by the red, dashed line: (a) Evaporation efficiency (see text) of a fixed evaporation sequence carried out at different magnetic fields close to the Feshbach resonance. (b) The effect on fitted temperature of the same evaporation ramps. (c) Feshbach resonance in the $F = 2, m_F = -2$ state of ^{85}Rb. The scattering length is given in units of the Bohr radius, $a_0 \approx 0.529 \times 10^{-10}$ m. (d) Magnetic field dependence of the three-body inelastic loss rate near the Feshbach resonance. Solid lines in (a), (b) and (d) are a guide to the eye only.

In contrast to the hybrid case, in the levitated trap evaporation happens preferentially along the dipole beams, as shown in Fig. 6.8(c), resulting in a trap with roughly half the depth compared to the zero bias field case.

To achieve efficient evaporation in the levitated trap it is necessary to understand the interplay between elastic and inelastic collisions close to the Feshbach resonance. We explore this by indirectly probing the collision ratio, carrying out a fixed evaporation sequence for different magnetic fields. The efficiency, γ, of the evaporation sequence can then be calculated from the initial (i) and final (f) number, N, and PSD of the gas according to:

$$\gamma = -\frac{\log(\mathrm{PSD}_f/\mathrm{PSD}_i)}{\log(N_f/N_i)}.$$

The efficiency for a 50 G window spanning the zero crossing of the Feshbach resonance is shown in Fig. 6.9(a). The two clear peaks at 161 G and $175-185$ G highlight the most efficient fields at which to evaporate with the broad $a_s < 0$ peak, $175-185$ G, giving marginally better performance. As a_s approaches zero (red dashed line) the elastic collision rate reduces and rethermalisation ceases. As a result the efficiency tends to zero and we see a corresponding peak in the fitted cloud temperature, Fig. 6.9(b).

6.4.1 Three-body loss: Measuring K_3

The distinct structure evident in Fig. 6.9(a) follows from the magnetic field dependence of the elastic and inelastic collision rates. The elastic collision rate, determined by the atomic scattering length (Fig. 6.9(c)), varies by many orders of magnitude over the region of interest as shown previously in Fig. 6.6. Similarly, inelastic losses are known to exhibit a strong field dependence close to the resonance [155]. This is illustrated in Fig. 6.9(d) which shows the change in the three-body inelastic loss rate, K_3, measured close to the Feshbach resonance.

To determine the three-body loss rate at a given magnetic field an atomic sample is first prepared at 175 G with a temperature of ~ 0.15 μK. The magnetic field is then ramped from 175 G to a new value in 10 ms. Following the ramp, the trap is compressed (in 1 s) by linearly increasing the laser power. This deepens the trap from 1.4 μK to 27.5 μK, increasing the atomic

density. The increased trap depth also suppresses evaporation effects due to the relative difference in cloud temperature and trap depth. (Assuming the compression is adiabatic, the temperature of the cloud scales linearly with the trap frequency ($T'/T \sim \omega'_{\rm ho}/\omega_{\rm ho}$). The trap frequency depends on the beam power as $\omega \sim \sqrt{P}$ however, the trap depth scales faster with power, instead going as $U \sim P$ thus it is possible to deepen the trap, relative to the cloud temperature.) As atoms are lost from the trap, Fig. 6.10(a), this makes it possible to observe heating as a result of the three-body effect, Fig. 6.10(b).

The lifetime of the atomic cloud in this deep trap is measured and the three-body loss rate, K_3, determined by fitting the data with the solution to a pair of coupled differential equations describing the atom number evolution with time [183],

$$\frac{dN}{dt} = -\alpha N - \gamma \frac{N^3}{T^3}, \tag{6.15}$$

and the associated change in temperature,

$$\frac{dT}{dt} = \gamma \frac{N^2}{T^3} \frac{(T + T_{\rm h})}{3}. \tag{6.16}$$

Here $\alpha = 1/\tau_b$ accounts for background losses and $\gamma = \frac{K_3}{\sqrt{27}}(m\overline{\omega}^2/2\pi k_{\rm B})^3$ where $\overline{\omega}$ is the geometrically averaged trap frequency. $T_{\rm h}$ is the recombination heating associated with the loss. It is likely that there is a combination of both two and three-body loss processes going on in the trapped gas, however it is often difficult to differentiate between the two [155]. We choose to fit the data using this model of K_3 as the compression of the trap is designed to increase the atomic density. As three-body loss scales more strongly with density than two-body loss the compression should therefore favour the three-body scaling.

Looking again at Fig. 6.9(c) and (d) it is apparent that for a given magnitude of scattering length the inelastic losses are marginally lower on the $a_s < 0$ side of the zero crossing as previously predicted and observed [181, 155]. This leads to slightly better evaporation performance for the $175 - 185$ G peak (Fig. 6.9(a)).

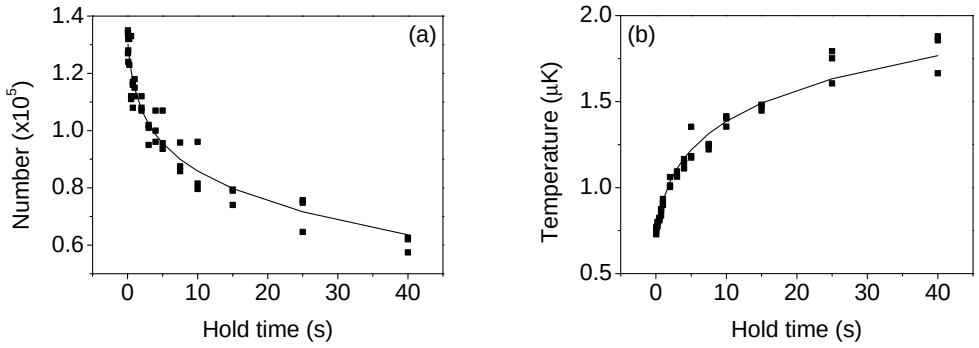

Figure 6.10: Determining K_3: (a) Atom loss from the 'deep' crossed trap due to three-body loss processes. (b) Increase in cloud temperature observed as a result of three-body heating. Solid lines are fits to the data based on Eq. (6.15) and Eq. (6.16).

6.5 Bose-Einstein Condensation

With this understanding of the collisional properties of the trapped cloud, it is then clearer how best to achieve BEC in the optical trap. Following a low field evaporation stage in the hybrid trap, the bias field is ramped rapidly ($\sim$ 10 ms) to $175 - 185$ G to exploit the window of efficient evaporation. It is at this low loss region that the majority of the subsequent evaporation is carried out. Following a 500 ms hold to allow atoms to equilibrate in the reduced trap depth, we apply two more evaporation ramps resulting in a sample of 2.5×10^5 atoms at 150 nK with a PSD of 0.5. Unfortunately, stable condensates cannot be created at this magnetic field due to the large, negative scattering length ($\sim -200\ a_0$) [13] hence we must ramp the bias field again, this time to 161.3 G where the scattering length, calculated from Eq. (6.8), is positive ($\sim 315\ a_0$). A further evaporation ramp is carried out here reducing the beam power to 0.3 W and creating an almost spherically symmetric trapping geometry, $\omega_{x,y,z} = 2\pi\times(31,\ 27,\ 25)$ Hz. To reach BEC the sample is held in this final trap for up to 1.5 s to allow for further plain evaporation. A schematic of the evaporation sequence, from the evaporation in the magnetic quadrupole trap, is shown in Fig. 6.11. The total time for the evaporation sequence in the dipole trap is 14.5 s. We note that, owing to the width of the efficiency peak shown in Fig. 6.9(a), we are able to produce

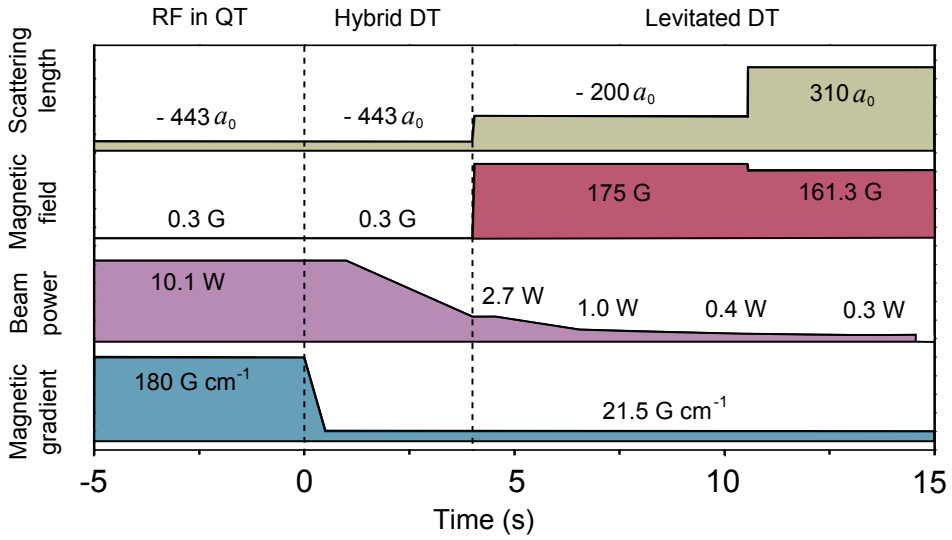

Figure 6.11: ^{85}Rb BEC experimental timing sequence: Relative timings of the crossed dipole trap, quadrupole gradient and bias field ramps used to reach degeneracy.

condensates of a similar size over a range of fields from 160 G ($\sim$ 510 a_0) to 163 G ($\sim$ 150 a_0). However, below 160 G an increase in the inelastic loss rate makes condensation difficult and BECs of only a few thousand atoms are formed. Similarly above 163 G the elastic cross-section is too small for efficient rethermalisation. We also note that it is possible to create condensate when carrying out all of the (high magnetic field) evaporation at 161.3 G, however, this again results in smaller BECs due to the reduced evaporation efficiency.

The complete evaporation trajectory to BEC is shown in Fig. 6.12(a). Despite the difficulties associated with cooling ^{85}Rb, it is clear that it is possible to maintain a highly efficient evaporation trajectory both in the magnetic (circles) and optical (squares) trap. Unlike the experiment in [30], we do not suffer the catastrophic factor of 50 loss as we approach the BEC transition. We attribute this to a lower atomic density meaning the effect of three-body loss is not as severe in our trap. By varying the final trap depth we are able to see the transition from the thermal cloud to BEC as shown in Fig. 6.12(b), with the characteristic double-distribution signature occurring with around 10^5 atoms in the trap. By reducing the trap depth to $\sim$ 360 nK we are able to produce pure condensates with $\sim 4 \times 10^4$ atoms.

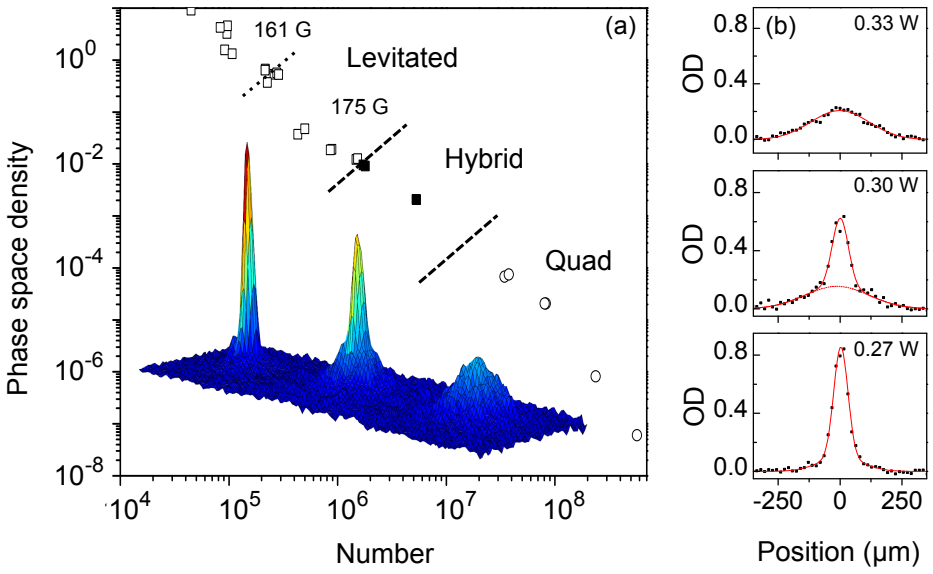

Figure 6.12: Evaporation trajectory to reach ^{85}Rb BEC: (a) After RF evaporation in the quadrupole trap (◯), atoms are loaded into the hybrid dipole trap (■). Following an initial evaporation stage in the hybrid trap, a $175 - 185$ G bias field is applied. This produces the levitated trap (□) in which further evaporation is carried out. At a PSD of ∼0.5 the bias field is ramped to 161.3 G and a final evaporation stage is performed to reach BEC. Inset: Density profiles for (R-L) a thermal, bimodal and condensed atomic sample. (b) Horizontal cross-sections of the condensate column density for a thermal (top), bimodal (centre) and condensed (bottom) sample as the dipole beam power (top right) is reduced. Solid lines are fits to Gaussian and bimodal Gaussian distributions.

6.6 Demonstration of tunable interactions

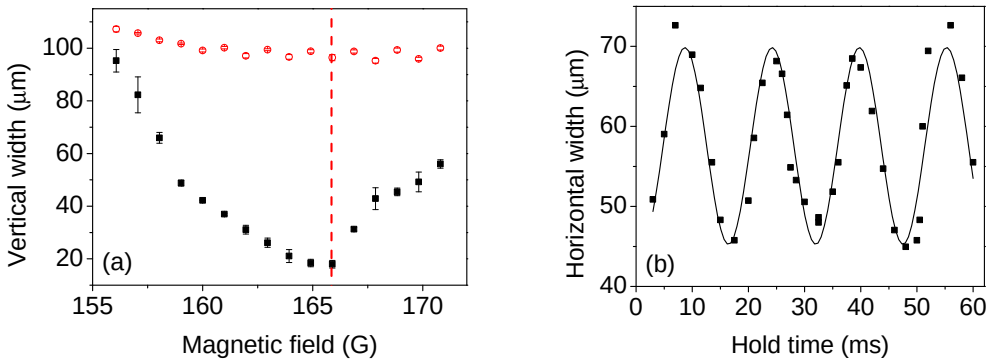

Figure 6.13: BEC with tunable interactions: (a) Change in vertical size of a pure condensate (filled squares) and thermal cloud (open circles) as a function of magnetic field applied during time of flight. (b) Breathing mode oscillation set up by jumping the atomic scattering length from $\sim 315\ a_0$ to $\sim 50\ a_0$. The hold time shown is that at the new scattering length of $\sim 50\ a_0$.

In order to demonstrate the tunable nature of the condensate we present two simple experiments. In the first we alter the magnetic field synchronously with the release from the dipole trap and observe the variation of the expansion of the cloud following 55 ms of levitated time of flight. As shown by the filled squares in Fig. 6.13(a) the change in mean field interaction strength with magnetic field manifests itself in a change in the cloud size. We see that the BEC reaches its minimum size as the scattering length approaches zero at 165.75 G [172], marked by the red, dashed line. Over the region of $a_s > 0$ the condensate number remains approximately constant. As a_s becomes negative, the subsequent collapse [34] of the BEC causes an increase in cloud size. In comparison, when the same field jump is carried out using thermal atoms (for 25 ms time of flight) the cloud is insensitive to the atomic interactions and hence no change in shape is observed (open circles).

The second, elegant demonstration of tunable interparticle interactions is to set up a breathing mode oscillation of the condensate by jumping the magnetic field, and hence scattering length, and observing the subsequent dynamics of the cloud at the new value of a_s. The result for a jump from $\sim 315\ a_0$ to $\sim 50\ a_0$ is shown in Fig. 6.13(b). A jump of this type (to

small a_s but $a_s \neq 0$) in our almost spherically symmetric trap leaves us in the Thomas-Fermi regime and hence the resulting oscillation occurs at a frequency of $\sqrt{5}\omega_{x,y}$ [62]. The trap frequency extracted using this model is in good agreement with the value measured by parametric heating.

6.7 Collapse of an attractive condensate

In 1D, attractive interactions in a condensate can compensate exactly for the dispersion otherwise present in a wavepacket [13]. This results in highly stable soliton solutions to the NLSE. In contrast, in 3D all solutions are unstable and the system will undergo collapse. However, the spatial localisation provided by a trap can in fact stabilize the condensate if the non-linearity is relatively weak. The stability can be parameterised [63] by the dimensionless parameter,

$$k = \frac{N_{\rm cr}|a_s|}{a_{\rm ho}}, \tag{6.17}$$

where $a_{\rm ho} = \sqrt{\hbar/m\omega_{\rm ho}}$ is the harmonic oscillator length. The existence of these non-collapsing, metastable states therefore depends on the atom number, interaction strength and the shape and strength of the trapping potential.

The collapse process has been explored theoretically using variational [68, 186, 69], perturbative [187] and numerical [66, 67, 13, 68] methods. In the next section we review previous experimental investigations of the collapse which provide a valuable testing ground for these theoretical models.

6.7.1 Collapse in ^{7}Li and ^{85}Rb condensates

Once the number of atoms in the condensate exceeds the limiting critical number $N_{\rm cr}$, determined by Eq. (6.17), a collapse occurs. Experimentally this has been dubbed the 'Bosenova' in analogy to the astronomical phenomena of stellar explosion.

The first experimental insights into BECs with attractive interactions were made using ^{7}Li [188]. Here the negative scattering length, $a_s = (-27.4 \pm 0.8)\ a_0$, means that the condensate number, N_0, grows until the condensate

eventually collapses. During the collapse the density of the cloud rises thus increasing both the elastic and inelastic collision rates. This causes atoms to be ejected from the condensate with high energy in a violent explosion. Following this, the condensate begins to reform, fed by the surrounding bath of thermal atoms also present in the trap. If observed for an extended period the system exhibits a saw-tooth dynamic of growth and collapse [189] until equilibrium is eventually reached. Throughout, the maximum condensate number is strictly limited to the critical number for an attractive BEC (for this experiment $N_{\mathrm{cr}} \approx 1,250$). It is also possible that collapse occurs even with $N_0 < N_{\mathrm{cr}}$ due to quantum tunneling effects and thermal fluctuations in the cloud leading to instability.

Further insight into the collapse phenomena came from the group at JILA (Boulder, US) in 2001 [34, 35], carrying out a controlled collapse using a pure ^{85}Rb condensate. Tuning the scattering length from positive to negative using the same 155 G Feshbach resonance described in section 6.3.2 not only enabled the collapse process to be precisely initiated but also allowed the condition $N_0 > N_{\mathrm{cr}}$ to be fulfilled prior to the collapse, unlike systems using fixed negative scattering lengths. Along with control of the initial condensate number, control over scattering length made the testing of critical number models possible, finding the exact scattering length necessary to collapse the cloud, a_{cr}. Early work examining the point of collapse using slow field ramps confirmed the relationship between critical number and scattering length, determining the stability constant, k, for the trap. Later improvements to the calibration of the Feshbach resonance detailed in section 6.3.2, enhancing precision, then found k to be in excellent agreement with theoretical models [37].

Following this, the JILA experiments were then extended to study the dynamics of the collapse, measuring the evolution of the condensate number following a 'sudden' change in the scattering length. Measurements of atom number as a function of time showed a sudden yet delayed loss of atoms. As the interactions are made attractive the condensate begins to shrink in size, thus increasing its density. This contraction tends to accelerate with time eventually leading to collapse of the condensate. The time for the collapse to begin t_{collapse} was found to be shorter for larger $|a_{\mathrm{collapse}}|$ as the stronger at-

traction between atoms in the condensate results in a more rapid contraction of the cloud. Following the collapse, a stable remnant component was formed in the trap. Notably, the number of atoms maintained in this remnant, N_f was found to depend strongly on N_0 and a_{collapse} and in many cases exceeded N_{cr}. This remnant was observed to persist in the trap for more than 1 s, oscillating in a highly excited state[3].

In addition, a number of more qualitative features were observed about the collapse process in the ^{85}Rb experiment. The first of these features was bursts of atoms with variable energies being ejected from the condensate. These bursts would then focus at multiples of $T_x/2$ and $T_r/2$, where $T_{x,r} = 2\pi/\omega_{x,r}$ is the trap period in the axial (x) and radial (r) dimensions. In all experiments only full, never partial, collapse was observed. However, if interrupted (by jumping the scattering length away from the collapse point), jets of atoms were also formed. Unlike the bursts, these streams of atoms were found to have highly anisotropic velocities and were interpreted as indicating the local pinching of the wavefunction during the collapse rather than a smooth global collapse of the BEC.

The collapse process has since been revisited by the group at the Australian National University (Canberra, Australia) [38]. Again using ^{85}Rb, measurements of the collapse time have been shown to be in good agreement with theoretical models of the GPE which take into account three-body loss mechanisms.

6.7.2 Observation of a collapsing condensate

To observe the collapse of an attractively interacting condensate we begin by preparing a BEC with repulsive interactions ($a_s \approx 400\ a_0$). The scattering length is then jumped to a large negative value, (in the first experiment to $a_s = -95(6)\ a_0$ and in the second to $a_s = -135(7)\ a_0$), and held there for some time, t_{evolve}. The cloud is then imaged after 20 ms time of flight during which time the interactions are switched back to repulsive to cause the condensate to expand sufficiently before imaging.

[3]Later these highly excited remnants with $N_f > N_{\text{cr}}$ were found to be associated with the formation of bright matter-wave solitons [7] as discussed in section 7.1.1.

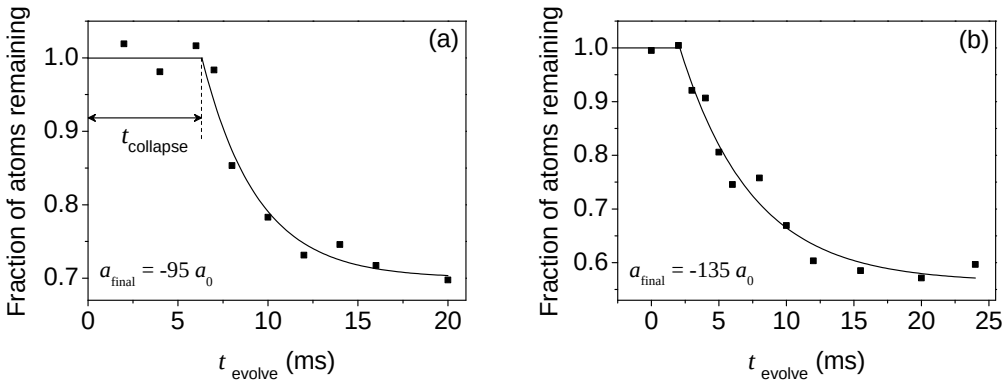

Figure 6.14: Collapse of an attractive BEC: The effect of jumping the scattering length of a stable Bose-Einstein condensate from positive to negative is to induce a collapse of the condensate, assuming the number of atoms is greater than the critical number for the field. The loss of atoms from the condensate is dramatic but delayed from the point of the field change by a time t_{collapse}. This time decreases for larger $|a_{\text{final}}|$.

Figure 6.14 shows the evolution of the atom number in the condensate as a function of t_{evolve} for two different experimental conditions. As seen previously [34, 38], there is a dramatic loss of atoms from the condensate which starts only after some delay, t_{collapse}. As in [38] we fit the data with the form

$$N(t) = (N_0 - N_f) \exp\left[-\frac{(t - t_{\text{collapse}})}{\tau_{\text{decay}}}\right] + N_f, \tag{6.18}$$

where N_0 and N_f are the atoms numbers at $t < t_{\text{collapse}}$ and $t \gg t_{\text{collapse}}$ respectively.

In Fig. 6.14(a) the initial cloud contains $N_0 = 1.4(1) \times 10^4$ at a scattering length of $a_s = 480(20)\ a_0$. A jump to -95(6) a_0 results in a collapse time of 6.3(5) ms, leaving a surviving fraction of $N_f/N_0 = 0.70(2)$. Comparing this to Fig. 6.14(b) where $N_0 = 2.0(2) \times 10^4$ and the initial scattering length $a_s = 400(6)\ a_0$ is jumped to a more negative value of $-135(7)\ a_0$ we can observe a change in the collapse process. The more negative scattering length results in an increased loss of atoms, $N_f/N_0 = 0.56(2)$, and a much shorter collapse time of only 2.0(5) ms.

This decrease in the collapse time as the atomic interactions are made more attractive is in agreement with [38]. As one would expect, making a_s more

negative has the effect of increasing the interaction strength hence accelerating the collapse process.

Calculating the critical number for the two final configurations, assuming $\omega_{\rm ho} = 2\pi \times 29$ Hz and $k = 0.575$ i.e. a spherical trap, we find $N_{\rm cr}$ is only ~ 200 atoms due to the large (negative) scattering length. However, the number of atoms observed to survive the collapse $N_{\rm remnant}$ is many times this critical value. This result is in agreement with previous measurements of the collapse process [34, 7] where the formation of multiple bright solitary matter-waves was put forward as an explanation of the $N_{\rm remnant} > N_{\rm cr}$ result.

It is possible that following the collapse a similarly highly excited state (as in [34]) may be produced in the crossed dipole trap. Unfortunately, the large negative scattering lengths, and hence low critical numbers, used here means that if solitary waves are formed, we may be unable to resolve them with our current imaging system. However, jumps to smaller scattering lengths would allow the collapse phenomena to be investigated further using this experiment thus allowing one to test 'how 1D' a system needs to be in order to observe solitary waves. As we shall see in chapter 7, the addition of an optical waveguide to the experimental setup means that the collapse could also be investigated as a function of trap geometry.

6.8 Summary

In this chapter we have explored some of the characteristics which make ^{85}Rb such a difficult yet appealing species to work with. Through a careful exploration of the atomic scattering properties we have successfully demonstrated the condensation of ^{85}Rb by direct evaporation in an optical dipole trap. Unlike previous experiments we require neither the aid of additional refrigerant species nor excessively weak traps leading to long duty cycles. With this tunable BEC we are able to observe the effect of the changing scattering length on the cloud size and recreate the collapse of an attractive condensate observed by other groups.

From here, our next step requires a modification of the trapping geometry. Although attractive condensates can be created, the almost spherical crossed

dipole trap is poorly suited to the formation of bright solitary matter-waves. To produce a more 1D geometry the condensate must be transfered into an optical waveguide, providing tight radial confinement but only weak axial trapping. In the next chapter we discuss the transfer into this new beam and search for the experimental signature of soliton formation.

Chapter 7

Formation of bright solitary matter-waves

7.1 Introduction

Following the successful creation of a tunable Bose-Einstein condensate we turn our attention to the formation of a bright solitary matter-wave from the condensate. In this chapter we begin by reviewing previous experiments and the results which have provoked such vast theoretical interest in the creation and dynamics of these non-dispersive wavepackets. We then introduce the new trapping geometry, an optical waveguide, which must be implemented to allow the formation of the solitary waves and discuss how the condensate is loaded from the crossed dipole trap.

Once in the waveguide, the atomic interactions can be tuned, again using the 155 G Feshbach resonance, to control the expansion of the condensate as it propagates along the waveguide. We measure the expansion rate of the condensate as a function of Na_s and compare this to a 3D GPE simulation. With careful tuning of the scattering length we can halt this expansion and in doing so create a bright solitary matter-wave. Finally we demonstrate classical reflection from a broad, repulsive, Gaussian barrier, contrasting this to a repulsive BEC undergoing the same reflection.

7.1.1 Observation of bright solitary matter-waves

The advent of optical trapping led to the realisation of experimental geometries closer to the ideal 1D limit. This, in combination with control of the atomic scattering length via Feshbach resonances, led to the first observations of bright solitary matter-waves by groups at Rice University (Houston, US) [5] and École Normale Supérieure (Paris, France) [6] in 2002 using ^{7}Li. Despite two inherently similar experiments, the ENS group succeeded in producing a single solitary wave whereas the Rice experiment resulted in trains of multiple solitary waves.

In order to utilize the Feshbach resonance in the non-magnetically trappable $F = 1, m_F = 1$ state of ^{7}Li it is necessary to work using an optical dipole trap [92]. In both experiments initial cooling of the atomic sample was carried out in a magnetic trap using the $F = 2, m_F = 2$ state before transferring to a dipole trap and flipping the spin state of the atoms to suppress two-body loss mechanisms and allowing access to the Feshbach resonance.

In the ENS experiment optical confinement was realised using a red detuned crossed dipole trap. Here condensates of 2×10^4 atoms were produced with $a_s = +39.7a_0$ in a $\omega = 2\pi \times (710, 1000, 710)$ Hz crossed trap. After the creation of the BEC, the scattering length was tuned close to $a_s = 0$ before adiabatically reducing the power in one of the beams, producing a cylindrical geometry, $\omega = 2\pi \times (710, 710, 50)$ Hz. The bias field, and hence scattering length, was then ramped to its final value before the weak beam was switched off, releasing the cloud into a 1D waveguide. In this trap, the atoms experience a slightly expulsive potential due to the magnetic coils used to produce the bias field. As a typical example, at $B = 520$ G, the trap frequency along the waveguide can be considered imaginary, around $\omega_z = 2i\pi \times 78$ Hz. Tuning the scattering length to a small negative value, $a_s = -3.97\ a_0$, resulted in a soliton of 6×10^3 atoms able to propagate without dispersion for over 1.1 mm.

In contrast to the crossed ENS trap, the Rice experiment used a single red detuned dipole beam to provide radial confinement, however two additional blue detuned beams were needed in order to cap the ends of the trap in the axial direction. After forming a condensate of 3×10^5 atoms with $a_s \approx 200a_0$

the magnetic field controlling the scattering length was ramped exponentially to the final value and the laser end caps switched off thus setting the resulting solitary waves in motion.

In this experiment multiple solitary waves were observed. The number of these wavepackets, N_s, was found to be insensitive to the time constant of the exponential magnetic field ramp, however, N_s increased linearly with Δt, the time delay between the switch off of the end caps and the time of the scattering length change to $a_s < 0$. For the Rice experiment 4 solitary waves were observed for $\Delta t = 0$ with this number increasing to 10 for $\Delta t = 35$ ms. The wavepackets were observed to propagate for $\sim$3 s completing several periods of oscillation along the waveguide, this being limited by atom loss rather than dispersion effects.

With many solitary waves confined in a single trap it becomes possible to explore the dynamics of the wavepackets. Observation of the solitary wave motion showed evidence of a short range repulsive interaction between neighbouring wavepackets raising many questions regarding their formation and collisional dynamics. A possible explanation for the formation of multiple solitary waves was the presence of a modulational instability [73]. Here, phase fluctuations of the condensate lead to a local increase in density at wavelengths approximately equal to the healing length. The attractive nonlinearity leads to the growth of these density fluctuations and the emergence of solitons.

In the non-interacting limit, two colliding solitary waves should pass through each other, emerging from the collision unaltered. In reality the collisional dynamics revealed a surprising result, implying repulsive interaction between two solitary waves undergoing a collision. This interaction manifested itself experimentally as a change in the spacing between neighbouring solitary waves, increasing near the centre of the oscillation and decreasing near the turning points. This result implied a relative phase of $\phi = \pi$ between neighbouring solitary waves, somehow imprinted during their formation.

It was not until 2006 that bright solitary waves were again investigated experimentally. In the intervening years many theoretical models were developed to explain the repulsive interactions seen in the Rice experiment between

neighbouring solitary waves. The next series of experiments were undertaken at JILA [7] using the same ^{85}Rb experiment that had first observed tunable atomic interactions [30] and controlled collapse [35]. This new work concluded that the stable remnant observed previously in the collapse experiments divided into similar solitary wave structures as seen at Rice. Unlike the quasi 1D trapping used in the Rice experiment, the JILA trap remained 3D throughout the cooling and soliton formation stages with radial and axial trap frequencies of 17.3 Hz and 6.8 Hz respectively.

Unlike the ENS and Rice experiments, the JILA apparatus used a purely magnetic trap, however, the method of creating solitary waves by modifying the scattering length can be considered an inherently similar process. After producing condensates of up to 15,000 atoms at $a_s > 0$ the magnetic field was adiabatically ramped to decrease the scattering length to $a_s = 9a_0$. To initiate the collapse, the field and hence scattering length, was then jumped rapidly (0.1 ms) from positive to negative, to a_{collapse}. Following some time at the final scattering length, t_{evolve}, the atoms were destructively imaged following the turn off of the trap. Investigating the collapse process as a function of a_{collapse} and the initial condensate number, N_0, it was clear that the number of condensate atoms surviving the collapse could, in the right conditions, greatly exceed N_{critical}. The fraction remaining was found to vary dramatically, from around 60 % at $-5a_0$ to as little as 30 % at $-50a_0$. Notably, the lifetime of the stable remnant could be as long as several seconds.

Observations of the condensate size in the trap as a function of time suggested a highly excited state had been produced during the collapse, with the remnant cloud's width doubling in size during its oscillation in the trap. However, further analysis revealed that, as in the Rice experiment, multiple solitary waves were being created which oscillated back and forth along the weak axial direction of the trap. The wavepackets were observed to persist in the trap for ~ 3 s, undergoing as many as 40 collisions in this time. This provided additional experimental data to accompany the Rice experiments and the growing body of theoretical work examining solitary wave stability. The number of solitary waves created in the ^{85}Rb collapse experiment was found to be controllable, to a degree, depending on a_{collapse} and N_0. As expected, N_s increased with $|a_{\text{collapse}}|$. Importantly, the number of atoms observed in

any one solitary wave was never found to exceed N_{critical}.

7.1.2 Open questions: Validity of the GPE description and the role of relative phase

In two of the previous three experiments multiple wavepackets were created, allowing the study of the collision dynamics in the trap. The long lived nature of the solitary waves and their apparent stability during binary collisions has been the subject of much theoretical interest [74, 8, 63, 9, 10]. Central to this work is the role of relative phase.

Within the framework of the GPE, the observed stability of solitary wave collisions seen in previous experiments [5, 7] can only be explained by imposing a relative phase between neighbouring solitary waves such that the collisions are effectively repulsive in character. Parker *et al.* found this phase to be $\phi = \pi$ [41] whereas Carr *et al.* observed stability for a range of phases $\pi/2 < \phi < 3\pi/2$ [9]. In the absence of this phase, $\phi = 0$, the increase in density as the wavepackets overlap causes a collapse and the subsequent destruction of the solitary wave pair. For intermediate phases, $0 < \phi < \pi$, the same GPE model used by Parker *et al.* predicts population transfer during the collision [41] with the velocity of the two incoming wavepackets playing a key role in the fraction of atoms transfered.

Although these GPE simulations successfully reproduce the behaviour and stability of multiple wavepackets undergoing collisions previously observed, the same results have been reported without the need for the GPE imposed phase. Instead, the inclusion of quantum fluctuations [10] is sufficient to render all collisions repulsive, irrespective of phase. However, this is limited to 1D simulations, modelling a system similar to the Rice experiment. When extended to 3D, a closer description of the JILA experiment, the inclusion of 3D quantum noise has a negative impact on the lifetime of the bright solitary matter-waves. As such, the length of time for which the solitary waves were observed to persist experimentally cannot be reproduced.

Despite the phase independence of collisions in 1D shown by Dabrowska-Wüster *et al.* [10], they find there is insufficient evidence to suggest that

quantum noise effects are the correct interpretation of experimental results and indeed their 3D simulations do not support this theory. However, mean field GPE simulations carried out by the same group also fail to explain the system fully as the symmetry of initial wavefunction precludes the formation of a repulsive relative phase for an even number of wavepackets. This is a result of the mean-field theory which preserves the initial symmetry.

It is of course important to consider that Bose-Einstein condensates are in fact many-body quantum mechanical systems at finite temperature and perhaps the mean-field, zero temperature description given by the GPE may not be capable of providing an explanation of the behaviour observed in experiments. Beyond-mean-field effects (quantum and/or thermal effects) are most commonly described by a stochastic GPE. However, one can also adopt a more fundamental quantum mechanical approach, describing the many-body dynamics via the multiconfigurational time-dependent Hartree method for interacting bosons [190].

Using this Hartree method to explore the dynamics of two solitons, Cederbaum *et al.* [191] found the initial matter-wave trains rapidly lose their coherence, becoming macroscopically fragmented BECs, or 'fragmentons'. This is in obvious contradiction to the results of GPE simulations.

Such a stark contrast between the conclusions regarding relative phase undoubtedly invites further experimental studies [78] as a means of testing theoretical models of quantum many-body systems such as this. Not only will this allow the questions over relative phase to be answered but the next generation of experiments should also provide an insight into whether the GPE is indeed the correct description for the solitary wave dynamics.

7.2 Loading a BEC into the waveguide

To create our single solitary wave we begin by forming a BEC containing up to 10,000 atoms at a scattering length of $a_s \approx 300\ a_0$. The crossed beam trap in which the BEC is created has a roughly spherically symmetric geometry at the point of condensation, with final trap frequencies of $\omega_{x,y,z} = 2\pi \times (31, 27, 25)$ Hz. Unfortunately, this trap is ill-suited to the observation of

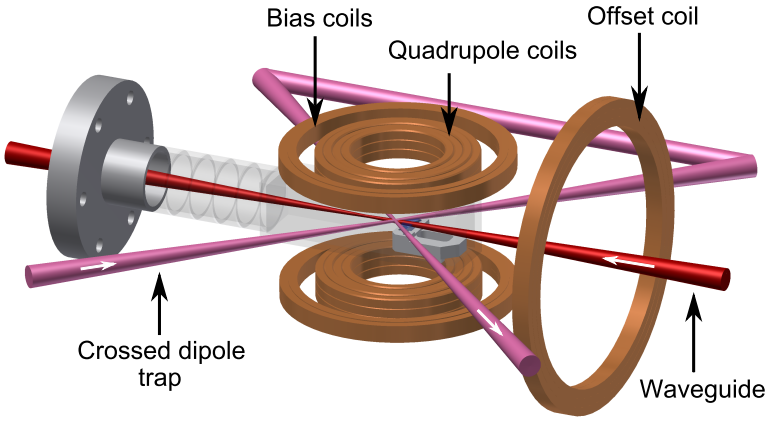

Figure 7.1: Waveguide setup: Experimental setup showing the crossed dipole trap used to create the BEC, the optical waveguide and the quadrupole, bias and offset coils.

bright solitary matter-waves and thus we must transfer the condensate into a more quasi-1D trapping geometry. This geometry is created by an additional 1064 nm laser beam, focused to 117 μm, producing a 1D waveguide which intersects the cross trap at 45° to each beam. This enters the glass science cell through the back surface of the anti-reflection coated fused silica Dove prism as shown in Fig. 7.1.

To load the condensate into the waveguide the scattering length is ramped close to $a_s = 0$ in 50 ms thus reducing the condensate size and creating a BEC approximately in the harmonic oscillator ground state of the cross trap. The BEC is then held for 10 ms to allow the magnetic field to stabilise before simultaneously switching the waveguide beam on, the crossed beams off and jumping the quadrupole gradient from 21.5 Gcm^{-1} to 26 Gcm^{-1}. The change in the magnetic gradient ensures a truer levitation of the atoms in the waveguide trap, thus maximising the trap depth of the beam. In addition, the presence of the quadrupole gradient provides much of the, albeit weak, axial trapping along the beam [91]. At a beam power of 0.17 W the waveguide and quadrupole potential produces a trap of $\omega_{x,y,z} = 2\pi \times (1, 28, 28)$ Hz. Here the radial trap frequency ($\omega_{y,z}$) approximately matches that of the crossed beam trap at the point of condensation. A small offset (2.6 mm) between the crossed dipole trap, i.e. the waveguide loading position, and the quadrupole centre means that once loaded into the waveguide, the BEC propagates freely

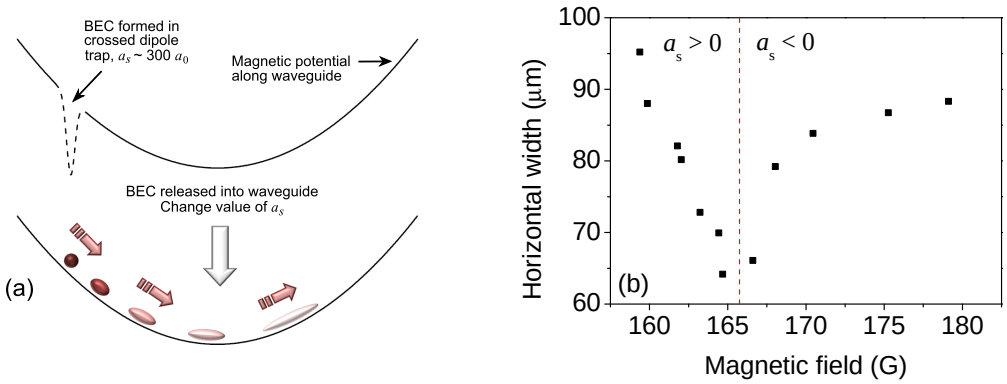

Figure 7.2: Loading the waveguide: (a) Schematic of the release of the condensate from the crossed dipole trap into the waveguide. (b) Cloud size after 50 ms of propagation time in the waveguide. The change in horizontal size with magnetic field suggests the presence of tunable atomic interactions, characteristic of a ^{85}Rb Bose-Einstein condensate. The dotted line marks the position of $a_s = 0$.

towards the minimum of the magnetic potential along the waveguide, undergoing harmonic motion. This is show schematically in Fig. 7.2(a). The application of a small magnetic field along the axis of the waveguide as in chapter 4, shifting the quadrupole field zero (and therefore the location of the minimum of the magnetic potential), allows this offset to be changed and hence the amplitude and velocity of the atoms' motion to be precisely controlled [45].

7.2.1 Tunable BEC in the waveguide

At the point of release into the waveguide, the magnetic bias field controlling the atomic scattering length is also jumped (see Fig. 7.2(a)). To confirm that the transfer into the waveguide does not destroy the condensate, we perform a similar experiment to that described in section 6.6, looking for a signature of tunable atomic interactions. Once the loading into the waveguide is completed, the bias field is jumped to some new value and and condensate allowed to propagate in the waveguide for 50 ms. Before imaging, a 10 ms time of flight stage at zero bias field allows the condensate to expand sufficiently to allow the cloud size to be determined more accurately. A very

coarse scan of the magnetic field and its effect on the condensate width is shown in Fig. 7.2(b). The change in size with field indicates the presence of tunable interactions and confirms that, despite the somewhat violent jump in the trapping geometry, the condensate survives the transfer process.

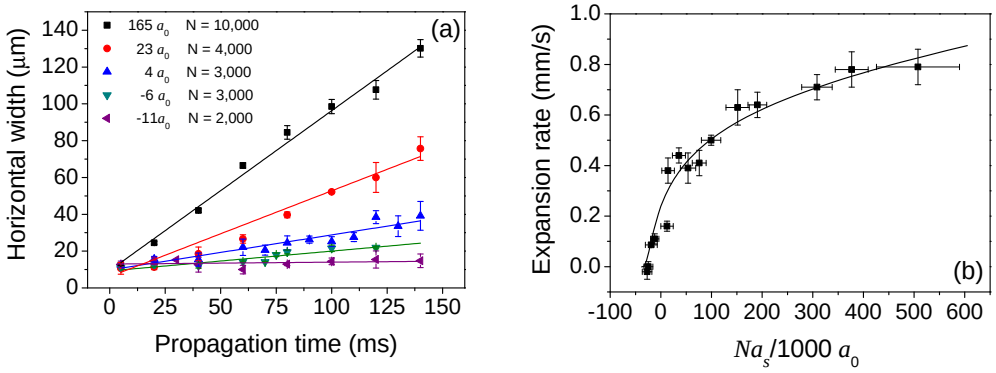

Figure 7.3: Expansion in the waveguide: (a) Condensate expansion in the waveguide for $a_s = 165\ a_0$ (black), 23 a_0 (red), 4 a_0 (blue), -6 a_0 (green) and -11 a_0 (purple). Widths are rms values extracted from a Gaussian fit to the data. Solid lines are linear fits to the data. (b) Condensate expansion rate in the waveguide as a function of atom number and scattering length. The solid line is the theoretical expansion rate, calculated using a cylindrically symmetric 3D GPE [192].

7.3 Solitary wave formation

As the BEC propagates, the value of a_s determines the rate of expansion of the condensate in the axial direction, along the waveguide. We probe this expansion rate[1] by measuring the condensate size as a function of propagation time for different values of a_s as shown in Fig. 7.3(a). An rms width σ is extracted by fitting a Gaussian profile, $y = A\exp[-(x-b)^2/2\sigma^2]$, to optical depth crosscuts of the atomic cloud.

[1] Although strictly speaking the expansion is non-linear over the full range of times measured, a linear approximation is valid over the range 10 ms$\lesssim t \lesssim$100 ms from which we can extract this 'rate'.

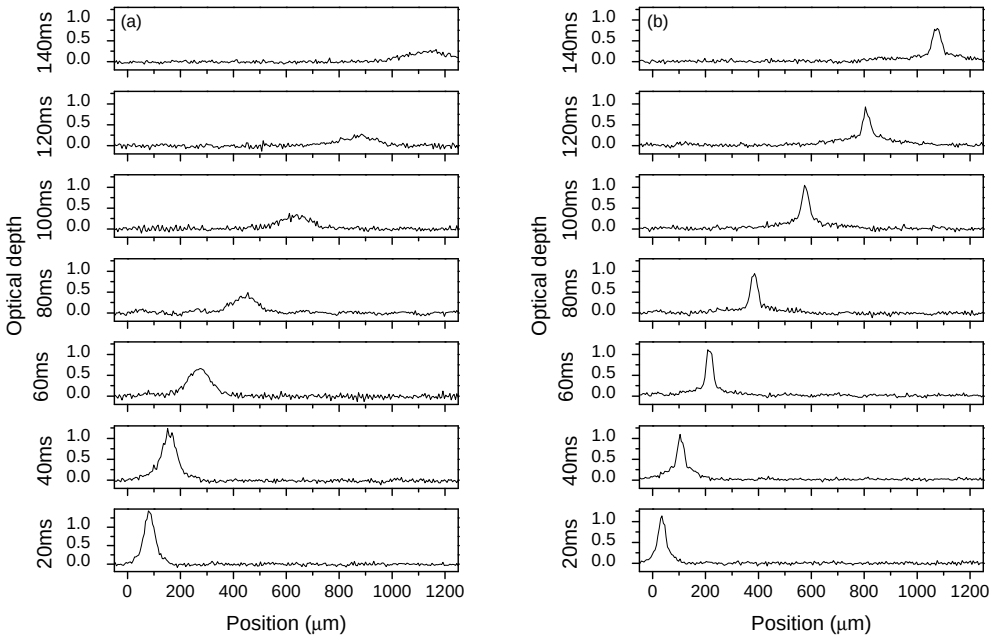

Figure 7.4: Crosscuts of a repulsive BEC and solitary wave propagating in the waveguide: Optical depth crosscuts along the axial direction of the waveguide for multiple propagation times. (a) As a repulsive condensate ($a_s = 58\ a_0$) propagates its width increases as the condensate spreads in the axial direction. (b) As the solitary wave ($a_s = -11\ a_0$) propagates, its width remains constant, the wavepacket being held together by the attractive interactions in the condensate.

Fitting the experimental data in this way, we can extract an expansion rate for the BEC, dependent on a_s and N. This is shown in Fig. 7.3(b). We compare the experimentally determined rate to a 3D cylindrically symmetric GPE simulation of the expansion [192], finding good agreement. At $a_s = -11\ a_0$ and $N = 2000$ we see the expansion of the BEC becomes smaller than the noise associated with determining the cloud width, hence the expansion rate becomes zero. This lack of dispersion with time indicates the formation of a bright solitary matter-wave and is in stark contrast to the propagation of a repulsive condensate, as shown in Fig. 7.4.

Calculating the critical number of atoms for the waveguide geometry ($k = 0.675$) and $a_s = -11\ a_0$ gives a value of $N_c \sim 2300$, consistent with the number of atoms observed in the solitary wave. However, the observed size of the solitary wave in the axial direction $\sigma = 13(3)\ \mu$m is much larger than

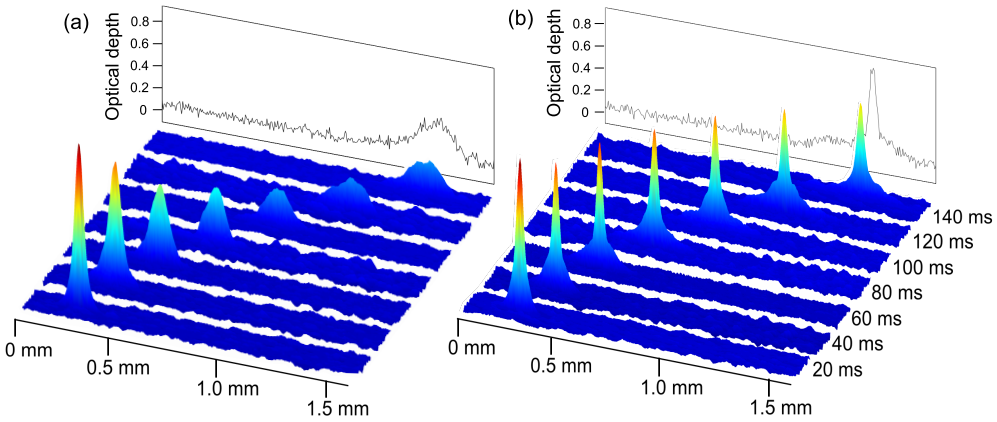

Figure 7.5: Propagation in the waveguide: (a) As a repulsive BEC propagates along the waveguide the atomic interactions allow the condensate to spread, leading to a drop in optical depth. (b) In contrast, the attractive interactions present in a bright solitary matter-wave cause the wavepacket to hold together as it propagates, maintaining its shape with time. Cross-cuts shown are the horizontal optical depth profiles of the condensates after 140 ms propagation time along the waveguide.

the value of ~ 4 μm calculated from Eq. (2.31). In the radial direction, the width $\sigma_r = 8(3)$ μm is again greater than one would expect, this time when compared to the harmonic oscillator length $a_{\mathrm{ho,r}} \approx 2$ μm. This is most likely the result of the limitation of the current imaging system which leaves us unable to resolve and accurately measure objects on the scale of the solitary wave.

7.4 Solitary wave propagation in the waveguide

The experimental signatures associated with solitary wave formation are illustrated again in Fig. 7.5. As a repulsive BEC propagates along the waveguide, the optical depth drops as the condensate spreads in the axial direction (Fig. 7.5(a)). In contrast, no such spreading or significant drop in optical depth is seen for the solitary wave (Fig. 7.5(b)). We observe the single solitary wave propagating over distances of 1.1 mm in a time of ∼150 ms with

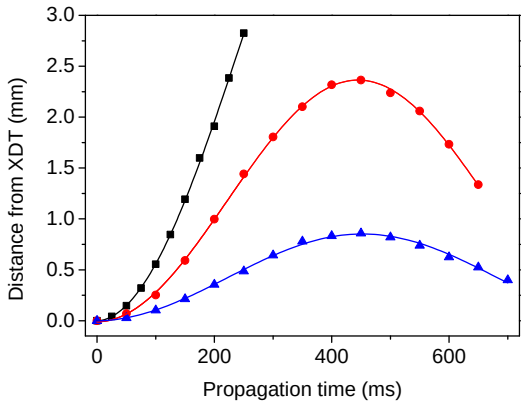

Figure 7.6: Oscillation amplitude in the waveguide: Motion of a cold cloud in the waveguide for three different horizontal bias fields, 0 G (Black squares), ∼2 G (red circles) and ∼5 G (blue triangles) which offset the quadrupole field zero along the axis of the waveguide. By moving the field zero relative to the point of release into the waveguide (i.e. the crossed dipole trap, XDT, position) the amplitude of the oscillation, and hence the velocity, of atoms in the waveguide can be controlled. Sinusoidal fits to the data (solid lines) are used to obtain an estimate of the axial trap frequency and the offset of the quadrupole field zero.

very little distortion. Beyond this, atom loss from the solitary wave becomes appreciable, possibly as a result of moderate heating of the wavepacket due to a radial oscillation in the waveguide.

7.4.1 Oscillation amplitude

The motion of the solitary wave in the waveguide is governed primarily by the weak harmonic confinement along the axial direction of the beam. This is provided by the combination of the quadrupole gradient and the large bias field. (The offset of the field zero due to the bias field creates a large region over which the potential remains harmonic rather than the usual linear shape of the quadrupole (see section 3.3.3)). The amplitude of the solitary wave's motion and its centre is also determined by the quadrupole trap and more specifically the position of the field zero. However, employing the same technique described in section 4.6, it is possible to change the location of this zero point with the application of a moderate bias field along the direction

of the waveguide. Examples of the non-shifted trajectory of atoms in the waveguide, along with two offset cases are show in Fig. 7.6. Fitting a sinusoidal waveform to the data allows the axial frequency of the waveguide to be obtained, $\omega_{\text{axial}} = 2\pi\times1.0(1)$ Hz, along with the position of the field zero relative to the crossed dipole trap position, an offset of 2.6 mm.

Fortuitously, the way in which the contributing fields add (in quadrature) leaves the overall bias field relatively insensitive to this offset field. We can think of the contribution to the field in two ways. In the first we consider the change in field due to the magnetic gradient along the direction of the waveguide (13 Gcm^{-1}) for a cloud initially displaced by 2.6 mm, moving to the minimum of the potential. This gives a change in field of 3.4 G. When added in quadrature to a 165 G bias field the total field is only increased to 165.03 G. Alternatively we can consider the energy associated with the harmonic motion in the trap being transfered into magnetic potential energy, $\frac{1}{2}m\omega^2\Delta x^2 = \mu B$. For a 1 Hz trap and the same 2.6 mm displacement this analysis also yields a 0.03 G change in field. Close to the zero crossing of the Feshbach resonance this translates into a change in scattering length on the order of a_0.

This uniformity in the field has important implications in potential future experiments. For example, for small fields it allows one to control the velocity of a solitary wave without the continual need to compensate for the effect of the additional offset bias field on the scattering length. An unfortunate quirk of our current experimental setup means that for large fields this is no longer true. Due to spatial constraints we can only apply a horizontal bias field from a single coil rather than the more traditional pair configuration. This has the effect of causing a magnetic field gradient along the length of the waveguide, complicating the process. However, with an equally matched, on axis coil pair this problem can be readily addressed.

7.4.2 Velocity control

For future experiments (see chapter 8) where the velocity of a solitary wave incident on a barrier will need to be precisely controlled, the ability to tune the offset between the trap centre and the barrier is of huge importance.

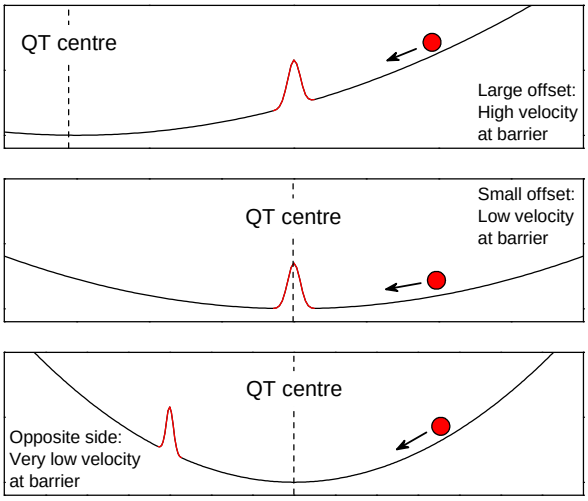

Figure 7.7: Adjustable offset between the quadrupole trap centre and barrier potential: The application of a small bias field allows the quadrupole trap centre to be shifted with respect to the waveguide loading point and any barrier potentials used in the experimental setup. In this way the velocity of the solitary wave can be tuned, most importantly during collisions.

Changing the distance between the release point of the atoms into the waveguide and the quadrupole trap centre affects the amplitude of the motion and hence the velocity of the wavepacket. As shown in Fig. 7.7, little or no offset between the quadrupole trap and the starting position results in low incident velocities at the barrier. In contrast, increasing the offset allows the atoms to gain more momentum before reaching the barrier. In the current (non-shifted) configuration an offset of 2.6 mm between the release point and the quadrupole field zero results in a maximum velocity of $\sim$17 mms^{-1} as atoms pass through the trap centre.

If we assume the case of a narrow barrier, that is we can neglect the effect of the potential on the solitary wave's motion in the trap as it approaches the barrier position, we can calculate an estimate for the solitary wave velocity at the barrier. The position of the wavepacket is given by

$$x(t) = x_c + (x_s - x_c)\cos(\omega t), \tag{7.1}$$

where x_c is the location of the quadrupole trap centre and x_s is the starting position for the solitary wave (i.e. the crossed dipole trap position). If we

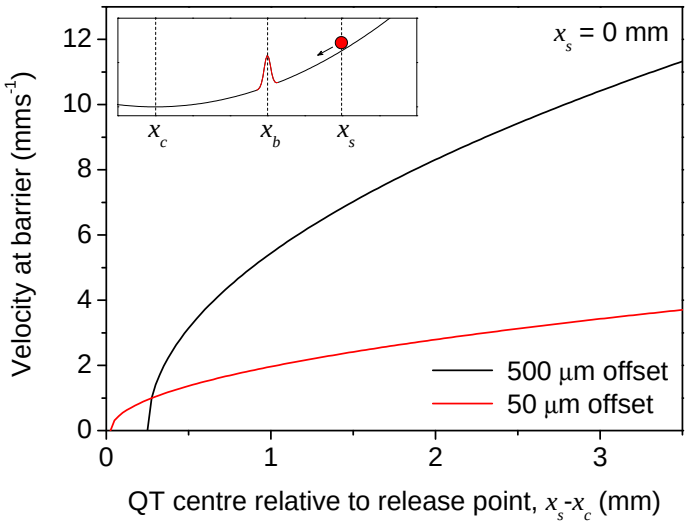

Figure 7.8: Solitary wave velocity at a narrow barrier: Velocity at the barrier as a function of the separation between the release point x_s and the quadrupole trap centre x_c for barriers placed 500 μm and 50 μm from x_s.

then set $x = x_b$, where x_b is the barrier position, Eq. (7.1) becomes,

$$\frac{x_b - x_c}{x_s - x_c} = \cos(\omega t). \tag{7.2}$$

Differentiating Eq. (7.1) yields an expression for the velocity,

$$\begin{aligned} v &= -\omega(x_s - x_c)\sin(\omega t) \\ &= -\omega(x_s - x_c)(1 - \cos^2(\omega t))^{1/2}. \end{aligned} \tag{7.3}$$

Substituting Eq. (7.2) into Eq. (7.3) we have,

$$v = -\omega(x_s - x_c)\left(1 - \left[\frac{x_b - x_c}{x_s - x_c}\right]^2\right)^{1/2}. \tag{7.4}$$

This velocity is plotted as a function of the quadrupole trap position for two fixed barrier locations in Fig. 7.8. By placing the barrier and quadrupole trap centre close to the initial start position it should therefore be possible to achieve incident velocities on the order of a few mms^{-1}. Moreover, placing the trap minimum between the barrier and the release point allows velocities approaching zero to be realised (see lower panel of Fig. 7.7).

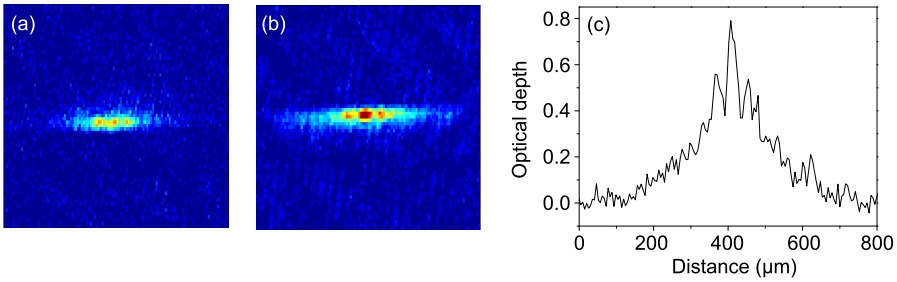

Figure 7.9: Multiple solitary wave formation: (a) and (b) False colour images of multiple solitary wave creation. (c) Optical depth crosscut of image (b) showing three distinct peaks in the horizontal profile.

7.5 Multiple solitary wave formation

In almost all cases, a single solitary wave is formed during the experimental cycle. However, on a small number of occasions, multiple wavepackets have been observed in the waveguide. We attribute this to small, uncontrollable fluctuations in either atom number or scattering length affecting the stability of the condensate, ultimately leading to collapse. Example images are shown in Fig. 7.9. Notably, the separate solitary waves tend to differ in size more so than those observed previously at JILA [7]. Usually one central, large solitary wave is formed, flanked by a number of smaller wavepackets. Implementing the same experimental protocol as outlined in [5], releasing the BEC into the waveguide and waiting some time before jumping the scattering length, fails to reliably produce multiple solitary waves, although this has not be explored extensively.

7.6 Reflection from a wide repulsive Gaussian barrier

To further probe the stability of the solitary wave we investigate the effect of a collision with a repulsive Gaussian barrier. This allows us to gain insight into the suitability of solitary waves for future applications such as the study of short-range atom-surface interactions and quantum reflection.

7.6.1 Experimental implementation

To produce the repulsive potential we use a 532 nm Gaussian beam (Laser Quantum Finesse), focused using a cylindrical lens to 131 μm horizontally and 495 μm vertically with a typical power of 1.75 W. The barrier is aligned to cross the waveguide in the horizontal plane at an angle of $\sim$45° and is offset by $\sim$335 μm from where the BEC is released from the crossed dipole trap. In the ideal case the barrier would be orientated perpendicular to the direction of propagation along the waveguide, however, the input angle of the beam is restricted by the available optical access close to the dipole trap centre.

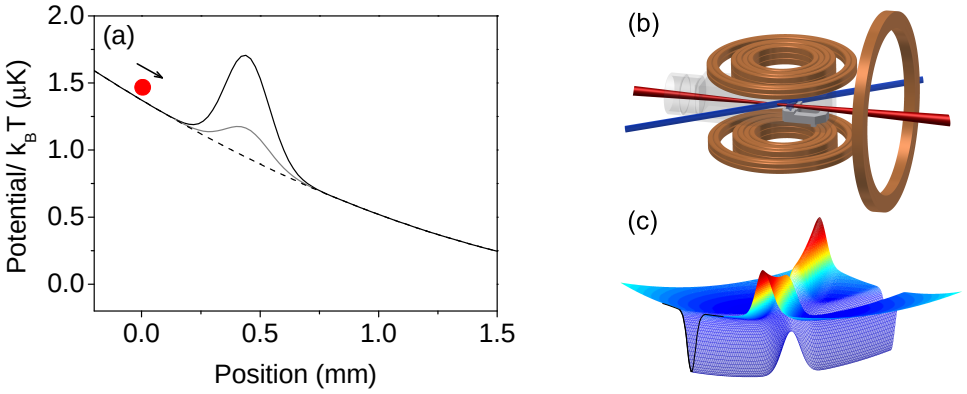

Figure 7.10: Barrier potential: (a) Potential in the axial direction along the waveguide in the presence of the repulsive barrier. (b) Experimental setup. The barrier beam is positioned such that it intersects the waveguide at 45°. (c) Combined waveguide and Gaussian barrier potential.

7.6.2 Observation of classical reflection

As demonstrated in section 7.4, in the absence of a repulsive barrier a solitary wave propagates along the waveguide with negligible dispersion. With the addition of the 532 nm barrier, the motion is halted some way along the waveguide before the direction of travel is reversed. Figure 7.11 shows the horizontal centre of a solitary wave in these two cases. If left for sufficient time, atoms held in the waveguide will continue to propagate back and forth, undergoing many oscillations between the newly imposed boundary

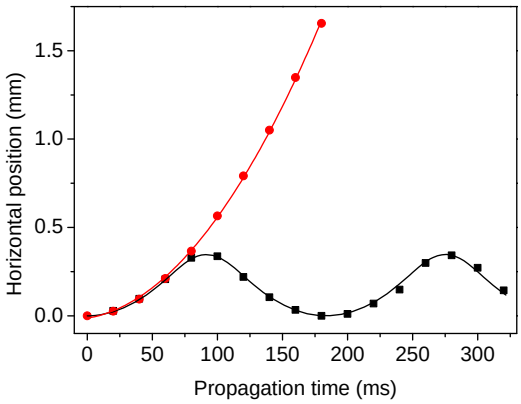

Figure 7.11: Horizontal centre of a solitary wave as a function of propagation time in the waveguide: If allowed to propagate freely (red circles) the solitary wave trajectory is the same as that of an atom in a harmonic potential. In the presence of the barrier (black squares) the amplitude of the motion is greatly reduced and the solitary wave oscillates between the barrier position and the release point.

conditions; the barrier and the release point.

7.6.3 Effect of a barrier on solitary wave motion

In the initial experiment described in section 7.6.2 a power of 1.75 W was used to form the repulsive barrier (height $|U| \sim 0.52$ μK). Although a freely propagating solitary wave would have sufficient kinetic energy at the position of the barrier to overcome the repulsive potential, the wavepacket experiences a slowing force as it approaches the beam. The result is that a much energetically smaller barrier is needed to reflect the solitary wave than one may predict from consideration of only the free propagation. By tuning the power of the barrier it is possible to control whether the solitary wave is able to propagate over and to the other side of the barrier or whether it is reflected back towards the release point.

The solitary wave position for a given time can be calculated from a simple consideration of $F = ma$ where contributions to the force come from the harmonic waveguide and the repulsive barrier. Starting from the harmonic

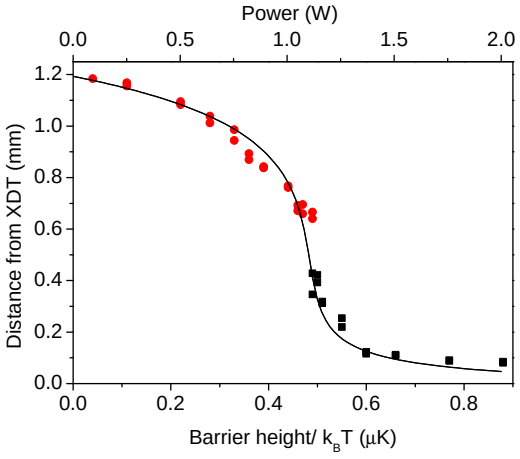

Figure 7.12: Position of a solitary wave after 150 ms expansion time in the waveguide as a function of barrier height: At sufficiently low power (red circles) the solitary wave is able to travel over the barrier. As the power is increased and the barrier height increases, the solitary wave slows before eventually being reflected from the repulsive potential (black squares). The solid line shows the solution to Eq. 7.7 modelled using only experimentally measured parameters.

and repulsive barrier potentials,

$$U_{\text{harmonic}} = \frac{1}{2}m\omega^2 x^2, \tag{7.5}$$

$$U_{\text{barrier}} = -\frac{2P\beta}{\pi w_x w_y} e^{\frac{-2(x-x_0)^2}{\sigma^2}}, \tag{7.6}$$

it is possible to extract an expression for the total force experienced by each atom,

$$F = m\ddot{x} = -m\omega^2 x - \frac{8P\beta}{\pi w_x w_y \sigma^2}(x - x_0)e^{\frac{-2(x-x_0)^2}{\sigma^2}}. \tag{7.7}$$

Here, ω is the harmonic trap frequency, P the power of the 532 nm beam, β accounts for the polarizability of the atom at 532 nm ($\sim -196.8\ a_0^3$ in atomic units [93]), w_x and w_y are the beam waists horizontally and vertically, σ is the horizontal barrier width 'seen' by the atoms (accounting for the angle of incidence) and x_0 is the distance between the harmonic trap centre and the barrier. Solving this expression numerically as a function of barrier height, one can plot the solitary wave position after a given propagation time (150 ms). This is shown as the solid line in Fig. 7.12. Note, no free parameters are used in the model, rather they have been experimentally

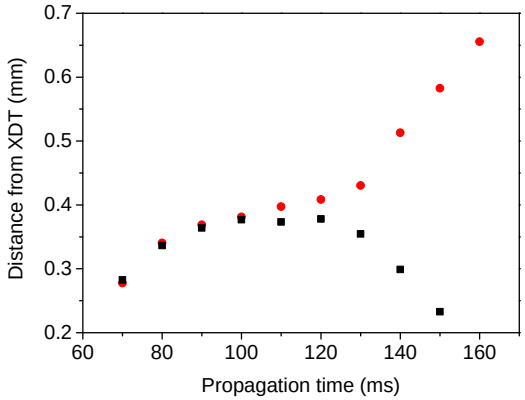

Figure 7.13: Control of solitary wave velocity using a repulsive barrier: By setting the barrier close to that needed to halt the solitary wave's motion it is possible to observe considerable slowing of the wavepacket. At a power of 1.11 W (red circles) the solitary wave is temporarily slowed close to the barrier but eventually makes it over, continuing to propagate along the waveguide. Only a small increase in power to 1.15 W is sufficient to reflect the solitary wave back towards the release point (black squares).

measured or extracted from fits to data.

Figure 7.12 also shows the experimentally measured position of the solitary wave 150 ms after release from the crossed trap. The points in red correspond to the solitary wave successfully traversing the barrier and making it to the other side. The black points are for solitary waves reflected backwards. The final positions are of course governed by the velocity of the wavepacket, this being partially determined by the repulsion due to the barrier.

Again using Eq. (7.7), this time to obtain an expression for velocity rather than position, it is possible to determine the barrier power required to theoretically bring the cloud to a standstill at the position of the barrier. Although experimentally it is difficult to completely stop and hold the solitary wave at the barrier, close to the required power, it is possible to observe considerable slowing down of the solitary wave as shown in Fig. 7.13. A slight increase in power then causes reflection.

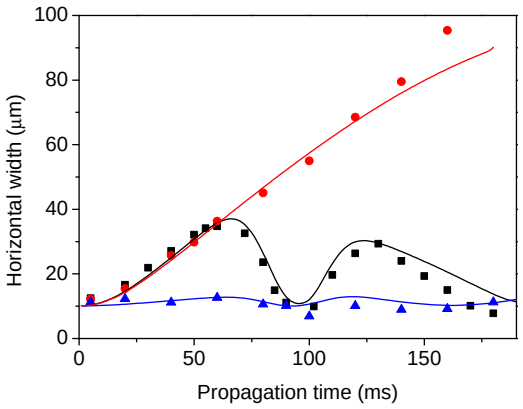

Figure 7.14: Condensate width following a collision with a repulsive barrier: In the absence of a barrier, a repulsive BEC will expand as it propagates (red circles). With the barrier in place, an oscillation in the width is set up following the reflection due to the compression of the condensate at the barrier (black squares). The trapping potential created by the waveguide and barrier restricts the expansion of the condensate causing the repeated compression of the cloud. Conversely, a solitary wave undergoing the same collision emerges unaltered (blue triangles). Solid lines are the theoretical condensate widths calculated by solving the 3D (cylindrically symmetric) GPE [192].

7.6.4 Effect of a barrier collision on solitary wave width

A key signature of bright solitary matter-waves is their robustness, emerging unchanged from collisions with other solitary waves and with external potentials. Using the repulsive Gaussian potential it is possible to test this, examining the width of the solitary wave both before and after the reflection.

Again using a barrier power of 1.75 W (∼520 nK) we allow a solitary wave ($a_s = -12\ a_0$, $N = 2 \times 10^3$) to propagate along the waveguide, colliding with the barrier. We then compare the observed solitary wave size to that of a repulsive BEC ($a_s = +57.5\ a_0$, $N = 4 \times 10^3$) colliding with the same barrier and a repulsive BEC propagating unobstructed ($a_s = +57.5\ a_0$, $N = 3.5 \times 10^3$). The horizontal condensate widths in each of the three cases are shown in Fig. 7.14.

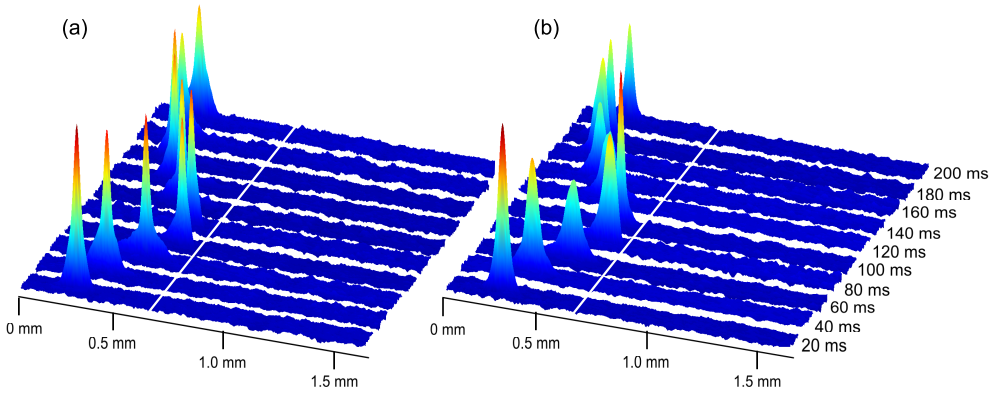

Figure 7.15: 3D images of solitary wave and repulsive BEC collisions with a barrier: (a) As expected, very little change is observed in the width of a solitary wave colliding with the barrier. (b) Conversely, a repulsive BEC incident on the barrier begins to undergo oscillations in its width. As the cloud narrows as it hits the barrier there is a corresponding increase in optical depth. Following the reflection the BEC begins to spread again, this cycle of expansion and contraction continuing with time. White lines show the approximate barrier position.

As expected, the solitary wave width is unaffected by the collision. This is not the case for the repulsive condensate. Prior to the collision, the condensate expands as in the unobstructed case, however once the barrier is hit, the expansion is halted. Instead an oscillation in the condensate width is set up. This arises because of the spatial extent of the condensate causing it to be strongly compressed at the turning point. This change in width can be seen again in Fig. 7.15. A narrowing of the repulsive condensate width is accompanied with an increase in optical depth as atoms pile up in a smaller volume.

7.7 Summary

In this chapter we have shown it is possible to transfer a Bose-Einstein condensate between two different trapping geometries. We begin with the condensate in the crossed dipole trap before loading it into a quasi-1D waveguide. Once here, we are able to tune the atomic scattering length thus controlling

the expansion of the condensate in the waveguide. We compare the expansion rate with a theoretical simulation, finding good agreement between the two.

By making the interactions sufficiently attractive we are able to demonstrate the formation of a bright solitary matter-wave from the ^{85}Rb condensate. The solitary wave is observed to propagate a distance of $\sim$1.1 mm in the optical waveguide in 150 ms without dispersion.

Using a broad, repulsive, Gaussian barrier we explore the classical reflection of a solitary wave and a repulsive condensate. Following the reflection an oscillation in the width of a repulsive condensate it set up as a result of compression at the turning point. In contrast to this, the solitary wave is found to reflect cleanly from the barrier, maintaining its width following the reflection. Although these are only very preliminary results, the nature of the reflection of the solitary wave from the wide Gaussian barrier illustrates the superiority of these attractive condensates for use in reflection experiments such as those to be described in chapter 8.

Chapter 8

Conclusions and outlook

In this thesis we have demonstrated the formation of bright solitary matter-waves from a ^{85}Rb Bose-Einstein condensate. Using a magnetic Feshbach resonance to manipulate the atomic scattering properties, we are able to create a BEC with tunable interactions and to form solitary waves by switching the interactions from repulsive to attractive.

In order to access the magnetic Feshbach resonance we choose to work with a crossed optical dipole trap. This has an advantage over a magnetic trap in that the radial trap frequencies are insensitive to any applied bias fields. We began by exploring the simplest case of optical trapping, a single laser beam used in conjunction with a magnetic quadrupole trap to produce a hybrid single beam trap. We characterised this system using ^{87}Rb and demonstrated that, with the application of a moderate bias field to displace the quadrupole trap centre, atoms can be transported over distances of several millimetres along the length of the laser beam. In this first trap we produced condensates of ^{87}Rb by both direct evaporation and by using a surface to selectively remove the hottest atoms from the trapped cloud.

An unfortunate limitation of this trap showed itself with the application of any significant bias field in the vertical direction. This effectively removes the axial trapping, reducing the trap to a waveguide. In order to access the broad Feshbach resonance in the $F = 2, m_F = -2$ state of ^{85}Rb we need to apply a 155 G magnetic field, hence this trap was no longer suitable. Instead we moved to a crossed beam trap, using more power and larger

beam waists to create a larger volume trap. Again we initially characterised the system using ^{87}Rb for convenience, exploiting its low inelastic loss rates. We demonstrated that three distinct trapping configurations may be realised using a combination of laser light, magnetic fields and magnetic gradients. In each of these traps we again produced condensates of ^{87}Rb. By virtue of the trapping geometry we were also able to form a 1D optical lattice and performed some basic manipulations of a condensate produced in the lattice.

With the crossed trap fully characterised we turned our attention to the trapping and cooling of ^{85}Rb. Using a combination of the hybrid crossed dipole trap and a levitated trap (produced with the application of a magnetic bias field) we exploited the variation of both the elastic and inelastic scattering properties close to the 155 G Feshbach resonance to efficiently evaporate to degeneracy. We demonstrated the tunable nature of the atomic interactions in the condensate and observed the collapse phenomenon associated with attractive BECs.

Finally we described the transfer of the condensate from the 3D crossed trap to a quasi-1D waveguide. Once here we again tuned the s-wave scattering length of the atoms, this time to control the expansion of the condensate in the waveguide. In doing so we created a bright solitary matter-wave. We observed the propagation of the solitary wave in the waveguide, finding negligible dispersion over a distance of $\sim$1.1 mm. We demonstrated the particle like nature of the solitary wave via a classical reflection experiment from a repulsive Gaussian barrier produced by a blue detuned laser beam. As we expected, the solitary wave reflected cleanly from the barrier and we contrasted this to the case of a repulsive condensate where an oscillation in the radial width was set up following the reflection.

8.1 Future work

Following the successful realisation of a bright solitary matter-wave we immediately turn our attention to the plethora of exciting and potentially insightful experiments ahead.

8.1.1 Reflection from a narrow barrier

The first, and most obvious, avenue to investigate is to extend the preliminary reflection experiment described in chapter 7. Although a wide barrier allows the study of classical reflection, to observe quantum effects a barrier waist on the order of, or less than, the solitary wave width is required. When aligned to be in the path of the propagating soliton, the barrier then appears as a rapid variation in the waveguide potential; for a repulsive barrier as a hump along the waveguide and for an attractive barrier as a step down (or potential well).

Repulsive barriers

At high kinetic energy soliton splitting is energetically allowed at narrow *repulsive* barriers within the formalism of the GPE. The effect of quantum tunnelling means the barrier can act as a beam splitter, dividing the soliton into two parts. These multiple wavepackets can then be used to investigate the phase dependence of binary collisions [78], the effect of collisions of two solitary waves on a barrier [193] and would provide a solid first step towards the realisation of a bright solitary wave interferometer [194, 4]. Work to study this type of splitting is currently underway in the Hulet group (Rice, Texas) using solitary waves formed from ^{7}Li condensates [195].

In the limit of low kinetic energy, a mean-field GPE treatment of the problem begins to break down [196] and quantum behaviour, described by the Lieb-Liniger Hamiltonian [197], becomes more significant. Here, splitting of the soliton is energetically forbidden and it becomes possible to create Schrödinger-cat states [198, 199] where the effect of the barrier is to create a superposition of one soliton containing all the atoms being simultaneously on both sides of the barrier at once.

Attractive barriers

For the case of a slow soliton incident on an *attractive* potential well, reflection, transmission, and trapping of the soliton are predicted [200], strongly dependent on the well's depth. Importantly it is the level structure of the

well which leads to the formation of quasi-bound states causing the trapping of the soliton. As such, solitons could be used to experimentally probe bound states of an unknown localized potential well using this sort of scattering.

8.1.2 Controlled formation of soliton pairs via tuning of the *s*-wave scattering length

As an alternative to the barrier splitting methods described previously, careful tuning of the scattering length has been proposed as a controlled way in which to create soliton, or solitary wave pairs [201]. In this scheme a condensate with *large repulsive* interactions is first created in the centre of a shallow trap. This causes the cloud to spread by virtue of the strong internal repulsion. Once the cloud becomes sufficiently large, the interactions are then switched from repulsive to attractive using a Feshbach resonance. This should produce a pair of solitons, as the result of modulational instability [9], moving with opposite velocities away from each other in the trap. Importantly the precise switching of the scattering length should yield full control over the splitting process.

8.1.3 Investigating phase dependence of binary solitary wave collisions

Using a narrow barrier or tuning of the scattering length to controllably create two solitary waves provides an ideal starting point for the investigation of solitary wave collisions. Once formed the two separate wavepackets can be spatially separated thus allowing a relative phase to be imprinted between the two.

Considering the many competing theoretical models of the formation and dynamics of solitary waves (discussed in section 7.1.2) the ability to probe the effect of relative phase on the stability of collisions is of obvious value. The observation of population transfer predicted in Refs. [41] and [78] would also be a conclusive test of the GPE. Potentially experiments such as these could then help settle the debate over the correct description of these quantum many-body systems.

8.1.4 Beyond mean field effects

Consideration of beyond mean field effects also predicts a number of interesting phenomena which raise yet more questions about the nature of the solitary waves observed in experiments. Many-body calculations by Streltsov *et al.* [42] result in the emergence of 'fragmentons', objects combining macroscopic fragmentation of the wavefunction and the dynamical properties of a soliton. Unlike solitons these fragmentons are not coherent objects. Found to form even when the production of a two soliton train from the initial state is energetically forbidden, fragmentons arise as excited states of the quantum many-body system become energetically accessible. This would therefore suggest the existence of a new kind of low lying excited state which is unavailable within the framework of the GPE.

Results such as this cast doubt over whether the Gross-Pitaevskii formalism is indeed the correct description of the system, not only for the particular case of an attractive 1D Bose gas investigated in [42], but in a more general sense.

8.1.5 Bose-Einstein condensation close to a surface

Short range atom-surface interactions

Although reflection and splitting experiments with narrow barriers show the potential to settle the theoretical debate over solitary wave formation and dynamics, the ability to probe such narrow and hence rapidly varying potentials using these wavepackets also lends itself to an obvious application in precision measurement.

Atoms close to a surface are subject to the short-range Casimir-Polder and van der Waals potentials. This results in an attractive potential between the atom and the surface in question. As highlighted in chapter 4, loading precisely tailored surface traps or lattices, positioning atoms only a few microns from the surface, allows one to test a number of novel schemes to measure the atom-surface potential, including interferometry in a double-well potential [140] and the study of Bloch oscillations [141].

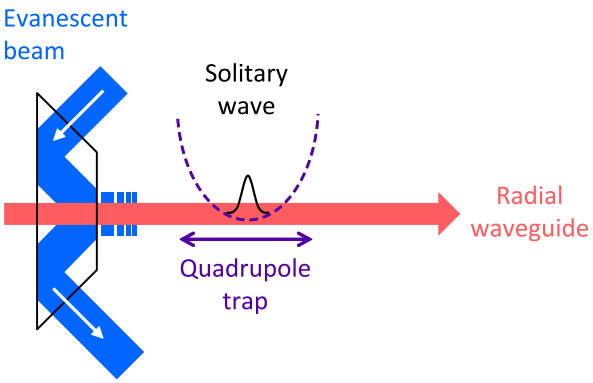

Figure 8.1: Schematic of the experimental setup proposed for the study of atom-surface interactions and quantum reflection: Solitary waves are guided towards the prism surface along a waveguide formed from a 1064 nm laser beam. The position of the solitary wave and its velocity is determined by a magnetic quadrupole trap used to provide weak magnetic confinement along the waveguide. An optional evanescent wave potential can be produced through total internal reflection of a 532 nm laser beam inside the prism.

As described in chapter 3, the apparatus presented here includes a super-polished Dove prism suitable for atom-surface experiments. The geometry of the prism is such that an additional (blue detuned) laser beam can be used to produce a repulsive, evanescent mirror at the front surface of the prism as shown in Fig 8.1. In this way the net potential experienced by the atoms approaching the surface can be tuned from attractive to repulsive, as shown in Fig. 8.2, through control of the laser power. This presents the opportunity to observe both classical [128, 202] and quantum reflection from the surface [203], allowing information about the short-range atom-surface potential to be extracted. Theoretical work [3] suggests that solitary waves should prove a superior tool for such experiments, enhancing the precision obtainable with ultracold gases or large, repulsive BECs seen in previous work [119].

Quantum reflection from a surface

The classically counterintuitive phenomenon of quantum reflection results in the reflection of a matter-wave from an attractive potential and reinforces

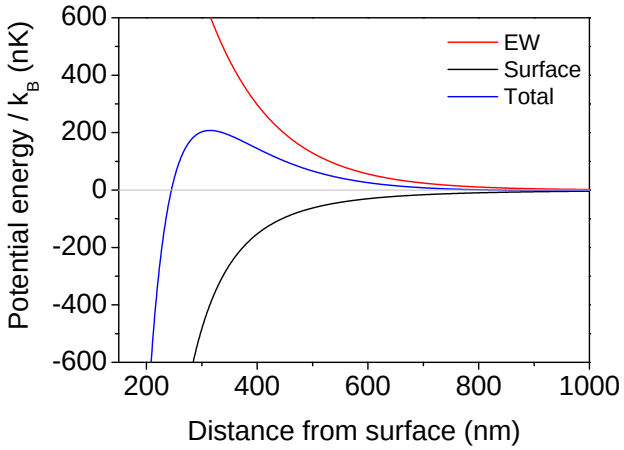

Figure 8.2: Atom-surface potential: At short range, the atom-surface interaction is dominated by the attractive van der Waals (vdW) and Casimir-Polder (CP) potentials. However, the use of an evanescent wave (EW) potential can be used to overcome this interaction, the result being a tunable potential close to the surface. With sufficient power in the EW laser beam a repulsive barrier can be created allowing one to examine both classical and quantum reflection. The example shown here is for λ_{EW} =532 nm light (I =85 MWm^{-2}) incident on the prism surface ($n = 1.5$) at 45° .

the description of atoms as wave-like objects.

Quantum reflection requires a rapid variation in the local wavevector k such that k varies within the deBroglie wavelength by more than k itself,

$$\frac{1}{k^2}\frac{dk}{dr} > 1. \tag{8.1}$$

In the vicinity of a surface the local wavevector is given by [204]

$$k = \sqrt{\frac{k_0^2 - 2mU_{\text{int}}}{\hbar^2}}. \tag{8.2}$$

Here $k_0 = mv/\hbar$ is the wavevector perpendicular to the surface far away (i.e. $r \to \infty$) and U_{int} is the atom-surface interaction potential.

The probability of reflection has been studied extensively for an atom-surface potential and is given by [205]

$$R \approx 1 - \frac{\beta_4 mv}{\hbar}, \tag{8.3}$$

where $\beta_4 = \sqrt{2mC_4/\hbar^2}$ is the length scale associated with the Casimir-Polder C_4 coefficient. A high reflection probability therefore requires low incident velocity, $v = \hbar k_0/m \to 0$, or weak attraction to the surface. Previous experiments [204, 206, 207, 208] have achieved this using low mass elements such as He and H reflecting from liquid He or through trajectories with only grazing incidence to reduce the component of the velocity normal to the surface.

Although an experiment using a harmonic trap close to a surface [209] has previously been used to observe quantum reflection from a solid surface, the small size and attractive interactions present in a solitary wave should make lower incident velocities attainable and reflection signals cleaner [3].

8.2 Next phase of the experiment

It is likely that experiments discussed in this chapter will ultimately require the modification of our current system. In the new setup a crossed dipole trap constructed from two independent laser beams should offer greater control of the evaporative cooling and, most importantly, the loading of the waveguide.

It is likely that one of the two beams will be delivered through the back surface of the super-polished Dove prism, as the waveguide beam is now. Rather than transferring the condensate from the crossed dipole trap into a separate waveguide, this geometry should allow a smooth release of the condensate into one of the two crossed beams as the intensity of the second is ramped to zero.

In this new design both the quadrupole and crossed dipole traps will also be positioned much closer to the Dove prism surface. This will allow us to use the same guided transport scheme presented in chapter 4, along with the manipulation of the trapping potential discussed in chapter 7, to deliver solitary waves up to the surface with low incident velocities.

8.3 Concluding remarks

The use of narrow barriers to controllably split solitary waves is a vital step towards a greater understanding of solitary waves and their collisional dynamics. Ultimately this will prove an essential stage in the development of a solitary wave interferometer. In the future, the realisation of Schrödinger cat states using solitary waves could open the door to quantum enhanced interferometry, where the conventional bounds of precision of measurements, such as the shot noise limit or the standard quantum limit, might be beaten [210].

Arguably the most exciting prospect for bright solitary matter-waves in the context of this experiment is their use as probes of atom-surface forces. The control and precision offered by this new generation of cold atom experiments promises to revolutionise the way we approach such measurements. Ultimately the ability to measure short-range forces between atoms and surface could lead to the exploration of short-range corrections to gravity and the search for exotic forces beyond the Standard Model.

Appendix A

Off resonance laser frequency stabilization using the Faraday effect

Prior to the realisation of ^{85}Rb BEC it was unclear as to whether direct evaporation in the optical trap would prove a successful method to attain condensation. An alternative approach considered at this time was to use Raman sideband cooling [211] to aid the cooling of the atoms. This method requires a far detuned optical lattice into which the atoms are loaded. As a first step towards the experimental implementation of sideband cooling a laser frequency stabilisation technique using the Faraday effect was developed and characterised, potentially for use in controlling the lattice detuning. The results of this work are published in the paper '*Off resonance laser frequency stabilization using the Faraday effect*', Opt. Lett. **36**, 64 (2011) and presented here.

A.1 Abstract

We present a simple technique for stabilization of a laser frequency off resonance using the Faraday effect in a heated vapour cell with an applied magnetic field. In particular we demonstrate stabilization of a 780 nm laser detuned up to 14 GHz from the ^{85}Rb D_2 $5^2S_{1/2}$ $F = 2$ to $5^2P_{3/2}$ $F' = 3$

transition. Control of the temperature of the vapour cell and the magnitude of the applied magnetic field allows locking ∼6-14 GHz red and blue detuned from the atomic line. We obtain an rms fluctuation of 7 MHz over one hour without stabilization of the cell temperature or magnetic field.

A.2 Introduction

In the field of atomic and molecular physics it is commonplace to require a frequency stabilized or 'locked' laser source. Many established techniques exist for locking close to an atomic resonance (within a Doppler linewidth) including: frequency-modulation spectroscopy [81], polarization spectroscopy [212], dichroic atomic vapour laser locking [213] and Sagnac interferometry [214]. In contrast, schemes for locking away from resonance, that is, greater than twice the Doppler linewidth away, can present more of an obstacle. Nevertheless, in many instances it is desirable to be detuned by more than 1 GHz from resonance. This is particularly important in experiments using two photon or Raman transitions where population of the intermediate state should be avoided. Examples include Raman cooling [215] and two photon excitation of Rydberg states [216]. It is also common to manipulate ultracold atoms in optical lattices formed using laser fields detuned many GHz from resonance. Applications of such lattices include degenerate Raman sideband cooling (DRSC) [211] and the study of quantum accelerator modes [217].

A common approach for locking off resonance is to employ a second laser, slaved in some way to a reference laser which is locked on resonance. For example, an electro-optic modulator can be used to produce off resonant sidebands on the reference laser which are then used to seed the slave laser [218]. Alternatively, a beat measurement can be used to stabilize the frequency difference between the slave and reference lasers [219]. In a similar fashion, an optical cavity can be used to bridge the frequency gap between the two lasers [220, 221]. However, the experimental complexity of these approaches means that realising their full potential can be technically challenging, especially for larger detunings. Here we present a simple alternative based upon the Faraday effect in a heated vapour cell with an applied magnetic field which allows locking 6-14 GHz (red and blue) detuned from an atomic line without

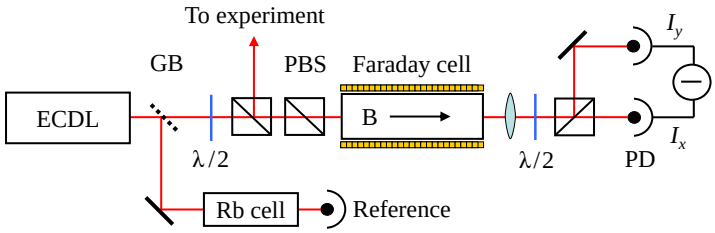

Figure A.1: Schematic of the experimental apparatus used to obtain the Faraday signal: ECDL: external cavity diode laser, GB: glass blank, PBS: polarizing beam splitter, PD: differencing photodiode.

the need for a second laser.

The Faraday effect is a magneto-optical phenomenon. A magnetic field applied along the direction of light propagation causes the medium involved to respond differently to left and right circularly polarized light as the field shifts the σ transitions. The result of this circular birefringence is a rotation of linearly polarized light entering the medium due to the phase shift accumulated between its circular components. A key example of where this effect can be exploited is in optical isolators. A similar dispersive response to that exhibited by the isolator crystal can be seen in atomic media.

In previous work the Faraday effect has been applied to produce a narrowband optical filter or 'Faraday filter' [222] and, more recently, in a slow light medium to produce a gigahertz-bandwidth atomic probe [223]. Here we present a technique which uses the Faraday effect in a heated cell to lock off resonance from an atomic transition using that same transition. We consider the specific case of red detuning >10 GHz from the 780 nm ^{85}Rb D_2 $5^2S_{1/2}$ $F = 2$ to $5^2P_{3/2}$ $F' = 3$ transition in order to perform degenerate Raman sideband cooling on ultracold atoms in the $F = 2$ ground state.

A.3 Experimental setup

We use the setup shown in Fig. A.1 to produce the Faraday signal. Light is derived from a homebuilt 780 nm external cavity diode laser (based upon a Roithner Lasertechnik RLT 780-150 GS laser diode). The design incorporates current feed forward circuitry which allows the current to be modulated (with

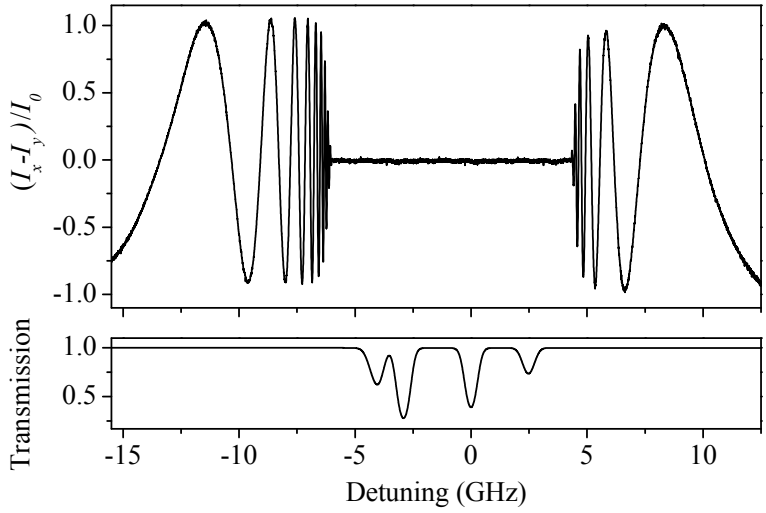

Figure A.2: Normalized Faraday signal: Shown as a function of detuning from ^{85}Rb $F = 2$ to $F' = 3$ obtained using a cell heated to 124°C with $\sim$ 270 G applied magnetic field. A room temperature Doppler broadened transmission spectrum is shown for reference.

an amplitude of 20 mA) synchronously with the piezo. As a result of this modification the scan range of the laser is increased from 2.5 GHz to around 14 GHz. The laser output is split into two beams using a glass blank. The weak reflection from the glass blank is used to record a transmission spectrum using a room temperature vapour cell for reference. The transmitted beam is sent through a half-waveplate and polarizing beam splitter (PBS) cube to pick off light for the Raman sideband cooling, leaving a small proportion of the total output light for the Faraday beam. This light is sent through a second PBS to ensure well defined polarization (extinction of 500:1) and is attenuated to $\sim$ 170 μW. Inside the cell the beam has a $1/e^2$ radius of 1.30(2) mm. The Faraday cell is a modification of the DAVLL cell used in [224] consisting of two 43 mm long solenoids, each wound with 8 layers (53 turns per layer) of 0.8 mm polyurethane coated copper wire (rated at 150 °C) surrounding a 7.5 cm long rubidium vapour cell. When supplied with 6 A the solenoids produce a magnetic field of $\sim$ 270 G (the field varies smoothly between 240 G and 300 G along the length of the cell) and simultaneously heat the rubidium vapour cell enclosed to 110 °C once thermal equilibrium

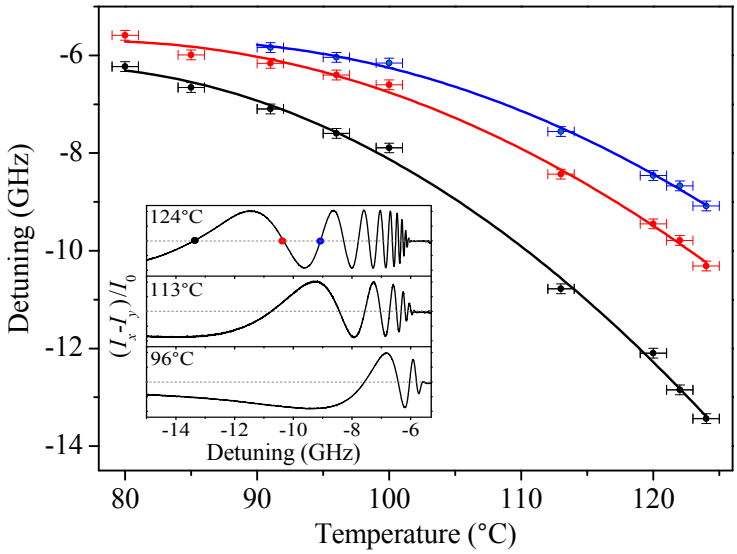

Figure A.3: Effect of temperature on detuning: Detuning from ^{85}Rb $F = 2$ to $F' = 3$ of the last (black, bottom), second to last (red, center) and third to last (blue, top) zero crossings of the Faraday signal as a function of cell temperature for an applied magnetic field of ~ 270 G. At lower temperatures there is no visible third to last crossing. The fitted lines are a guide to the eye only. Inset: Example signals obtained with a magnetic field of ~ 270 G for three cell temperatures.

is reached. The output from the Faraday cell is analysed by polarimetry. The light is split using a PBS and a half-waveplate set such that, in the absence of any optical rotation, an equal amount of light is incident on each of two photodiodes. (We note all polarization optics are positioned away from the cell to avoid thermal effects.) To produce the Faraday signal the difference in the two photocurrents (I_x - I_y) is converted to a voltage via a transimpedance amplifier ($R = 1.2$ MΩ). Fig. A.2 shows a typical signal normalized to the transmission in the absence of the applied magnetic field (obtained by switching off the cell current), $I_0 = I_{x_0} + I_{y_0}$. Each zero crossing in the observed signal corresponds to a π phase shift between the left and right circular components of the input light and is a potential locking point. A room temperature Doppler broadened transmission spectrum is shown to highlight that several lock points exist both red and blue detuned from resonance. Close to resonance there is no Faraday signal as the atomic vapour is optically thick.

A.4 Effect of temperature

The number and detuning of potential locking points exhibited by the Faraday signal are determined by the combination of the coil temperature and magnetic field. This, in principle, allows the detuning of the lock point to be controlled. To investigate the effect of temperature on the detuning of the lock points the cell was heated by adjusting the current supplied to the copper windings. The temperature was monitored using a K PTFE thermocouple probe inside the metal coil mounting around the cell. Before each measurement the current was set back to 6 A to generate the same magnetic field within the cell without allowing the temperature to change. As the temperature of the cell, and therefore the atomic vapour pressure, is increased, the refractive index of the medium increases leading to a greater circular birefringence and an enhanced magneto-optical effect at larger detunings. The detunings of the last, second to and third to last zero crossings with temperature are shown in Fig. A.3. This temperature dependence gives a good coarse adjustment of the lock point between $\sim$ 6 and 14 GHz. Below $\sim$ 70 °C the rotation does not extend beyond the optically thick region and as such there are no suitable lock points.

A.5 Lock stability

To lock to a zero crossing in the Faraday signal we use a homebuilt locking servo. The input to this is the non-normalized output of the differencing photodiode (see inset Fig. A.4). In order to investigate the stability of the Faraday lock a second copy of the setup shown in Fig. A.1 was constructed. Both lasers were locked using their respective Faraday signals and light taken from the two setups was combined and detected on a fast photodiode (2 GHz bandwidth). The frequency of the beat note between the lasers was recorded at 1 s intervals for $\sim$ 80 minutes and the Allan variance [225] calculated. Fig. A.4 shows the square root of the Allan variance as a function of averaging time of the beat frequency between the two Faraday locked lasers. For comparison we also show the results for the case of one laser free running and the second locked with modulation transfer spectroscopy [80] to the ^{85}Rb

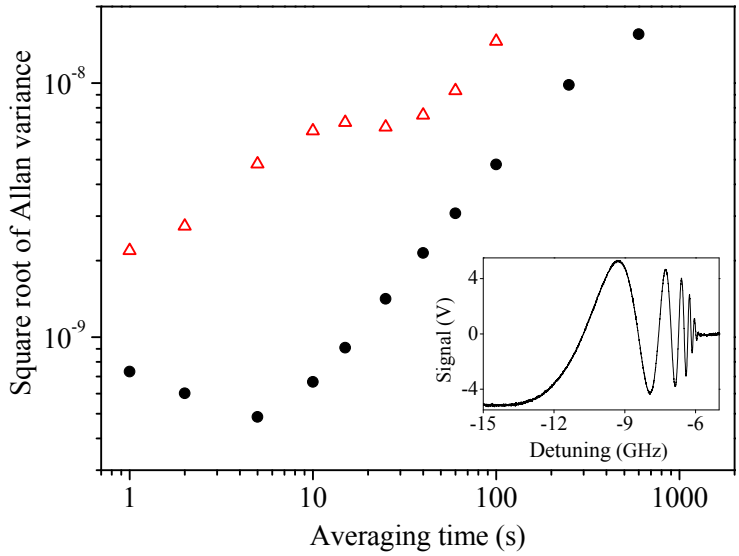

Figure A.4: Allan variance: Square root of the Allan variance of the beat frequency between two Faraday locked (circles) ECDLs. For comparison data for one free running laser and one locked with modulation transfer spectroscopy is also shown (triangles). Inset: Example raw photodiode signal obtained at 113°C.

$F = 3$ to $F' = 4$ transition, stable to $\sim$ 0.1 MHz. For the Faraday locked lasers the fractional frequency stability was 4.9 x 10^{-10} for a 5 s averaging time and over the full monitor period the rms frequency deviation from the mean was $\sim$ 7 MHz. For applications such as DRSC, where the resulting optical potential scales as 1/detuning, this frequency stability ($\approx$ 0.1% of the total detuning) is more than adequate.

To understand the observed fluctuations the sensitivity of the signal to temperature and magnetic field was examined. From Fig. A.3, at 110 °C, the temperature dependence of the last zero crossing is $\sim$ -0.2 GHz/°C. The effect of magnetic field gives a shift of - 0.49(2) MHz/mA, which, assuming a field of 270 G translates into a field sensitivity of - 10.9(4) MHz/G. Considering these sensitivities we attribute the observed fluctuations to small changes in the cell temperature caused by the current supply. We note that the supply to the coil was operated in constant current mode but the current was not actively stabilized. In addition, there was no active stabilization of the ambient temperature and magnetic field. However, with stabilization of temperature ($\sim$ 1 mK) and current ($\sim$ 10 μA), frequency stability on the

order of 200 kHz should be possible.

A.6 Summary

In summary, we have demonstrated a simple laser locking technique which allows off resonance ($\sim$ 6-14 GHz red and blue detuned) stabilization to an absolute frequency using the Faraday effect. A compact heated cell is used, not only to achieve increased rubidium vapour pressure but also to produce a magnetic field parallel to the direction of light propagation. Implementation of the Faraday locking technique extends the useful locking range of an atomic reference considerably. The usual accessible sub Doppler transition range of a few hundred MHz is increased to, in our case, around 25 GHz. We propose the technique for use in the generation of off resonant optical lattices, such as those needed in DRSC schemes. Potentially the detuning achieved could be extended by careful cell design. From extrapolation of Fig. A.3, we expect detunings of 25 GHz and 50 GHz would require 155 °C and 200 °C operating temperatures respectively. Cell designs capable of achieving such temperatures are currently under construction.

Bibliography

[1] J. S. Russell, *Report on waves*, in *Report of the fourteenth meeting of the British association for the advancement of Science*, pp. 311–90, John Murray, 1845.

[2] T. Dauxois and M. Peyrard, *Physics of solitons* (Cambridge University Press, Cambridge, UK, 2006).

[3] S. Cornish *et al.*, *Quantum reflection of bright matter-wave solitons*, Physica D: Nonlinear Phenomena **238**, 1299 (2009).

[4] A. D. Cronin, J. Schmiedmayer, and D. E. Pritchard, *Optics and interferometry with atoms and molecules*, Rev. Mod. Phys. **81**, 1051 (2009).

[5] K. E. Strecker, G. B. Partridge, A. G. Truscott, and R. G. Hulet, *Formation and propagation of matter-wave soliton trains*, Nature **417**, 150 (2002).

[6] L. Khaykovich *et al.*, *Formation of a matter-wave bright soliton*, Science **296**, 1290 (2002).

[7] S. L. Cornish, S. T. Thompson, and C. E. Wieman, *Formation of bright matter-wave solitons during the collapse of attractive Bose–Einstein condensates*, Phys. Rev. Lett. **96**, 170401 (2006).

[8] N. Parker, A. Martin, C. Adams, and S. Cornish, *Bright solitary waves of trapped atomic Bose–Einstein condensates*, Physica D: Nonlinear Phenomena **238**, 1456 (2009).

[9] L. D. Carr and J. Brand, *Spontaneous soliton formation and modulational instability in Bose–Einstein condensates*, Phys. Rev. Lett. **92**, 040401 (2004).

[10] B. J. Dabrowska-Wüster, S. Wüster, and M. J. Davis, *Dynamical formation and interaction of bright solitary waves and solitons in the collapse of Bose–Einstein condensates with attractive interactions*, New J. Phys. **11**, 053017 (2009).

[11] P. G. Drazin, *Solitons* (Cambridge University Press, 1983).

[12] J. P. Gordon, *Interaction forces among solitons in optical fibers*, Opt. Lett. **8**, 596 (1983).

[13] P. A. Ruprecht, M. J. Holland, K. Burnett, and M. Edwards, *Time-dependent solution of the nonlinear Schrödinger equation for Bose-condensed trapped neutral atoms*, Phys. Rev. A **51**, 4704 (1995).

[14] C. Chin, R. Grimm, P. Julienne, and E. Tiesinga, *Feshbach resonances in ultracold gases*, Rev. Mod. Phys. **82**, 1225 (2010).

[15] D. Krökel, N. J. Halas, G. Giuliani, and D. Grischkowsky, *Dark-pulse propagation in optical fibers*, Phys. Rev. Lett. **60**, 29 (1988).

[16] B. Denardo *et al.*, *Observations of localized structures in nonlinear lattices: Domain walls and kinks*, Phys. Rev. Lett. **68**, 1730 (1992).

[17] M. Chen, M. A. Tsankov, J. M. Nash, and C. E. Patton, *Microwave magnetic-envelope dark solitons in yttrium iron garnet thin films*, Phys. Rev. Lett. **70**, 1707 (1993).

[18] D. J. Frantzeskakis, *Dark solitons in atomic Bose–Einstein condensates: from theory to experiments*, Journal of Physics A: Mathematical and Theoretical **43**, 213001 (2010).

[19] S. Burger *et al.*, *Dark solitons in Bose–Einstein condensates*, Phys. Rev. Lett. **83**, 5198 (1999).

[20] J. Denschlag *et al.*, *Generating solitons by phase engineering of a Bose–Einstein condensate*, Science **287**, 97 (2000).

[21] Z. Dutton, M. Budde, C. Slowe, and L. V. Hau, *Observation of quantum shock waves created with ultra- compressed slow light pulses in a Bose–Einstein condensate*, Science **293**, 663 (2001).

[22] N. S. Ginsberg, J. Brand, and L. V. Hau, *Observation of hybrid soliton vortex-ring structures in Bose–Einstein condensates*, Phys. Rev. Lett. **94**, 040403 (2005).

[23] S. Burger, L. D. Carr, P. Öhberg, K. Sengstock, and A. Sanpera, *Generation and interaction of solitons in Bose–Einstein condensates*, Phys. Rev. A **65**, 043611 (2002).

[24] L. D. Carr, J. Brand, S. Burger, and A. Sanpera, *Dark-soliton creation in Bose–Einstein condensates*, Phys. Rev. A **63**, 051601 (2001).

[25] M. R. Andrews *et al.*, *Observation of interference between two Bose condensates*, Science **275**, 637 (1997).

[26] A. Weller *et al.*, *Experimental observation of oscillating and interacting matter wave dark solitons*, Phys. Rev. Lett. **101**, 130401 (2008).

[27] P. Engels and C. Atherton, *Stationary and nonstationary fluid flow of a Bose–Einstein condensate through a penetrable barrier*, Phys. Rev. Lett. **99**, 160405 (2007).

[28] O. Zobay, S. Pötting, P. Meystre, and E. M. Wright, *Creation of gap solitons in Bose–Einstein condensates*, Phys. Rev. A **59**, 643 (1999).

[29] B. Eiermann *et al.*, *Bright Bose–Einstein gap solitons of atoms with repulsive interaction*, Phys. Rev. Lett. **92**, 230401 (2004).

[30] S. L. Cornish, N. R. Claussen, J. L. Roberts, E. A. Cornell, and C. E. Wieman, *Stable ^{85}Rb Bose–Einstein condensates with widely tunable interactions*, Phys. Rev. Lett. **85**, 1795 (2000).

[31] P. A. Altin *et al.*, *^{85}Rb tunable-interaction Bose-Einstein condensate machine*, Rev. Sci. Instrum. **81**, 063103 (2010).

[32] D. E. Pritchard, *Cooling neutral atoms in a magnetic trap for precision spectroscopy*, Phys. Rev. Lett. **51**, 1336 (1983).

[33] S. B. Papp, J. M. Pino, and C. E. Wieman, *Tunable miscibility in a dual-species Bose–Einstein condensate*, Phys. Rev. Lett. **101**, 040402 (2008).

[34] E. A. Donley *et al.*, *Dynamics of collapsing and exploding Bose–Einstein condensates*, Nature **412**, 295 (2001).

[35] J. L. Roberts *et al.*, *Controlled collapse of a Bose–Einstein condensate*, Phys. Rev. Lett. **86**, 4211 (2001).

[36] E. A. Donley, N. R. Claussen, S. T. Thompson, and C. E. Wieman, *Atom-molecule coherence in a Bose–Einstein condensate*, Nature **417**, 529 (2002).

[37] N. R. Claussen *et al.*, *Very-high-precision bound-state spectroscopy near a ^{85}Rb Feshbach resonance*, Phys. Rev. A **67**, 060701 (2003).

[38] P. A. Altin *et al.*, *Collapse and three-body loss in a ^{85}Rb Bose–Einstein condensate*, Phys. Rev. A **84**, 033632 (2011).

[39] P. A. Altin *et al.*, *Measurement of inelastic losses in a sample of ultracold ^{85}Rb*, Phys. Rev. A **81**, 012713 (2010).

[40] L. Khaykovich *et al.*, *Formation of a matter-wave bright soliton*, Science **296**, 1290 (2002).

[41] N. G. Parker, A. M. Martin, S. L. Cornish, and C. S. Adams, *Collisions of bright solitary matter waves*, J. Phys. B **41**, 045303 (2008).

[42] A. I. Streltsov, O. E. Alon, and L. S. Cederbaum, *Formation and dynamics of many-Boson fragmented states in one-dimensional attractive ultracold gases*, Phys. Rev. Lett. **100**, 130401 (2008).

[43] S. Händel, *Experiments on ultracold quantum gases of ^{85}Rb and ^{87}Rb*, PhD thesis, Durham University, 2011.

[44] S. Händel, A. L. Marchant, T. P. Wiles, S. A. Hopkins, and S. L. Cornish, *Magnetic transport apparatus for the production of ultracold atomic gases in the vicinity of a dielectric surface*, Rev. Sci. Instrum. **83**, 013105 (2012).

[45] A. L. Marchant, S. Händel, T. P. Wiles, S. A. Hopkins, and S. L. Cornish, *Guided transport of ultracold gases of rubidium up to a room-temperature dielectric surface*, New J. Phys. **13**, 125003 (2011).

[46] A. L. Marchant, S. Händel, S. A. Hopkins, T. P. Wiles, and S. L. Cornish, *Bose–Einstein condensation of ^{85}Rb by direct evaporation in an optical dipole trap*, Phys. Rev. A **85**, 053647 (2012).

[47] A. L. Marchant *et al.*, *Controlled formation and reflection of a bright solitary matter-wave*, Nat. Commun. **4**, 1865 (2013).

[48] A. L. Marchant *et al.*, *Off-resonance laser frequency stabilization using the Faraday effect*, Opt. Lett. **36**, 64 (2011).

[49] S. Händel *et al.*, *Magnetic merging of ultracold atomic gases of ^{85}Rb and ^{87}Rb*, Phys. Rev. A **83**, 053633 (2011).

[50] T. P. Billam, A. L. Marchant, S. L. Cornish, S. A. Gardiner, and N. Parker, *Bright solitary matter waves: formation, stability and interactions*, in *Spontaneous symmetry breaking, self-trapping, and Josephson oscillations*, edited by B. A. Malomed, Progress in optical science and photonics, Springer, 2013.

[51] V. Bagnato, D. E. Pritchard, and D. Kleppner, *Bose–Einstein condensation in an external potential*, Phys. Rev. A **35**, 4354 (1987).

[52] S. N. Bose, *Plancks law and light quantum hypothesis*, Z. Phys. **26**, 178 (1924).

[53] A. Einstein, *Quantentheorie des einatomigen idealen gases*, Sitzber. Kgl. Preuss. Akad. Wiss. , 261 (1924).

[54] M. H. Anderson, J. R. Ensher, M. R. Matthews, C. E. Wieman, and E. A. Cornell, *Observation of Bose–Einstein condensation in a dilute atomic vapor*, Science **269**, 198 (1995).

[55] K. B. Davis *et al.*, *Bose–Einstein condensation in a gas of sodium atoms*, Phys. Rev. Lett. **75**, 3969 (1995).

[56] C. C. Bradley, C. A. Sackett, J. J. Tollett, and R. G. Hulet, *Evidence of Bose–Einstein condensation in an atomic gas with attractive interactions*, Phys. Rev. Lett. **75**, 1687 (1995).

[57] P. D. Lett *et al.*, *Observation of atoms laser cooled below the Doppler limit*, Phys. Rev. Lett. **61**, 169 (1988).

[58] H. F. Hess, *Evaporative cooling of magnetically trapped and compressed spin-polarized hydrogen*, Phys. Rev. B **34**, 3476 (1986).

[59] N. Masuhara *et al.*, *Evaporative cooling of spin-polarized atomic hydrogen*, Phys. Rev. Lett. **61**, 935 (1988).

[60] C. J. Pethick and H. Smith, *Bose–Einstein condensation in dilute gases* (Cambridge University Press, 2001).

[61] C. J. Foot, *Atomic physics* (Oxford University Press, 2005).

[62] F. Dalfovo, S. Giorgini, L. P. Pitaevskii, and S. Stringari, *Theory of Bose–Einstein condensation in trapped gases*, Rev. Mod. Phys. **71**, 463 (1999).

[63] N. G. Parker, S. L. Cornish, C. S. Adams, and A. M. Martin, *Bright solitary waves and trapped solutions in Bose–Einstein condensates with attractive interactions*, J. Phys. B: At. Mol. Opt. **40**, 3127 (2007).

[64] L. Pitaevskii and S. Stringari, *Bose–Einstein condensation* (Clarendon Press Oxford, 2003).

[65] V. M. Pérez-Garcia, H. Michinel, and H. Herrero, *Bose–Einstein solitons in highly asymmetric traps*, Phys. Rev. A **57**, 3837 (1998).

[66] A. Gammal, T. Frederico, and L. Tomio, *Critical number of atoms for attractive Bose–Einstein condensates with cylindrically symmetrical traps*, Phys. Rev. A **64**, 055602 (2001).

[67] A. Gammal, L. Tomio, and T. Frederico, *Critical numbers of attractive Bose–Einstein condensed atoms in asymmetric traps*, Phys. Rev. A **66**, 043619 (2002).

[68] T. P. Billam, S. A. Wrathmall, and S. A. Gardiner, *Variational determination of approximate bright matter-wave soliton solutions in anisotropic traps*, Phys. Rev. A **85**, 013627 (2012).

[69] V. M. Pérez-Garcia, H. Michinel, J. I. Cirac, M. Lewenstein, and P. Zoller, *Dynamics of Bose–Einstein condensates: Variational solutions of the Gross–Pitaevskii equations*, Phys. Rev. A **56**, 1424 (1997).

[70] P. G. Kevrekidis, D. J. Frantzeskakis, and R. Carretero-González, editors, *Emergent nonlinear phenomena in Bose–Einstein condensates* (Springer, 2008).

[71] A. D. Martin, C. S. Adams, and S. A. Gardiner, *Bright solitary-matter-wave collisions in a harmonic trap: Regimes of solitonlike behavior*, Phys. Rev. A **77**, 013620 (2008).

[72] A. D. Martin, C. S. Adams, and S. A. Gardiner, *Bright matter-wave soliton collisions in a harmonic trap: Regular and chaotic dynamics*, Phys. Rev. Lett. **98**, 020402 (2007).

[73] K. Tai, A. Hasegawa, and A. Tomita, *Observation of modulational instability in optical fibers*, Phys. Rev. Lett. **56**, 135 (1986).

[74] U. Al Khawaja, H. T. C. Stoof, R. G. Hulet, K. E. Strecker, and G. B. Partridge, *Bright soliton trains of trapped Bose–Einstein condensates*, Phys. Rev. Lett. **89**, 200404 (2002).

[75] L. D. Carr, J. N. Kutz, and W. P. Reinhardt, *Stability of stationary states in the cubic nonlinear Schrödinger equation: Applications to the Bose–Einstein condensate*, Phys. Rev. E **63**, 066604 (2001).

[76] L. Khaykovich and B. A. Malomed, *Deviation from one dimensionality in stationary properties and collisional dynamics of matter-wave solitons*, Phys. Rev. A **74**, 023607 (2006).

[77] T. Mayteevarunyoo, B. A. Malomed, and M. Krairiksh, *Stability limits for two-dimensional matter-wave solitons in a time-modulated quasi-one-dimensional optical lattice*, Phys. Rev. A **76**, 053612 (2007).

[78] T. P. Billam, S. L. Cornish, and S. A. Gardiner, *Realizing bright-matter-wave-soliton collisions with controlled relative phase*, Phys. Rev. A **83**, 041602 (2011).

[79] C. Klempt *et al.*, *Ultraviolet light-induced atom desorption for large rubidium and potassium magneto-optical traps*, Phys. Rev. A **73**, 013410 (2006).

[80] D. J. McCarron, S. A. King, and S. L. Cornish, *Modulation transfer spectroscopy in atomic rubidium*, Meas. Sci. Technol. **19** (2008).

[81] G. C. Bjorklund, *Frequency-modulation spectroscopy: A new method for measuring weak absorptions and dispersions*, Opt. Lett. **5** (1980).

[82] H. J. Metcalf and P. van der Straten, *Laser cooling and trapping* (Springer, 1999).

[83] M. Greiner, I. Bloch, T. W. Hänsch, and T. Esslinger, *Magnetic transport of trapped cold atoms over a large distance*, Phys. Rev. A **63**, 031401 (2001).

[84] H. J. Lewandowski, D. M. Harber, D. L. Whitaker, and E. A. Cornell, *Simplified system for creating a Bose-Einstein condensate*, J. Low Temp. Phys. **132**, 309 (2003).

[85] W. Ketterle and N. Van Druten, *Evaporative cooling of trapped atoms*, Advances in atomic, molecular and optical physics **37** (1996).

[86] J.-F. Clément *et al.*, *All-optical runaway evaporation to Bose–Einstein condensation*, Phys. Rev. A **79**, 061406 (2009).

[87] C.-L. Hung, X. Zhang, N. Gemelke, and C. Chin, *Accelerating evaporative cooling of atoms into Bose–Einstein condensation in optical traps*, Phys. Rev. A **78**, 011604 (2008).

[88] M. L. Harris, *Realisation of a cold mixture of rubidium and caesium*, PhD thesis, Durham University, 2008.

[89] J. F. Bertelsen, *Ultracold atomic gases mixtures and molecules*, PhD thesis, University of Aarhus, 2007.

[90] E. Majorana, *Oriented atoms in a variable magnetic field*, Nuovo Cimento **9**, 43 (1932).

[91] Y.-J. Lin, A. R. Perry, R. L. Compton, I. B. Spielman, and J. V. Porto, *Rapid production of ^{87}Rb Bose–Einstein condensates in a combined magnetic and optical potential*, Phys. Rev. A **79**, 063631 (2009).

[92] R. Grimm, M. Weidemller, and Y. B. Ovchinnikov, *Optical dipole traps for neutral atoms*, Adv. At. Mol. Opt. Phys. **42**, 95 (2000).

[93] M. S. Safronova, B. Arora, and C. W. Clark, *Frequency-dependent polarizabilities of alkali-metal atoms from ultraviolet through infrared spectral regions*, Phys. Rev. A **73**, 022505 (2006).

[94] National Instruments, *National Instruments FPGA Fundamentals*, Online, http://www.ni.com/white-paper/6983/en.

[95] A. M. Thomas, *Ultra-cold collisions and evaporative cooling of caesium in a magnetic trap*, PhD thesis, Oxford University, 2004.

[96] C. G. Townsend *et al.*, *Phase-space density in the magneto-optical trap*, Phys. Rev. A **52**, 1423 (1995).

[97] G. Breit and I. I. Rabi, *Measurement of nuclear spin*, Phys. Rev. **38**, 2082 (1931).

[98] I. Newton, *PhilosophiæNaturalis Principia Mathematica* (The Royal Society, London, 1687).

[99] M. Kramer *et al.*, *Strong-field tests of gravity using pulsars and black holes*, New Astron. Rev. **48**, 993 (2004).

[100] C. D. Hoyle *et al.*, *Submillimeter test of the gravitational inverse-square law: A search for "large" extra dimensions*, Phys. Rev. Lett. **86**, 1418 (2001).

[101] M. Masuda and M. Sasaki, *Limits on nonstandard forces in the sub-micrometer range*, Phys. Rev. Lett. **102**, 171101 (2009).

[102] H. Cavendish, *Experiments to determine the density of the Earth*, Roy. Soc. Phil. Trans. **88**, 469 (1798).

[103] M. V. Moody and H. J. Paik, *Gauss's law test of gravity at short range*, Phys. Rev. Lett. **70**, 1195 (1993).

[104] J. Chiaverini, S. J. Smullin, A. A. Geraci, D. M. Weld, and A. Kapitulnik, *New experimental constraints on non-Newtonian forces below* 100 μm, Phys. Rev. Lett. **90**, 151101 (2003).

[105] J. C. Long *et al.*, *Upper limits to submillimetre-range forces from extra space-time dimensions*, Nature **421**, 922 (2003).

[106] D. J. Kapner *et al.*, *Tests of the gravitational inverse-square law below the dark-energy length scale*, Phys. Rev. Lett. **98**, 021101 (2007).

[107] H. Casimir, *On the attraction between two perfectly conducting plates*, Proc. K. Ned. Akad. Wet **51** (1948).

[108] A. Lambrecht, P. A. M. Neto, and S. Reynaud, *The Casimir effect within scattering theory*, New J. Phys. **8**, 243 (2006).

[109] H. B. G. Casimir and D. Polder, *The influence of retardation on the London-van der Waals forces*, Phys. Rev. **73**, 360 (1948).

[110] A. McLachlan, *Van der Waals forces between an atom and a surface*, Mol. Phys. **7**, 381 (1963-1964).

[111] H. B. G. Casimir and D. Polder, *Influence of retardation on the London van der Waals forces*, Nature **158**, 787 (1946).

[112] M. Antezza, L. P. Pitaevskii, and S. Stringari, *Effect of the Casimir–Polder force on the collective oscillations of a trapped Bose–Einstein condensate*, Phys. Rev. A **70**, 053619 (2004).

[113] S. Dimopoulos and A. A. Geraci, *Probing submicron forces by interferometry of Bose–Einstein condensed atoms*, Phys. Rev. D **68**, 124021 (2003).

[114] P. Wolf *et al.*, *From optical lattice clocks to the measurement of forces in the Casimir regime*, Phys. Rev. A **75**, 063608 (2007).

[115] V. Sandoghdar, C. I. Sukenik, E. A. Hinds, and S. Haroche, *Direct measurement of the van der Waals interaction between an atom and its images in a micron-sized cavity*, Phys. Rev. Lett. **68**, 3432 (1992).

[116] R. Onofrio, *Casimir forces and non-Newtonian gravitation*, New J. Phys. **8**, 237 (2006).

[117] A. Landragin *et al.*, *Measurement of the van der Waals force in an atomic mirror*, Phys. Rev. Lett. **77**, 1464 (1996).

[118] C. I. Sukenik, M. G. Boshier, D. Cho, V. Sandoghdar, and E. A. Hinds, *Measurement of the Casimir–Polder force*, Phys. Rev. Lett. **70**, 560 (1993).

[119] H. Bender, P. W. Courteille, C. Marzok, C. Zimmermann, and S. Slama, *Direct measurement of intermediate-range Casimir–Polder potentials*, Phys. Rev. Lett. **104**, 083201 (2010).

[120] D. M. Harber, J. M. Obrecht, J. M. McGuirk, and E. A. Cornell, *Measurement of the Casimir–Polder force through center-of-mass oscillations of a Bose–Einstein condensate*, Phys. Rev. A **72**, 033610 (2005).

[121] R. Jáuregui, *Nonperturbative and perturbative treatments of parametric heating in atom traps*, Phys. Rev. A **64**, 053408 (2001).

[122] D. M. Harber, J. M. McGuirk, J. M. Obrecht, and E. A. Cornell, *Thermally induced losses in ultra-cold atoms magnetically trapped near room-temperature surfaces*, J. Low Temp. Phys. **133**, 229 (2003).

[123] F. Sorrentino *et al.*, *Quantum sensor for atom-surface interactions below* $10\mu m$, Phys. Rev. A **79**, 013409 (2009).

[124] D. Rychtarik, B. Engeser, H.-C. Nägerl, and R. Grimm, *Two-dimensional Bose–Einstein condensate in an optical surface trap*, Phys. Rev. Lett. **92**, 173003 (2004).

[125] T. Schumm *et al.*, *Matter-wave interferometry in a double well on an atom chip*, Nature Phys. **1**, 57 (2005).

[126] J. I. Gillen *et al.*, *Two-dimensional quantum gas in a hybrid surface trap*, Phys. Rev. A **80**, 021602 (2009).

[127] J. M. Obrecht *et al.*, *Measurement of the temperature dependence of the Casimir–Polder force*, Phys. Rev. Lett. **98**, 063201 (2007).

[128] M. A. Kasevich, D. S. Weiss, and S. Chu, *Normal-incidence reflection of slow atoms from an optical evanescent wave*, Opt. Lett. **15**, 607 (1990).

[129] M. Christ, A. Scholz, M. Schiffer, R. Deutschmann, and W. Ertmer, *Diffraction and reflection of a slow metastable neon beam by an evanescent light grating*, Opt. Commun. **107**, 211 (1994).

[130] W. Seifert, R. Kaiser, A. Aspect, and J. Mlynek, *Reflection of atoms from a dielectric wave guide*, Opt. Commun. **111**, 566 (1994).

[131] V. Savalli *et al.*, *Specular reflection of matter waves from a rough mirror*, Phys. Rev. Lett. **88**, 250404 (2002).

[132] H. Perrin, Y. Colombe, B. Mercier, V. Lorent, and C. Henkel, *Diffuse reflection of a Bose–Einstein condensate from a rough evanescent wave mirror*, J. Phys. B: At. Mol. Phys. **39**, 4649 (2006).

[133] H. Bender, P. Courteille, C. Zimmermann, and S. Slama, *Towards surface quantum optics with Bose–Einstein condensates in evanescent waves*, Appl. Phys. B: Lasers and Opt. **96**, 275 (2009).

[134] Y. Colombe *et al.*, *Schemes for loading a Bose–Einstein condensate into a two-dimensional dipole trap*, J. Opt. B: Quant. Semiclass. Opt. **5**, S155 (2003).

[135] S. Schmid, G. Thalhammer, K. Winkler, F. Lang, and J. H. Denschlag, *Long distance transport of ultracold atoms using a 1D optical lattice*, New J. Phys **8**, 159 (2006).

[136] Y. B. Ovchinnikov, S. V. Shul'ga, and V. I. Balykin, *An atomic trap based on evanescent light waves*, J Phys. B: At. Mol. Phys. **24**, 3173 (1991).

[137] P. Desbiolles and J. Dalibard, *Loading atoms in a bi-dimensional light trap*, Opt. Commun. **132**, 540 (1996).

[138] A. H. Barnett *et al.*, *Substrate-based atom waveguide using guided two-color evanescent light fields*, Phys. Rev. A **61**, 023608 (2000).

[139] M. Hammes, D. Rychtarik, B. Engeser, H.-C. Nägerl, and R. Grimm, *Evanescent-wave trapping and evaporative cooling of an atomic gas at the crossover to two dimensions*, Phys. Rev. Lett. **90**, 173001 (2003).

[140] J. Chwedeńczuk, L. Pezzé, F. Piazza, and A. Smerzi, *Rabi interferometry and sensitive measurement of the Casimir–Polder force with ultracold gases*, Phys. Rev. A **82**, 032104 (2010).

[141] N. Poli *et al.*, *Precision measurement of gravity with cold atoms in an optical lattice and comparison with a classical gravimeter*, Phys. Rev. Lett. **106**, 038501 (2011).

[142] D. L. Jenkin, *Feshbach spectroscopy of an ultracold Rb-Cs mixture*, PhD thesis, Durham University, 2012.

[143] O. Morsch and M. Oberthaler, *Dynamics of Bose–Einstein condensates in optical lattices*, Rev. Mod. Phys. **78**, 179 (2006).

[144] S. Friebel, C. D'Andrea, J. Walz, M. Weitz, and T. W. Hänsch, CO_2-*laser optical lattice with cold rubidium atoms*, Phys. Rev. A **57**, R20 (1998).

[145] P. L. Gould, G. A. Ruff, and D. E. Pritchard, *Diffraction of atoms by light: The near-resonant Kapitza-Dirac effect*, Phys. Rev. Lett. **56**, 827 (1986).

[146] E. Tiesinga, B. J. Verhaar, and H. T. C. Stoof, *Threshold and resonance phenomena in ultracold ground-state collisions*, Phys. Rev. A **47**, 4114 (1993).

[147] S. Giorgini, L. P. Pitaevskii, and S. Stringari, *Theory of ultracold atomic Fermi gases*, Rev. Mod. Phys. **80**, 1215 (2008).

[148] T. Köhler, K. Góral, and P. S. Julienne, *Production of cold molecules via magnetically tunable Feshbach resonances*, Rev. Mod. Phys. **78**, 1311 (2006).

[149] J. G. Danzl *et al.*, *An ultracold high-density sample of rovibronic ground-state molecules in an optical lattice*, Nat. Phys. **6**, 265 (2010).

[150] K.-K. Ni *et al.*, *A high phase-space-density gas of polar molecules*, Science **322**, 231 (2008).

[151] T. Volz, S. Dürr, S. Ernst, A. Marte, and G. Rempe, *Characterization of elastic scattering near a Feshbach resonance in* ^{87}Rb, Phys. Rev. A **68**, 010702 (2003).

[152] J. L. Roberts *et al.*, *Resonant magnetic field control of elastic scattering in cold* ^{85}*Rb*, Phys. Rev. Lett. **81**, 5109 (1998).

[153] S. B. Papp *et al.*, *Bragg spectroscopy of a strongly interacting* ^{85}*Rb Bose–Einstein condensate*, Phys. Rev. Lett. **101**, 135301 (2008).

[154] J. P. Burke, J. L. Bohn, B. D. Esry, and C. H. Greene, *Prospects for mixed-isotope Bose–Einstein condensates in rubidium*, Phys. Rev. Lett. **80**, 2097 (1998).

[155] J. L. Roberts, N. R. Claussen, S. L. Cornish, and C. E. Wieman, *Magnetic field dependence of ultracold inelastic collisions near a Feshbach resonance*, Phys. Rev. Lett. **85**, 728 (2000).

[156] J. James Patrick Burke, *Theoretical investigation of cold alkali atom collisions*, PhD thesis, JILA, 1999.

[157] C. Ramsauer, *Über den wirkungsquerschnitt der gasmoleküle gegenber langsamen elektronen*, Ann. Physik **64**, 513 (1921).

[158] J. S. Townsend and V. A. Bailey, *The motion of electrons in argon*, Phil. Mag. **43**, 593 (1922).

[159] D. J. Han, R. H. Wynar, P. Courteille, and D. J. Heinzen, *Bose–Einstein condensation of large numbers of atoms in a magnetic time-averaged orbiting potential trap*, Phys. Rev. A **57**, R4114 (1998).

[160] V. V. Flambaum, G. F. Gribakin, and C. Harabati, *Analytical calculation of cold-atom scattering*, Phys. Rev. A **59**, 1998 (1999).

[161] C. Chin, *Cooling, collisions and coherence of cold cesium atoms in a trap*, PhD thesis, Stanford University, 2001.

[162] J. Herbig *et al.*, *Preparation of a pure molecular quantum gas*, Science **301**, 1510 (2003).

[163] C. A. Regal, C. Ticknor, J. L. Bohn, and D. S. Jin, *Creation of ultracold molecules from a Fermi gas of atoms*, Nature **424**, 47 (2003).

[164] M. Greiner, C. A. Regal, and D. S. Jin, *Emergence of a molecular Bose–Einstein condensate from a Fermi gas*, Nature **426**, 537 (2003).

[165] M. Bartenstein *et al.*, *Collective excitations of a degenerate gas at the BEC-BCS crossover*, Phys. Rev. Lett. **92**, 203201 (2004).

[166] T. Bourdel *et al.*, *Experimental study of the BEC-BCS crossover region in lithium 6*, Phys. Rev. Lett. **93**, 050401 (2004).

[167] L. Pitaevskii and S. Stringari, *Elementary excitations in trapped Bose–Einstein condensed gases beyond the mean-field approximation*, Phys. Rev. Lett. **81**, 4541 (1998).

[168] M. Gustavsson *et al.*, *Control of interaction-induced dephasing of Bloch oscillations*, Phys. Rev. Lett. **100**, 080404 (2008).

[169] C. C. Tsai *et al.*, *Two-color photoassociation spectroscopy of ground state* Rb_2, Phys. Rev. Lett. **79**, 1245 (1997).

[170] J. M. Vogels *et al.*, *Prediction of Feshbach resonances in collisions of ultracold rubidium atoms*, Phys. Rev. A **56**, R1067 (1997).

[171] P. Courteille, R. S. Freeland, D. J. Heinzen, F. A. van Abeelen, and B. J. Verhaar, *Observation of a Feshbach resonance in cold atom scattering*, Phys. Rev. Lett. **81**, 69 (1998).

[172] J. L. Roberts *et al.*, *Improved characterization of elastic scattering near a Feshbach resonance in* ^{85}Rb, Phys. Rev. A **64**, 024702 (2001).

[173] C. L. Blackley, Private communication.

[174] N. R. Claussen, *Dynamics of Bose–Einstein condensates near a Feshbach resonance in* ^{85}*Rb*, PhD thesis, JILA, 1996.

[175] T. Kraemer *et al.*, *Optimized production of a cesium Bose–Einstein condensate*, Applied Physics B **79**, 1013 (2004).

[176] E. A. Burt *et al.*, *Coherence, correlations, and collisions: What one learns about Bose–Einstein condensates from their decay*, Phys. Rev. Lett. **79**, 337 (1997).

[177] Y. Kagan, B. Svistunov, and G. Shlyapnikov, *Effect of Bose condensation on inelastic processes in gases*, JETP Lett. **42**, 169 (1985).

[178] T. Weber, J. Herbig, M. Mark, H.-C. Nägerl, and R. Grimm, *Three-body recombination at large scattering lengths in an ultracold atomic gas*, Phys. Rev. Lett. **91**, 123201 (2003).

[179] P. O. Fedichev, M. W. Reynolds, and G. V. Shlyapnikov, *Three-body recombination of ultracold atoms to a weakly bound s level*, Phys. Rev. Lett. **77**, 2921 (1996).

[180] E. Nielsen and J. H. Macek, *Low-energy recombination of identical bosons by three-body collisions*, Phys. Rev. Lett. **83**, 1566 (1999).

[181] B. D. Esry, C. H. Greene, and J. P. Burke, *Recombination of three atoms in the ultracold limit*, Phys. Rev. Lett. **83**, 1751 (1999).

[182] P. F. Bedaque, E. Braaten, and H.-W. Hammer, *Three-body recombination in Bose gases with large scattering length*, Phys. Rev. Lett. **85**, 908 (2000).

[183] T. Weber, J. Herbig, M. Mark, H.-C. Nägerl, and R. Grimm, *Three-body recombination at large scattering lengths in an ultracold atomic gas*, Phys. Rev. Lett. **91**, 123201 (2003).

[184] J. P. Burke, J. L. Bohn, B. D. Esry, and C. H. Greene, *Impact of the* ^{87}*Rb singlet scattering length on suppressing inelastic collisions*, Phys. Rev. A **55**, R2511 (1997).

[185] P. Julienne, Private communication.

[186] L. Salasnich, A. Parola, and L. Reatto, *Condensate bright solitons under transverse confinement*, Phys. Rev. A **66**, 043603 (2002).

[187] V. I. Yukalov and E. P. Yukalova, *Optimal trap shape for a Bose gas with attractive interactions*, Phys. Rev. A **72**, 063611 (2005).

[188] C. C. Bradley, C. A. Sackett, and R. G. Hulet, *Bose–Einstein condensation of lithium: Observation of limited condensate number*, Phys. Rev. Lett. **78**, 985 (1997).

[189] J. M. Gerton, D. Strekalov, I. Prodan, and R. G. Hulet, *Direct observation of growth and collapse of a Bose–Einstein condensate with attractive interactions*, Nature **408**, 692 (2000).

[190] O. E. Alon, A. I. Streltsov, and L. S. Cederbaum, *Multiconfigurational time-dependent Hartree method for bosons: Many-body dynamics of bosonic systems*, Phys. Rev. A **77**, 033613 (2008).

[191] A. I. Streltsov, O. E. Alon, and L. S. Cederbaum, *Swift loss of coherence of soliton trains in attractive Bose–Einstein condensates*, Phys. Rev. Lett. **106**, 240401 (2011).

[192] T. P. Billam, Private communication.

[193] J. L. Helm, T. P. Billam, and S. A. Gardiner, *Bright matter-wave soliton collisions at narrow barriers*, Phys. Rev. A **85**, 053621 (2012).

[194] A. D. Martin and J. Ruostekoski, *Quantum dynamics of atomic bright solitons under splitting and recollision, and implications for interferometry*, New J. Phys. **14**, 043040 (2012).

[195] P. Dyke, L. Sidong, S. Pollack, D. Dries, and R. Hulet, *Interactions of bright matter-wave solitons with a barrier potential*, in *42nd Annual meeting of the APS division of Atomic, Molecular and Optical Physics*, volume 56, No. 5, 2011.

[196] B. Gertjerenken, T. P. Billam, L. Khaykovich, and C. Weiss, *Scattering bright solitons: Quantum versus mean-field behavior*, Phys. Rev. A **86**, 033608 (2012).

[197] E. H. Lieb and W. Liniger, *Exact analysis of an interacting Bose gas. I. The general solution and the ground state*, Phys. Rev. **130**, 1605 (1963).

[198] C. Weiss and Y. Castin, *Creation and detection of a mesoscopic gas in a nonlocal quantum superposition*, Phys. Rev. Lett. **102**, 010403 (2009).

[199] A. I. Streltsov, O. E. Alon, and L. S. Cederbaum, *Scattering of an attractive Bose–Einstein condensate from a barrier: Formation of quantum superposition states*, Phys. Rev. A **80**, 043616 (2009).

[200] T. Ernst and J. Brand, *Resonant trapping in the transport of a matter-wave soliton through a quantum well*, Phys. Rev. A **81**, 033614 (2010).

[201] H. Michinel, A. Paredes, M. M. Valado, and D. Feijoo, *Coherent emission of atomic soliton pairs by Feshbach-resonance tuning*, Phys. Rev. A **86**, 013620 (2012).

[202] V. I. Balykin, V. S. Letokhov, Y. B. Ovchinnikov, and A. I. Sidorov, *Quantum-state-selective mirror reflection of atoms by laser light*, Phys. Rev. Lett. **60**, 2137 (1988).

[203] R. Côté, B. Segev, and M. G. Raizen, *Retardation effects on quantum reflection from an evanescent-wave atomic mirror*, Phys. Rev. A **58**, 3999 (1998).

[204] F. Shimizu, *Specular reflection of very slow metastable neon atoms from a solid surface*, Phys. Rev. Lett. **86**, 987 (2001).

[205] H. Friedrich, G. Jacoby, and C. G. Meister, *Quantum reflection by Casimir–van der Waals potential tails*, Phys. Rev. A **65**, 032902 (2002).

[206] V. U. Nayak, D. O. Edwards, and N. Masuhara, *Scattering of ^{4}He atoms grazing the liquid-^{4}He surface*, Phys. Rev. Lett. **50**, 990 (1983).

[207] I. A. Yu *et al.*, *Evidence for universal quantum reflection of hydrogen from liquid ^{4}He*, Phys. Rev. Lett. **71**, 1589 (1993).

[208] J. J. Berkhout *et al.*, *Quantum reflection: Focusing of hydrogen atoms with a concave mirror*, Phys. Rev. Lett. **63**, 1689 (1989).

[209] T. A. Pasquini *et al.*, *Quantum reflection from a solid surface at normal incidence*, Phys. Rev. Lett. **93**, 223201 (2004).

[210] V. Giovannetti, S. Lloyd, and L. Maccone, *Quantum-enhanced measurements: Beating the standard quantum limit*, Science **306**, 1330 (2004).

[211] A. J. Kerman, V. Vuletić, C. Chin, and S. Chu, *Beyond optical molasses: 3D Raman sideband cooling of atomic cesium to high phase-space density*, Phys. Rev. Lett. **84**, 439 (2000).

[212] M. L. Harris *et al.*, *Polarization spectroscopy in rubidium and cesium*, Phys. Rev. A **73**, 062509 (2006).

[213] K. L. Corwin, Z.-T. Lu, C. F. Hand, R. J. Epstein, and C. E. Wieman, *Frequency-stabilized diode laser with the Zeeman shift in an atomic vapor*, Appl. Opt. **37**, 3295 (1998).

[214] N. P. Robins, B. J. J. Slagmolen, D. A. Shaddock, J. D. Close, and M. B. Gray, *Interferometric, modulation-free laser stabilization*, Opt. Lett. **27**, 1905 (2002).

[215] H. J. Lee, C. S. Adams, M. Kasevich, and S. Chu, *Raman cooling of atoms in an optical dipole trap*, Phys. Rev. Lett. **76**, 2658 (1996).

[216] T. A. Johnson *et al.*, *Rabi oscillations between ground and Rydberg states with dipole-dipole atomic interactions*, Phys. Rev. Lett. **100**, 113003 (2008).

[217] M. K. Oberthaler, R. M. Godun, M. B. d'Arcy, G. S. Summy, and K. Burnett, *Observation of quantum accelerator modes*, Phys. Rev. Lett. **83**, 4447 (1999).

[218] M. G. Bason, A. K. Mohapatra, K. J. Weatherill, and C. S. Adams, *Narrow absorptive resonances in a four-level atomic system*, J. Phys. B: At. Mol. Phys. **42**, 075503 (2009).

[219] U. Schünemann, H. Engler, R. Grimm, M. Weidemüller, and M. Zielonkowski, *Simple scheme for tunable frequency offset locking of two lasers*, Rev. Sci. Instrum. **70**, 242 (1999).

[220] T. Hansch and B. Couillaud, *Laser frequency stabilization by polarization spectroscopy of a reflecting reference cavity*, Opt. Comm. **35**, 441 (1980).

[221] P. Bohlouli-Zanjani, K. Afrousheh, and J. D. D. Martin, *Optical transfer cavity stabilization using current-modulated injection-locked diode lasers*, Rev. Sci. Instrum. **77** (2006).

[222] P. P. Sorokin, J. R. Lankard, V. L. Moruzzi, and A. Lurio, *Frequency locking of organic dye lasers to atomic resonance lines*, Appl. Phys. Lett. **15** (1969).

[223] P. Siddons, N. C. Bell, Y. Cai, C. S. Adams, and I. G. Hughes, *A gigahertz-bandwidth atomic probe based on the slow-light Faraday effect*, Nature Photon. **3**, 225 (2009).

[224] D. J. McCarron, I. G. Hughes, P. Tierney, and S. L. Cornish, *A heated vapor cell unit for dichroic atomic vapor laser lock in atomic rubidium*, Rev. Sci. Instrum. **78**, 093106 (2007).

[225] D. Allan, *Statistics of atomic frequency standards*, Proceedings of the IEEE **54**, 221 (1966).